1-1-2016

Computational Fluid Dynamics Modeling of Laminar, Transitional, and Turbulent Flows with Sensitivity to Streamline Curvature and Rotational Effects

Varun Chitta

Computational fluid dynamics modeling of laminar, transitional, and turbulent flows with sensitivity to streamline curvature and rotational effects

By

Varun Chitta

A Dissertation
Submitted to the Faculty of
Mississippi State University
in Partial Fulfillment of the Requirements
for the Degree of Doctor of Philosophy
in Mechanical Engineering
in the Department of Mechanical Engineering

Mississippi State, Mississippi

May 2016

Computational fluid dynamics modeling of laminar, transitional, and turbulent flows with sensitivity to streamline curvature and rotational effects

By

Varun Chitta

Approved:

_____

D. Keith Walters
(Major Professor/Graduate Coordinator)

_____

Scott M. Thompson
(Committee Member)

_____

Shanti Bhushan
(Committee Member)

_____

Sundar R. Krishnan
(Committee Member)

_____

Jason M. Keith
Dean
Bagley College of Engineering

Name: Varun Chitta

Date of Degree: May 6, 2016

Institution: Mississippi State University

Major Field: Mechanical Engineering

Major Professor: D. Keith Walters

Title of Study: Computational fluid dynamics modeling of laminar, transitional, and turbulent flows with sensitivity to streamline curvature and rotational effects

Pages in Study 163

Candidate for Degree of Doctor of Philosophy

Modeling of complex flows involving the combined effects of flow transition and streamline curvature using two advanced turbulence models, one in the Reynolds-averaged Navier-Stokes (RANS) category and the other in the hybrid RANS-Large eddy simulation (LES) category is considered in this research effort. In the first part of the research, a new scalar eddy-viscosity model (EVM) is proposed, designed to exhibit physically correct responses to flow transition, streamline curvature, and system rotation effects. The four equation model developed herein is a curvature-sensitized version of a commercially available three-equation transition-sensitive model. The physical effects of rotation and curvature (RC) enter the model through the added transport equation, analogous to a transverse turbulent velocity scale. The eddy-viscosity has been redefined such that the proposed model is constrained to reduce to the original transition-sensitive model definition in nonrotating flows or in regions with negligible RC effects. In the second part of the research, the developed four-equation model is combined with a LES technique using a new hybrid modeling framework, dynamic hybrid RANS-LES. The new framework is highly generalized, allowing coupling of any desired LES model with

any given RANS model and addresses several deficiencies inherent in most current hybrid models. In the present research effort, the DHRL model comprises of the proposed four-equation model for RANS component and the MILES scheme for LES component.

Both the models were implemented into a commercial computational fluid dynamics (CFD) solver and tested on a number of engineering and generic flow problems. Results from both the RANS and hybrid models show successful resolution of the combined effects of transition and curvature with reasonable engineering accuracy, and for only a small increase in computational cost. In addition, results from the hybrid model indicate significant levels of turbulent fluctuations in the flowfield, improved accuracy compared to RANS models predictions, and are obtained at a significant reduction of computational cost compared to full LES models. The results suggest that the advanced turbulence modeling techniques presented in this research effort have potential as practical tools for solving low/high Re flows over blunt/curved bodies for the prediction of transition and RC effects.

DEDICATION

This dissertation is dedicated to my parents Padma and C. S. Murthy, and my grandparents Sitamahalakshmi and C. K. Murthy.

ACKNOWLEDGEMENTS

I take this opportunity to sincerely thank all those who supported and encouraged me during the entire course of this research work and finally getting me to where I am today. This certainly would not have been possible without their prayers and best wishes.

A big thanks to my entire family for their unconditional love, support, encouragement, and freedom they have given me during this period. I am also thankful to all my friends at the High Performance Computing Collaboratory (HPCC), including members from my research group Tausif, Tej, Farid, Eric, Manish, and Ben, for all the support, numerous discussions, late night work, and more importantly the fun we had working together. I will surely remember those fun moments moving forward in life. I am grateful to my PhD committee members Dr. Krishnan and Dr. Thompson for allocating their valuable time to me and providing with valuable insights and suggestions for further improvement of this work. Also, a big thanks to Dr. Shanti Bhushan for the fruitful collaboration on some research projects, for sharing his experiences and knowledge, for all the long discussions we had, and for being a member in my committee.

Lastly, and more importantly, I owe my deepest gratitude to my advisor Professor Keith Walters for all the support, encouragement, and guidance given to me during this period, and also sincerely thank him for introducing me to the field of turbulence modeling. It has been a wonderful experience working under his guidance for all these

years and I deeply appreciate all the experience and knowledge he has provided me. Thank you Dr. Walters for being a true mentor!

This research work would not have been possible without the resources provided by the HPCC center at Mississippi State University, and Mechanical Engineering department. A big thanks to all of them. I am also grateful for the financial support provided by the U.S. National Aeronautics and Space Administration (NASA) under Grant no. NNX10AN06A.

TABLE OF CONTENTS

LIST OF TABLES

LIST OF FIGURES

NOMENCLATURE

Symbols

α	angle of attack; RANS-LES transition parameter in hybrid model
α_T	effective diffusivity for turbulence dependent variables
β_{TS}	Tollmien-Schlichting threshold function
δ	99% boundary layer thickness
ε	turbulent dissipation rate
η	weak equilibrium ratio
η_{eff}	near-wall effective polynomial
II_S	second invariant of mean strain rate tensor
III_S	third invariant of mean strain rate tensor
Λ_z	spanwise domain size
λ_{eff}	effective turbulence length scale
μ	dynamic viscosity
μ_T	turbulent or eddy-viscosity
ν	kinematic viscosity
ν_T	turbulent kinematic viscosity
$\nu_{T,l}$	large-scale turbulent viscosity contribution
$\nu_{T,s}$	small-scale turbulent viscosity contribution

Ω	magnitude of mean rotation rate tensor
Ω_{ij}	rotation rate tensor in inertial frame
Ω'_{ij}	rotation rate tensor in a rotating reference frame
ω	specific dissipation rate
ω^{eff}	modified near-wall dissipation rate
ω^*	rotation rate
ω_m	angular velocity
ρ	density
τ_{ij}	subfilter stress
τ_{ij}^{RANS}	modeled Reynolds stress
τ_{ij}^{SGS}	modeled subgrid stress
θ	angle in degrees
C	airfoil chord
C_D, or c_d	coefficient of drag
C_f	skin friction coefficient
c_l	coefficient of lift
C_p	coefficient of pressure
C_μ	turbulent viscosity coefficient
C_μ^{nonrot}	rotation-sensitive eddy-viscosity coefficient for nonrotating systems
C_μ^{rot}	rotation-sensitive eddy-viscosity coefficient for rotating systems
d	wall distance
D_L	anisotropic (near-wall) dissipation term for k_L

D_T	anisotropic (near-wall) dissipation term for k_T
D_v	anisotropic (near-wall) dissipation term for v^2
f_{INT}	intermittency damping function
f_{SS}	shear-sheltering damping function
f_W	inviscid near-wall damping function
F_W	blending function
f_v	viscous damping function
$f_{\tau,l}$	time-scale damping function
f_ω	boundary layer wake term damping function
H	channel height; hill height
I_0	modified Bessel function
J_0	Bessel function
k, k_T	turbulent kinetic energy
k_L	laminar kinetic energy
$k_{T,l}$	effective large-scale turbulent kinetic energy
$k_{T,s}$	effective small-scale turbulent kinetic energy
k_{TOT}	total fluctuation kinetic energy
P_{k_L}	production of laminar kinetic energy
P_{k_T}	production of turbulent kinetic energy
$\overline{p}$	mean pressure
$\hat{P}$	resolved pressure
R_{BP}	bypass transition production term

Re	Reynolds Number
Re_H	Reynolds number based on hill height
Re_Ω	vorticity-based Reynolds number
Re_θ	momentum thickness Reynolds number
R_{NAT}	natural transition production term
Ro	rotation number
S	magnitude of mean strain rate tensor
S_{ij}	strain rate tensor
$\dot{S}_{ij}$	material derivative of mean strain rate tensor
SST	shear stress transport
t	time
Tu_∞	freestream turbulence intensity
u, v, w	velocity components in the x, y, z directions, respectively
u_i	instantaneous velocity
u''	resolved fluctuating velocity components
$\overline{u_i}$	mean velocity vector
$\widehat{u_i}$	resolved velocity vector
$\overline{u_i' u_j'}$	Reynolds stress tensor
u_i'	fluctuating velocity vector
U	reference velocity
U_∞	freestream mean velocity
U_i	velocity vector

U_m	average channel velocity
U^+	normalized velocity in boundary layer
u_τ	mean friction velocity
v^2	transverse turbulent velocity scale
W	effective flow rotation rate magnitude
W_{ij}	flow rotation rate tensor
x, y, z	Cartesian coordinate directions
y	wall normal distance
$y(r)$	shape function of radius r
y^+	nondimensional wall distance

Subscripts

∞	inlet or freestream condition
μ	viscosity
v	viscous
BP	bypass
D, d	drag
eff	effective
f	friction
i, j, k, m, p, l, q	indices
INT	intermittency
L	large-scale; lift
L	laminar

M	mean value over channel cross-section
NAT	natural
P	pressure
s	small-scale
SGS	subgrid stress
SS	shear-sheltering
T	turbulence
TOT	total
TS	Tollmien-Schlichting
W	wall

Superscripts

+	dimensionless wall quantity
nonrot	nonrotating
RANS	Reynolds-averaged Navier-Stokes
rot	rotating
SGS	subgrid stress

Operators

^ (overbar)	undefined filtering operation (i.e., dictated by simulation)
¯ (overbar)	ensemble or time-average
′	fluctuating
″	resolved fluctuating
e_{ijk}	tensor permutation operator
δ_{ij}	Kronecker delta

CHAPTER I

INTRODUCTION

1.1 Research Motivation

From early 1900s, CFD, a largely unexplored subject back then, has evolved significantly in close association with developments in the fields of fluid dynamics, applied mathematics, and computing science. Being a multi-disciplinary endeavor, the extensive and detailed information that can be obtained from a CFD simulation is immeasurable and more importantly inexpensive, although, highly dependent on the numerical techniques used and their computational efficiency. The growing dependence of industries, governmental agencies, and universities in solving practical problems using numerical techniques has placed a huge demand on the CFD community to deliver newer solution techniques which are accurate, robust, and computationally inexpensive. Some of the applications, an ever-widening range in a variety of disciplines and industries include, aerospace, astrophysics, automotive, chemical manufacturing, environmental engineering, marine and naval architecture, medical research, meteorology, petroleum exploration, polymer processing, power generation, social dynamics [1], and weather prediction.

Despite fast growth of computing power and significant increase in the usage of CFD as a predictive tool, turbulent flows and dispersed, multiphase flows are the two principle weaknesses in the applications of CFD [2], and remain an active area of

research. Both turbulent and multiphase flows are governed by the Navier-Stokes equations which have no exact solutions available. Numerical solution of such equations requires a modeling approach that takes into account the accurate representation of minute details of the flow in both space and time. These flows are commonly observed in industrial applications and hence, simulation of which is of great importance. The present research topic pertains to turbulent flows.

Turbulence is a ubiquitous phenomenon, also observed in many of the fluid-flow circumstances which are of substantial interest to both scientific studies and engineering applications. Modeling of turbulent flows is still considered as one of the outstanding problems in applied mechanics. Many turbulence resolving and modeling approaches are available in the literature today, however, the need for advanced models that are accurate, computationally inexpensive, easy to use, and robust is always present.

1.2 Physical Aspects

In the hierarchy of computational methods possible for the prediction of a turbulent flow, direct numerical simulation (DNS), LES, and RANS can be considered as the three principal strategies, based on the accuracy of the solution. Limited by the computational cost, complexity, or accuracy of the simulations, over the years, other intermediate or bridging methods dubbed hybrid RANS-LES, partially-averaged Navier-Stokes (PANS), very large eddy simulation (VLES), and unsteady RANS (URANS) have been developed. These intermediate strategies were developed in order to find a compromise between computational efficiency and accuracy of the numerical methods, such that more powerful tools will be available for use in industrial applications where

DNS or LES remain computationally out of reach. A brief introduction on various turbulence modeling strategies is given below.

1.2.1 DNS

Solutions to the equations of motion (i.e., turbulent flows) can be computed directly, at least in principle, using a straightforward approach known as DNS. The highlight of a DNS lies in its ability to capture the entire spectrum of scales, and to compute and visualize any quantity of interest that may provide insight to the detailed behavior of turbulent eddies. In a DNS, also known as fully resolved simulation, a spatial grid fine enough to resolve the Kolmogorov scales (smallest length scale) of motion and a highly accurate discretization scheme designed to minimize the numerical errors are required. Such a simulation demands sufficiently powerful computers as the computational cost scales in the order of Reynolds number (Re^3) [3]. Also, a very fine grid with the number of grid points proportional to $Re^{9/4}$ is required, which is often prohibitively difficult to meet with the current state of technology. The requirements of higher order schemes which have little flexibility to complex geometries and higher cost of the computations, limits the usage of DNS to relatively simple applications. With significant increase in computational resources every year, an estimate for the use of DNS to complex industrial applications is expected by the year 2080 [4].

1.2.2 LES

The second approach to turbulence modeling, LES, is a technique intermediate between DNS and RANS methods. LES is based on the energy cascade mechanism, wherein large eddies transfer their kinetic energy to smaller eddies, which in turn transfer

energy to even smaller eddies, and so on until the Kolmogorov scale is reached. At the smallest length scale of motion kinetic energy is dissipated or transformed into heat. In this approach, an attempt is made to compute the large eddies containing information about the geometry and dynamics of the flow exactly, while the effect of the smaller, subgrid scales of turbulence which are somewhat homogenous and universal in behavior is modeled. This results in significant reduction of computational cost compared to a fully resolved simulation. A filtering operation similar to a time averaging approach is employed to separate the small-scale fluctuations from the large-scale structures. The smaller eddies are either poorly resolved or not resolved at all, hence a subgrid scale (SGS) model is used to remove energy from the resolved scales and mimic the energy drain associated with the energy cascade.

Despite the fact that small-scales are modeled using a SGS model, LES remains computationally intensive compared to other available turbulence modeling approaches. This is due to the fact that the separation between large and small-scales in near-wall regions is not clearly understood, and selecting a grid course enough for efficiency and fine enough for accuracy depends on the user. Moreover, simulations have to be run for a much longer time to obtain statistical convergence of the turbulence quantities. To improve the accuracy of LES, a fine grid similar to the one used for DNS is required in near-wall regions, and to compute the large-scales exactly in both space and time, relatively finer grids or higher-order schemes with small time-steps are required. According to Chapman [5], estimated grid resolution requirement for the outer layer of a wall boundary is proportional to $Re^{2/5}$, and for the wall layer the grid resolution scales with $Re^{1.8}$, which results in excessively finer grid requirement at high Re flows. Other

drawbacks include grid selection, numerical discretization, and limitations of the SGS model.

With a simultaneous improvement in computational power and efficiency of SGS modeling, LES is now widely used for studies involving highly three-dimensional (3D) or separated flows where two-equation EVMs often fail to resolve the complex flow features accurately, and in free shear layer flows where the grid resolution requirements are nearly independent of Re. Recently, LES has been successfully applied to certain sector of industrial problems with satisfactory accuracy [6,7], and widespread use for complex engineering applications is expected by the year 2045 [4].

1.2.3 RANS

To date, turbulence models based on the RANS approach are the most common closure models adopted in industrial CFD applications, since these are easy to implement and inexpensive. Based on the Reynolds averaging approach, wherein a quantity is averaged over a time interval much longer than all the time scales of the turbulent flow, the flow variables in the equations of motion are decomposed into a mean and fluctuating part. This operation results in a time-averaged set of equations with an additional term, the Reynolds stress, which arises from the nonlinear convective terms in the original equations of motion. The effect of turbulent fluctuations appears in the Reynolds stress term which must be modeled to close the system of equations. A wide range of models for the turbulence closure problem are available today, ranging from simple algebraic to widely used two-equation models (i.e., k-ε, k-ω), to more complex algebraic Reynolds stress closures.

Over the years, RANS models have improved considerably and have provided reasonable predictions ranging from certain classes of flows which exhibit some degree of universal behavior, for example, the prediction of turbulent boundary layer, to fairly complex flow configurations. However, most of these models have difficulty in dealing with problems for which the details of the geometry are relevant to the turbulence dynamics. This is due to the strong flow-dependent nature of the larger eddies which contribute most to the energy and momentum transfer, and cannot be modeled in the same way for different flows as the smaller eddies which have somewhat universal behavior. Hence, these models more-or-less require some ad hoc adjustments from one flow to another. Moreover, Reynolds averaging suppresses too much information, for example, key characteristics of the turbulent eddies such as frequency, phase, and wavelength of the fluctuating motion are lost which may be important in some practical applications. Nevertheless, given the computational complexity involved with either DNS or pure LES methods, in the near future, complex URANS methods, along with hybrid RANS-LES methods, with more emphasis on the latter will be developed and employed in the industry.

1.2.4 Hybrid RANS-LES

Given the fact that RANS approach is physically inadequate for resolving the large-scale unsteadiness in several engineering applications and LES or DNS are computationally out of reach for now or into the foreseeable future, a new turbulence modeling paradigm called hybrid or bridging models which combine the advantages of RANS approach with those of LES have been developed. These intermediate models have the ability to resolve only the large dynamically important fluctuations without the

burden of resolving the inertial scales. The underlying concept in these strategies is to exploit the computational efficiency of RANS for modeling the flow in near-wall regions with the accuracy of LES for the prediction of momentum, heat and mass transfer in regions of separated flow [4]. Over the last two decades, a bevy of such models with different strategies have been proposed. Few notable approaches are detached-eddy simulation (DES) [8], URANS [9], VLES [10], limited numerical scales (LNS) [11], partially resolved numerical simulation (PRNS) [12], partially integrated transport model (PITM) [13], and PANS [14]. Although the idea behind all these strategies is the same, the rationales of each method are quite distinct. The main differences between these intermediate modeling strategies pertains to three issues: (i) the criteria according to which the RANS and LES zones are partitioned; (ii) the manner in which the two zones interact and interface with one another; and (iii) the filtering operation used to derive the model equations from the base Navier-Stokes equations [15].

Hybrid models require a grid resolution comparable to one used for RANS in near-wall regions and a grid similar to the one used for LES in regions away from the wall. The use of coarse grid spacing in planes parallel to the walls keeps the cost of hybrid simulations comparatively cheaper than LES. Using excessively finer grids is meaningless as the whole point of using a hybrid model is to keep the computational cost low. In general, for a zonal or non-zonal approach (see Sec. 2.5), it is possible for the user to activate LES only in regions of interest by having a fine resolution, which is in a way similar to tagging the regions as RANS or LES, however, this approach is implicit. For example, in flow over a bluff body, a RANS solution is possible by using a coarser grid

all over the domain, and refining the grid only in the wake region gives a hybrid solution with the large-scale structures resolved accurately.

1.3 Limitations of RANS and Hybrid Models

The inadequacies of conventional eddy-viscosity turbulence models in producing physically correct responses to flow transition, relaminarization of flow, streamline curvature, wall roughness, and system rotation effects have been known and documented for some time. Unlike differential Reynolds stress models, which contain a separate transport equation for each component of the Reynolds stress tensor, conventional EVMs do not explicitly contain streamline curvature and/or system rotation dependent terms in their formulation, and hence fail to predict these complex effects. Furthermore, for the accurate prediction of laminar-to-turbulent transition, traditional EVMs typically have to be coupled with empirical transition correlations, or else additional transport equations that include flow transition effects must be added, without which these models predict inaccurate results and are not suitable for addressing boundary layer transition in numerical simulations. Despite these limitations, traditional RANS-based models (i.e., fully turbulent models) are the most common turbulence closure approach adopted in industrial CFD applications, since these models are easy to implement, robust, computationally inexpensive, and can be applied to general grid structures (i.e., both structured and unstructured grids). An EVM sensitive to both RC and flow transition (T) effects would be a useful tool for CFD simulations of many flows of engineering interest, including applications in aerospace, automotive, marine systems, and turbomachinery. Besides the above mentioned limitations, RANS models are also known to perform poorly in highly unsteady flows wherein the details of the geometry are relevant to the

turbulence dynamics, and in prediction of momentum, heat and mass transfer in regions of separated flow.

The near-wall treatment of any modeling approach other than RANS has always been an important issue. Use of complex SGS modeling strategies for LES proved computationally expensive at high Re flows, and an SGS-free LES cannot deal with the wall region of the boundary layer, an exception being using a fine grid and approaching DNS. Given the current state of technology and computational cost involved, LES for complex flow problems is out of reach for now or into the foreseeable future. The other option, hybrid RANS-LES models are gaining popularity in this aspect, wherein RANS models are used for wall-boundary treatment and LES for regions away from the wall. However, a brief survey of literature revealed several weaknesses in currently available hybrid models. They include modeled-stress depletion, grid-induced separation, boundary layer log-layer mismatch, slow LES development in separated shear layers [16], treatment of the interface between RANS and LES regions, and inability to account for T-RC effects.

The obvious solution to the fundamental issues observed in currently available RANS and hybrid RANS-LES models is to propose new formulations that are robust and computationally viable with higher accuracy and resolve most of the weaknesses outlined above. This motivates the development of a new model in the RANS category and a new hybrid model under the non-zonal category.

1.4 Research Statement

The work presented in this research effort seeks primarily to identify several weaknesses inherent in currently available turbulence models and present alternative

techniques for CFD modeling of laminar, transitional, and turbulent flows with sensitivity to streamline curvature and rotational effects. In particular, two turbulence modeling techniques are developed:

- A four-equation RANS-based model capable of predicting both flow transition and streamline curvature and/or system rotation effects accurately.
- A dynamic hybrid RANS-LES model that addresses several deficiencies present in currently available hybrid models with the additional capability of capturing the flow transition and streamline curvature and/or system rotation effects accurately.

Both the proposed modeling techniques are validated against canonical and complex two-dimensional (2D) and 3D test cases to highlight the predictive capability of the models, and also show the importance of using such advanced modeling strategies to obtain improved accuracy in predictions compared to currently available models at a reasonable increase in computational cost.

An overview of this dissertation is as follows. After the introduction (in Chapter I), a brief review of literature pertaining to flow transition effects, curvature effects, and hybrid RANS-LES models is presented in Chapter II. In Chapter III, the objectives of current research work and a list of model validation cases are presented. The concepts and formulations of the new RANS and Hybrid RANS-LES models are presented in Chapter IV. Results obtained from the validation cases of the proposed models are shown in Chapters V-VII, and lastly, conclusions are included in Chapter VIII.

Note: This manuscript is a collection of various conference and journal papers written by the author during the course of this research work. Some of the papers are either published or in the process of publication, and a complete list can be found in Chapter III.

CHAPTER II

LITERATURE REVIEW

This chapter presents a brief overview of literature pertaining to the concepts of boundary layer transition and formation of separation bubbles; transition modeling; rotation and curvature effects; turbulence models with curvature corrections; hybrid RANS-LES approach; and lastly, the MILES scheme. This is not an exhaustive review, however, this body of literature provides valuable insight into the current understanding of the concepts that are relevant to the proposed model development and applications on which the models are tested.

2.1 Laminar-to-Turbulent Transition

Flow transition from an orderly state of laminar to a chaotic state of turbulence occurs through different modes in different applications. Firstly, there is the 'natural transition' mode which is due to the amplification of a weak instability present in the laminar boundary layer, eventually leading to a nonlinear breakdown to fully turbulent flow. Secondly, the 'separation-induced transition' mode, wherein the laminar boundary layer separates under the influence of high adverse pressure gradients (APGs) leading to transition in the separated shear layer. The flow may reattach to the surface as a turbulent boundary layer or stay separated. Thirdly, the 'bypass transition' mode typically observed in turbomachinery applications. Here, transition takes place due to the presence of high levels of disturbances in the freestream. Lastly, the 'relaminarization' mode, wherein the

turbulent boundary layer may relaminarize under the influence of high favorable pressure gradients.

Flow transition from laminar-to-turbulent takes place in the low Re regime where viscous effects play a much more important role than in high Re flows, in which viscous effects are either neglected or restricted to thin regions near body surface. The complex interactions of viscous mechanisms, transition, and separation present an interesting and challenging problem in many industrial applications, including design of airfoils for turbomachinery and lifting surfaces of unmanned aerial vehicles, among others. In these applications, the low Re regime typically extends from $10^5 < Re < 2 \times 10^6$ [17].

Another interesting and complex mechanism observed during transition is the formation of a laminar separation bubble (LSB). To explain the concept of the formation of a LSB, consider an airfoil under the influence of low freestream turbulence intensity and low Re flows. In such a scenario, boundary layers are initially laminar and are prone to separation if the near wall fluid has insufficient momentum to overcome even mild APGs. Once separated, the laminar boundary layer forms a shear layer that may quickly undergo transition to turbulence and reattach to the airfoil surface in the form of a turbulent boundary layer, leading to the formation of a LSB [18,19]. Shear layer transition occurs due to the amplification of flow instabilities, which cause the shear layer to roll up and form vortices that play a vital role in bubble formation. Inside a LSB, a 'dead air' region of low velocity is observed under the detached shear layer immediately after separation, resulting in the formation of a nearly constant region of pressure on the airfoil surface. A strong recirculation zone is also observed near the downstream region of bubble. Momentum transfer due to turbulent mixing eliminates the reverse flow due to

entrainment of high speed outer fluid and finally flow reattaches to the airfoil surface [20].

Depending on the size of bubble, LSB's are typically categorized as either short or long bubbles [21]. A long bubble occupies significant portion of the airfoil surface and affects the inviscid pressure and velocity distributions over much of the airfoil surface, whereas a short bubble covers only a small portion of the airfoil surface and only have a local effect on the pressure and velocity distributions. The existence of a separation bubble on the airfoil surface acts as a barrier to obtaining high aerodynamic performance in the low Re regime, and is exhibited by a decrease in lift and an increase in drag values [22].

For years, traditional EVMs, primarily developed for predicting only fully turbulent flows in high Re applications were used for the prediction of flows in low Re applications. This often led to the inaccurate prediction of critical flow characteristics as the effects from laminar and transition zones were neglected. The accuracy of everyday industrial CFD simulations can only be improved by designing turbulence models, be it RANS, LES, or hybrid for a wide range of flow regimes including low Re effects.

2.2 Transition-Sensitive Turbulence Models

Recent advances in eddy-viscosity based modeling approaches have resulted in the development of several EVMs modified to account for flow transition effects and have demonstrated varying degree of success. A few notable approaches to predict transition are: 1) use of zonal modeling with laminar and turbulent flow regions defined a priori; 2) use of unmodified low Re EVMs; 3) coupling of fully turbulent models with empirical transition correlations; and 4) addition of transport equations to the high Re

turbulence model equations. The first approach is necessarily highly user dependent and requires a great deal of expertise to be successfully applied for any particular application. The remaining approaches seek to provide a general transitional flow capability. With regard to the second approach, several low-Re models have been developed wherein wall damping functions are used to trigger the onset of transition. While several of these turbulence models are known to qualitatively mimic transition, careful investigation has shown that this behavior is a numerical artifact rather than true predictive capability, and that the transitional behavior tends to be highly dependent on simulation aspects such as mesh topology and boundary conditions [23,24]. It was also shown that certain forms of low Re k-ε models and two of the widely used fully turbulent models, SA [25] and Menter SST k-ω [26], did exhibit apparent transition behavior dependent on initial conditions and methods of solutions [27]. For example, using excessively finer grids and freestream turbulence values below some threshold, both SA and SST k-ω models did predict transition for the flow over an airfoil [28]. Although some of the standard low Re models successfully predicted bypass transition which is mostly dominated by diffusion effects, the ability of these models to predict transition is often described as "pseudo transition", as the apparent transition behavior (sometimes grid dependent) is not because of any physics built into the model rather simply a numerical artifact.

Turbulence models based on the third approach use appropriate intermittency factors to bridge the pre- and post-transitional boundary layers, and to enforce transition [29,30]. Dhawan and Narasimha [31] proposed a highly empirical approach with some success, in which a generalized intermittency distribution function was proposed based on correlations from experimental data. Steelant and Dick [30] proposed a transport

equation for intermittency and coupled with two sets of conditioned Navier-Stokes equations. However, the usage of two sets of strongly coupled equations makes the model not compatible with general purpose CFD solvers. Suzen and Huang [29] proposed a transport equation for intermittency factor and coupled with the SST k-ω model. The proposed equation combined the features of two existing transition models using a blending function to resolve the flow transition effects, including the influences of freestream turbulence and pressure gradients. Several difficulties arise in the aforementioned application of models, however, since they tend to be based on difficult to generalize quantities such as boundary layer momentum thickness or distance downstream of the boundary layer start location.

These difficulties have led to the development of a number of models designed to predict transition while being easily implemented into general-purpose flow solvers. These models, based on the fourth approach, are widely popular and are favored by the industry [32-34]. Wang and Perot [32] developed a modified version of the turbulent potential model [35] to predict transition in boundary layer flows. Unlike the classic Reynolds Stress Transport (RST) models which are difficult to implement and require significant computational resources, the turbulent potential model is a reformulation of the RST equations that retains only the non-equilibrium and energy distribution physics making it relatively cheaper and easy to implement. Two additional transport equations, k and ε, were solved to model the source terms in the turbulent potential evolution equations. The modified turbulent potential model successfully predicted both natural and bypass transition with a computational cost equivalent to that of a two-equation model. Menter et al. [33] developed a correlation-based transition model with two additional

transport equations, first is an intermittency equation used to trigger the onset of transition, and the second for transition onset criteria in terms of momentum thickness Reynolds number. Unlike other available transition models, these transport equations provide a framework for the implementation of correlation-based models into general-purpose CFD solvers, and the physics of transition is entirely dependent on the experimental correlations provided to the model. This allows the model to be used for predicting wider transition mechanisms, however appropriate correlations have to be provided by the user. Another widely used transition-sensitive turbulence model, developed by Walters and Cokljat [34], solves additional transport equations for predicting flow transition phenomena that rely on local information. The model, k-k_L-ω, is capable of predicting both natural and bypass transition without the requirement of any transition mechanism based correlations from the user, and is suitable for straightforward implementation within RANS methods. In the present study, this model was used as a baseline version for the development of a curvature corrected version of the model. The k-k_L-ω model is described in detail in Sec. 4.2.1.

Other turbulence modeling approaches available for predicting transitional flows include linear or nonlinear parabolized stability equations; parallel and linear stability theories, such as the e^N method [36]; and more computationally intensive approaches based on LES and DNS methods. The e^N method coupled with a RANS solver was adopted in many studies [37,38], wherein the Orr-Sommerfeld equation is solved to evaluate the local growth of unstable waves based on the velocity and temperature profiles of the body. In these models, flow transition takes place when the amplification of the most unstable Tollmien-Schlichting waves [39] reach a certain critical value.

However, these methods are difficult to implement as they require numerous nonlocal operations, and are not compatible with general-purpose CFD solvers as a priori knowledge of the geometry and grid topology are required. DNS and LES methods are mostly used as research tools, given their excessive computational cost requirement for engineering applications. Moreover, these models require proper specification of the external disturbance level and structure which is a challenge that needs to be solved [40,41].

2.3 Rotation and Curvature Effects

The effect of body forces arising from system rotation or streamline curvature on shear layers typically results in the alteration of the mean flow field, intensity, and turbulence structure. For example, in an imposed rotation of reference frame or simply in rotating flows which have applications in rotating fluid machinery, Coriolis forces are produced. These forces can either have a stabilizing or destabilizing effect on the flow depending on the interaction of the body forces with the mean shear layers. Here, stabilization refers to the suppression of turbulence, and at higher rotational speeds, this effect may result in the laminarization of flow. In contrast, enhancement of turbulence production refers to the destabilizing effect.

Similarly, the presence of a wall curvature, either convex or concave, results in an additional strain rate which can either enhance or suppress the turbulence intensity in the near-wall flow regions. As discussed by Durbin [42], convex curvature tends to reduce turbulence intensity while concave curvature tends to enhance it. These effects of curvature are determined by the direction of rotation: along a convex wall, the strain rate tensor rotates in the same direction as the local vorticity vector; along a concave wall, the

two rotations are in opposite directions. Co-rotation suppresses turbulence and counter-rotation enhances it.

2.4 Curvature Corrected Turbulence Models

Methods for incorporating RC corrections into linear eddy-viscosity closures have been investigated for decades. These methods have attempted to introduce the suppression and/or enhancement of turbulent production in the presence of stabilizing and/or destabilizing rotation [43]. Initial attempts based on ad hoc modifications were shown to predict RC effects successfully for the flows on which they were tested [44-46], however, none of the models satisfied mathematical invariance and frame indifference principles. As an alternative, a number of linear EVMs sensitized to RC effects have been proposed in the recent past, which were successful for a wider range of flows and the corrections satisfied mathematical invariance principles as well. The most common approaches followed in these models include: multiplication of either the eddy-viscosity or the eddy-viscosity coefficient with an empirical function sensitive to rotation effects [47,48]; and modification of turbulent length scale by including rotational dependent terms in the production or dissipation rate equations [45]. Spalart and Shur [49] proposed a curvature-corrected SA model by multiplying the production term of original SA model [25] with an empirical function calculated in terms of the local mean velocity gradients. This approach was later implemented in the SST k-ω model as well [50]. Recently, Dhakal and Walters [51] proposed a curvature corrected SST k-ω-v^2 model, a variant of the SST k-ω model corrected to system rotation and streamline curvature. The physical effects of curvature and rotation on turbulence structure enter the model through the added transport equation for a structural variable v^2, analogous to a transverse turbulent

velocity scale. The added transport equation enhances the stability of the curvature-corrected model versus several previous attempts, and also incorporates additional turbulence structure history effects into the calculation of the eddy-viscosity.

Reynolds stress models (RSMs) explicitly contain rotation and curvature terms in the turbulence equations and have a natural advantage over linear EVMs. However, due to excessive computational cost and numerical stiffness, other alternatives such as explicit algebraic stress models (ASMs) were derived by subjecting the anisotropy equation to the weak equilibrium assumption [52-54]. The curvature corrections in these models are based on mathematically consistent application of invariance and frame indifference principles. Moreover, these models address second-order RC effects related to stress anisotropy that cannot be reproduced with linear models in any form. The disadvantages of ASMs lie in their complexity and the requirement of the introduction of at least a portion of the Reynolds stress explicitly, rather than using a linear eddy-viscosity formulation that can be incorporated implicitly via the diffusion term. Many curvature-corrected EVMs can be placed in context by considering them as linearizations of more theoretically complete ASMs. For example, York et al. [48] derived a semi-implicit expression for the eddy-viscosity coefficient C_μ by linearizing the explicit algebraic anisotropy tensor with respect to the mean strain rate, and used it to modify the eddy-viscosity to develop a curvature-corrected model. Dhakal and Walters [51] further simplified this expression for C_μ and proposed a simpler explicit expression to develop a curvature-corrected variant of the SST k-ω model. The four-equation model proposed in this work follows the approach by Dhakal and Walters [51], and hence is based in large part on the components or simplification of ASMs available in the literature [52-54].

2.5 Hybrid RANS-LES Modeling

The objective of a hybrid modeling approach is to extract important large-scale unsteady features of a turbulent flow at minimal computational expense. This results in a hybrid model resolving more scales of motion compared to a RANS simulation and significantly lesser scales than a traditional LES approach. Hybrid models can be classified into zonal and non-zonal approaches. In a zonal approach, the user explicitly tags some regions of the computational domain as RANS and others as LES. Models based on the zonal approach are simple to develop and allow the user to pick any combination of RANS and LES models, however, the matching grid plane between the two regions, generally defined in terms of grid spacing, has to be pre-selected by the user and is grid dependent. Although the interface location can be automated, for certain problems such as wall-bounded flows, the matching grid plane location has a significant impact on the computed solution and results in wrongful prediction of turbulence quantities and mean flow statistics in the wall-layer [55]. A number of zonal hybrid models have been proposed and investigated over the years [56-57]. Most of them solved unsteady forms of boundary layer equations in the near-wall layer of prescribed thickness and used a mixing-length model to obtain the eddy-viscosity. The wall shear stress or other quantities obtained from the RANS solution are fed into the LES solution as a boundary condition at the interface location.

The zonal methods pose a range of questions, one of them being the treatment of interface region between the RANS and LES zones. Most zonal methods bridge the RANS and LES regions by interchanging velocities, modeled turbulent energy, and turbulent viscosity at the interface. The question arises at this location, wherein the

transfer of quantities from the RANS zone defined by time-averaging to the LES zone defined by volume averaging often results in inconsistencies (i.e., incorrect prediction of velocity and skin friction profiles). Many studies have indicated the importance of handling the RANS-LES interface region for obtaining accurate results in the LES region. Furthermore, the response of a RANS model, which is defined on the closure assumptions formulated in reference to steady flows, to the highly unsteady motion imposed on it by the LES model is questionable. A more common issue observed in most of the zonal methods is the optimum distance required for the placement of interface region which is problem dependent. For example, in a channel flow, studies have indicated that the interface location too close to the wall results in too low levels of eddy viscosity, and when the interface is moved away from the wall, better results were observed. However, the use of RANS model over larger regions is questionable in a hybrid approach [58]. These issues and many more concerning the RANS-LES interface region remain an active area of research [59-61].

Hybrid models based on the non-zonal approach utilize some kind of parameter to effectively transition from a RANS to LES type flowfield, hence refraining the user from tagging certain regions of flowfield as RANS and others as LES. For these models, no matching grid plane and no interface conditions between the RANS and LES regions are required. A popular model based on the non-zonal approach is the DES, proposed by Spalart et al. [8]. In this model, the transition from a RANS to LES type flowfield is solely based on the grid spacing. The DES model utilizes the one-equation SA and SGS models for the RANS and LES regions, respectively. Although the model was successful in flows with massive separation, several weaknesses of the model were outlined in a

recent review article by Spalart [16]. These include modeled-stress depletion, grid-induced separation, boundary layer log-layer mismatch, and slow development of LES content in separated shear layers. Other variants namely, zonal DES [62], shielded DES [63], delayed DES (DDES) [64], and improved delayed DES [65], have been proposed to mitigate some of the issues present in the original version of DES model, however, most of them were based on ad-hoc modifications and resulted in little success.

A number of other modeling approaches have been proposed in the category of hybrid models. Girimaji [14] proposed the PANS bridging method capable of producing fully averaged (RANS) to fully resolved (DNS) solutions. In the model, the extent of partial averaging is controlled via two parameters: the unresolved-to-total ratios of kinetic energy and dissipation. As the filter-control parameters which dictate the amount of scales to be resolved are varied, the model transitions smoothly from RANS to DNS. The uniqueness of the model lies in the decomposition of the velocity based on kinetic energy content rather than cutoff wavenumber. The PANS model can be viewed as LES with an implicit filter and a two-equation sub-filter closure. PITM, a subgrid-scale model involving all the transport equations of the SGS stresses was proposed by Chaouat and Schiestel [13]. In this model, as the filter cutoff location is varied, the SGS model varies continuously between a DNS and RSM [66]. Unlike PANS, which is derived from fractional energy evolution considerations in physical space, the PITM is derived from spectral partitioning. VLES, a concept originally proposed by Speziale [10], is based on the filtering of only the larger part of turbulent fluctuations as compared to a conventional LES approach. This approach necessitates the use of a complex sub-grid modeling strategy for modeling the unresolved fluctuations. A filter width is used which dictates

the model predictions to be either RANS or LES. The VLES can be thought of as an unsteady, 3D turbulence model acting as a link between traditional LES and URANS approaches. Shih and Liu [12] proposed a universal modeling approach (PRNS) wherein the very large-scales of turbulence are directly calculated, and the effects of unresolved scales are accounted by an eddy viscosity model with additional nonlinear source terms for rotation effects. The PRNS approach is based on a temporal filter with a fixed filter width to define the large-scales and a sub-scale model without grid spacing parameters in its constitutive equation. Hence, the Navier-Stokes equations used in this model are temporally filtered, similar to other spatially filtered LES approaches. The use of a temporal filter results in a set of PRNS equations which are grid invariant (i.e., valid for any type of grids) and allows the equations to evolve from DNS, LES, and towards RANS as dictated by the width of the temporal filter.

To date, very few hybrid models under the category of both zonal and non-zonal approaches are available in the literature that are sensitized to either flow transition effects or RC effects, and to the author's knowledge, none of the models were designed to include both the complex effects of transition and curvature in their formulation. A turbulence model, be it RANS or hybrid, sensitive to T-RC effects would be of substantial interest to the CFD community and also a useful tool for CFD simulations of many flows of engineering interest, including applications in aerospace, automotive, marine systems, and turbomachinery.

2.6 MILES

As explained before (see Sec. 1.2.2), traditional LES approaches utilize an SGS model to remove kinetic energy from the resolved scales and mimic the energy drain

associated with the energy cascade. The SGS models are explicitly introduced in the simulation for closure of the low-pass filtered Navier-Stokes equations. Some of the widely popular SGS closures include algebraic models, scale similarity models, and differential stress models [67-70]. As an alternative, monotonically integrated LES (MILES) approach was developed which involves solving the unfiltered Navier-Stokes equations using high-resolution monotone algorithms or simply using an upwind scheme. In this SGS free approach, nonlinear high-frequency filters built into the convection discretization schemes provide the SGS models implicitly [71]. The monotone algorithms may include the flux-corrected transport method or the piecewise parabolic method.

The main difference between a MILES and traditional LES approach is the use of an explicit SGS model in the latter, and in the way convective flux functions are derived. To perform a MILES simulation, the grid resolution has to be fine enough such that the cutoff wave number lies in the inertial subrange, and the kinetic energy in some way has to be channeled out from the resolved scales near the cutoff wave number. The MILES scheme has been tested on various applications successfully which can be found in Refs. [72-75].

CHAPTER III

RESEARCH OBJECTIVES AND APPROACH

3.1 Research Objectives

The primary objectives of the work presented in this research effort are:

- To develop a physics-based four-equation EVM capable of predicting laminar, transitional, and turbulent flows with sensitivity to streamline curvature and rotational effects.
- To validate the four-equation model on canonical test cases intended to verify the correct behavior of the model in the presence of T-RC effects, followed by testing the model on more complex and realistic engineering flows.
- To implement the developed EVM combined with a LES scheme in a new hybrid modeling framework, dynamic hybrid RANS-LES (DHRL).
- To validate the DHRL model on canonical test cases and complex flow applications.

The overall goal is, firstly, to develop simple and robust turbulence models that will improve the predictive capability of RANS and hybrid RANS-LES-based CFD simulations; secondly, validate the models against complex flows to highlight the importance of using advanced turbulence modeling techniques in obtaining solutions within engineering accuracy and at a reasonable computational cost; and thirdly, to provide a practical tool to the CFD community that can be used in a wide variety of disciplines and industries.

3.2 Approach

Initially, user-defined subroutines for both the proposed models were written by the author in the C language. Later, the models were incorporated into the commercially available finite volume solver ANSYS FLUENT using the user-defined function (UDF) capability available with the solver. For validation of the proposed RANS model, simulations were initially performed on canonical 2D cases, which include channel flow (both nonrotating and rotating flows) and zero pressure gradient (ZPG) flat plate cases. After obtaining satisfactory results, the RANS model was tested on various complex cases, including 2D circular cylinder and elliptic airfoil, and 3D axisymmetric hill. A similar strategy was followed with the validation of the DHRL model as well. Table 3.1 summarizes the list of test cases on which the models were tested. References for the test cases are also included.

Table 3.1 List of test cases for current research work

#	Case Description	Models Tested[1]	References
1	2D channel flow (a) Nonrotating flow (b) Rotating flow	k-k_L-ω-v^2	[76]
2	2D ZPG flat plate – 3 different cases	k-k_L-ω-v^2	[76,77]
3	2D circular cylinder cases	k-k_L-ω-v^2	[76,77]
4	Elliptic airfoil cases	k-k_L-ω-v^2	[17,76-78]
5	3D axisymmetric hill	k-k_L-ω-v^2	[79]
6	3D channel flow (a) Nonrotating flow (b) Rotating flow	k-k_L-ω-v^2, DHRL	[80]
7	3D ZPG flat plate – 3 different cases	k-k_L-ω-v^2, DHRL	[80]
8	3D circular cylinder cases	k-k_L-ω-v^2, DHRL	[80]

[1] Results obtained from the proposed models are compared with other available RANS and Hybrid RANS-LES models accordingly

3.3 Publications

A complete list of articles (both journal and conference) and presentations published as an outcome of this research effort are given below:

1. Chitta, V., Dhakal, T. P., and Walters, D. K., 2012, "A Four-Equation Variant of the k-k_L-ω model Sensitized to Rotation and Curvature Effects," Presented at the Ninth MSU-UAB Conference on Differential Equations & Computational Simulations, Mississippi State, MS.

2. Chitta, V., Dhakal, T. P., and Walters, D. K., 2013, "Development and Application of A New-Four Equation Eddy-Viscosity Model for Flows with Transition, Curvature and Rotation Effects," Paper No. FEDSM2013-16372, Proceedings of ASME 2013 Fluids Engineering Summer Meeting, Incline Village, Nevada.

3. Chitta, V., Jamal, T., and Walters, D. K., 2014, "Numerical Investigation of Low-Reynolds Number Airfoil Flows Using Transition-Sensitive and Fully Turbulent RANS Models," Paper No. FEDSM2014-21700, Proceedings of ASME 2014 Joint US-European Fluids Engineering Summer Meeting, Chicago, Illinois.

4. Chitta, V., and Walters, D. K., 2014, "A Dynamic Hybrid RANS/LES Model Sensitive to Transition and Rotation/Curvature Effects," Presented at the Tenth MSU-UAB Conference on Differential Equations & Computational Simulations, Mississippi State, MS.

5. Robertson, E. D., Chitta, V., Bhushan, S., and Walters, D. K., 2014, "Turbulent and Vortical Structure Analysis of the Vortex Breakdown Phenomenon over Delta Wing Geometries," Presented at the Tenth MSU-UAB Conference on Differential Equations & Computational Simulations, Mississippi State, MS.

6. Robertson, E. D., Chitta, V., Bhushan, S., and Walters, D. K., 2014, "On the Vortex Breakdown Phenomenon in High Angle of Attack Flows Over Delta Wing Geometries," Paper No. IMECE2014-39354, Proceedings of ASME 2014 International Mechanical Engineering Congress & Exposition, Montreal, Canada.

7. Chitta, V., Dhakal, T. P., and Walters, D. K., 2015, "Sensitization of a Transition-Sensitive Linear Eddy-Viscosity Model to Rotation and Curvature Effects," ASME Journal of Fluids Engineering, 137, p. 031207.

8. Chitta, V., Jamal, T., and Walters, D. K., 2015, "Numerical Study of Vortical Separation from a Three-Dimensional Hill Using Eddy-Viscosity Models," Paper No. AJK2015-03223, Proceedings of ASME-JSME-KSME Joint Fluids Engineering Conference, Seoul, Korea.

9. Chitta, V., and Walters, D. K., 2015, "A Hybrid RANS-LES Modeling Methodology Sensitized to Transitional and Curvature/Rotation Effects," Paper No. IMECE2015-53155, Proceedings of ASME 2015 International Mechanical Engineering Congress & Exposition, Houston, Texas.

10. Chitta, V., and Walters, D. K., "Computational Fluid Dynamics Study of Separated Flow over A Three-Dimensional Axisymmetric Hill," *Journal in preparation*.

11. Chitta, V., and Walters, D. K., "A Dynamic Hybrid RANS-LES Model for Transitional and Rotational Flows," *Journal in preparation*.

CHAPTER IV

MODEL DEVELOPMENT

In this chapter, firstly, a brief discussion on the turbulence closure problem is given. This is followed by the concept and development of the four-equation RANS model and the hybrid model in Secs. 4.2 and 4.3, respectively.

4.1 Governing Equations of Fluid Flow in RANS-Based Models

The RANS (time-averaged) equations for incompressible, isothermal, and Newtonian fluids with negligible body forces can be written in standard tensor notation as

$$\frac{\partial \overline{u_i}}{\partial x_i} = 0 \tag{4.1}$$

$$\frac{\partial \overline{u_i}}{\partial t} + \overline{u_j}\frac{\partial \overline{u_i}}{\partial x_j} = -\frac{1}{\rho}\frac{\partial \overline{p}}{\partial x_i} + \nu\frac{\partial^2 \overline{u_i}}{\partial x_j \partial x_j} - \frac{\partial \overline{u_i' u_j'}}{\partial x_j} \tag{4.2}$$

In the continuity (4.1) and momentum equations (4.2), the mean (time-averaged) quantities are denoted by an overbar and the fluctuating (instantaneous) quantities are denoted by a prime. The left hand side of Eq. (4-2) represents the unsteady and convective terms (first and second terms), and the right hand side represents the pressure gradient, viscous stresses, and Reynolds stresses (first, second, and third terms). The correlation of the fluctuating velocity components (four components for 2D flows and nine components for 3D flows) is represented by the nonlinear Reynolds stresses which result from the time-averaged effect of turbulent convection. In RANS-based models,

both transitional and turbulent fluctuations are modeled using the Reynolds stress tensor, and smaller values are assigned to these stresses to model steady laminar flows. Theoretically, turbulent fluctuations are neglected in laminar flows, however in a strict sense, for any time varying velocity field, even if the velocity fluctuations are not due to turbulence, the Reynolds stresses are nonzero.

The closure of the momentum equation (i.e., to solve the time-averaged governing equation (4.2)) is possible by modeling the Reynolds stress term. Most common method of RANS-based CFD is to use a single parameter—the eddy-viscosity—to model the Reynolds stresses. The widely used RANS-based models adopt the Boussinesq hypothesis, wherein a linear relationship is assumed between the Reynolds stresses and the strain rate tensor S_{ij}:

$$\overline{u_i' u_j'} - \frac{1}{3}\overline{u_k' u_k'}\delta_{ij} = -2\nu_T S_{ij} \tag{4.3}$$

where ν_T is the eddy-viscosity and δ_{ij} is the Kronecker delta. Equation (4.3) can also be written relating the turbulent kinetic energy (TKE) denoted by k as

$$\overline{u_i' u_j'} - \frac{2}{3}k\delta_{ij} = -2\nu_T S_{ij} \tag{4.4}$$

where $k = \frac{1}{2}\overline{u_k' u_k'}$.

The two-equation models, for example, turbulence models based on the k-ω or k-ε framework, solve two additional equations to obtain the turbulence quantities which are used to compute the eddy-viscosity. The proposed four-equation EVM addresses laminar, transitional, and turbulent flows with an additional capability of resolving RC effects entirely within the framework of Reynolds-averaging.

4.2 k-k_L-ω-v^2 Model Development and Formulation

The new EVM developed herein is based on the k-ω framework and employs four transport equations in addition to the mean flow equations, one for each scalar turbulence variable—TKE (denoted in this model as k_T), laminar kinetic energy (LKE) (k_L), scale-determining variable (ω), and structural variable (v^2). The model inherits its first three transport equations from the transition-sensitive k-k_L-ω model and the fourth transport equation v^2 is defined similar to the one proposed in Dhakal and Walters, [51]. The concepts of incorporating transition and curvature effects into the model are discussed in Secs. 4.2.1 and 4.2.2, respectively. The governing equations of the new model are given in Sec. 4.2.3. Here, only final transport equations of the new model are given and differences between the new model form and that in Refs. [34,51] are discussed. A complete definition of the terms and model constants are skipped due to their availability in the literature.

4.2.1 Modeling Transition Effects

The phenomenological (physics-based) k-k_L-ω model is a three-equation eddy-viscosity type based on the LKE concept [81]. The model reproduces laminar, transitional, and turbulent flows without the use of any intermittency factors or empirical correlations. It is currently used in the commercial CFD code ANSYS FLUENT and the open source CFD library OpenFOAM, among others. The main advantages of this single-point model are that it is versatile, can handle flows in complex geometries, and can be easily implemented for the prediction of all three flow regimes. Single point modeling refers to the determination of all new unknowns in the time-averaged equations based solely on the local values of the other variables. For example, in zero equation models,

using algebraic relations, the unknown Reynolds stress components can be related to the mean flow variables. The concept and model development are documented in the literature [34] and is described here briefly.

To understand the physics and major concepts embodied in the transition-sensitive part of the model, consider the boundary layer which can be differentiated into three regions – pretransitional (i.e., nonturbulent), transitional, and post-transitional (i.e., turbulent). In the presence of freestream turbulence (Tu_∞), the mean velocity profile in the pretransitional region resembles a laminar boundary layer. As Tu_∞ is increased, the momentum increases in the inner layer and decreases in the outer layer of the velocity profile. This results in a noticeably distorted profile, even for lower values of Tu_∞ in the range of 1% [82] and is accompanied by the development of relatively high-amplitude streamwise fluctuations. This process is followed by an augmentation of skin friction and heat transfer in the pretransitional region. Eventually, the breakdown of streamwise fluctuations takes place and bypass transition is observed [83]. Generally for incompressible flows, boundary layer transition is of two types – bypass and natural transition. Flow transition caused by Tu_∞ affecting the pretransitional boundary layer by pressure fluctuations and diffusion is bypass transition, and flow transition emanating from the breakdown of amplified disturbances within the boundary layer is natural transition [84]. Commonly, in the presence of environmental disturbances, bypass transition is far more observed compared to natural transition which is usually seen under well controlled conditions or with artificial forcing.

The velocity fluctuations—Klebanoff modes [85] or streaky structures—in the pretransitional region are known to be structurally and dynamically very different from

turbulent fluctuations [86]. The energy contained in these fluctuations is called the LKE, a concept first proposed by Mayle and Schulz [84]. In the present model, the development of these fluctuations is represented by an additional transport equation k_L. The development and amplification of k_L is based on the "splat mechanism" [87], which states that the wall redirects the normal fluctuation into a streamwise component, thereby creating local pressure gradients in the boundary layer which cause disturbance amplification. Based on the assumption that "splats" occur only for eddies with large length scales relative to the wall distance, the turbulent energy spectrum is divided into wall-limited (large-scales) and non-wall-limited (small-scales) sections in the near-wall region. The cutoff eddy size is defined such that smaller scales contribute to turbulence production and larger scales (near-wall) contribute to the production of nonturbulent fluctuations.

In the model, flow transition is initiated based on the concept of shear-sheltering and consideration of relevant time scales for nonlinear disturbance amplification and dissipation. Shear-sheltering refers to the damping of turbulence dynamics that occurs in thin regions of high vorticity [88]. Its main effect is to inhibit nonlinear turbulence breakdown mechanisms in the pretransitional boundary layer. Transition initiation is governed by the use of a local dimensionless quantity which is the ratio between the turbulent production time scale and the molecular diffusion time scale. When this ratio is small, pressure strain is suppressed and one-component fluctuations are generated. Once this ratio reaches a critical value, the pressure strain term quickly increases in magnitude to generate 3D fluctuations leading to the onset of transition. This mechanism is represented in the model by a transfer of energy from the streamwise fluctuations to the

turbulent fluctuations via the pressure strain terms. The onset of transition can be defined as the upstream location where the first turbulent spots are generated. Generally, these spots are not confined to a single location, instead spread over a distance. The total fluctuation energy which equals the sum of streamwise fluctuations and turbulent fluctuations is interpreted as energy distribution rather than production or dissipation. After transition initiation, the effects of shear-sheltering are restricted to the viscous sublayer in the turbulent boundary layer.

In the post-transitional region, the model predicts a fully turbulent boundary layer and almost all of the fluctuation energy is turbulent in nature. However, small amount of k_L is still present in the viscous sublayer due to the presence of streamwise-oriented streaky structures which bear a resemblance to those in the pretransitional region. The model is capable of predicting both natural and mixed mode (i.e., natural and bypass) transition and the related terms are included in the transport equations.

4.2.2 Modeling Curvature Effects

The most common practice for including RC effects in the eddy-viscosity class of models is to modify the eddy viscosity definition based on the mean velocity gradients. This approach is followed in the proposed four-equation EVM as well. The physical effects of curvature and rotation on turbulence structure enter the model through the added transport equation for a structural variable v^2. The framework for the v^2 transport equation is borrowed from the curvature-corrected SST k-ω-v^2 model. The modified eddy-viscosity in the new model is constrained to reduce to the original (k-k_L-ω) model definition in nonrotating flows or in regions with negligible RC effects. This is necessary to ensure that the new model results be identical to the ones predicted by the standard k-

k_L-ω model in regions of the flowfield with negligible RC effects. In the proposed model, turbulence enhancement or attenuation is translated by an increase or reduction of eddy-viscosity depending on the type of wall curvature present (i.e., convex or concave). Interested readers can refer to Dhakal and Walters [51] for the derivation of the v^2 equation.

4.2.3 Model Formulation

Here, the goal is to develop a RANS model sensitive to both T-RC effects. For this sake, the v^2 equation, as explained earlier, is redefined and blended with the transition-sensitive k-k_L-ω model. The terms in the v^2 equation are defined in a way similar to the terms in the k_T equation, such that in the absence of any flow rotation and/or streamline curvature effects, the proposed model behaves identical to the parent k-k_L-ω model. To begin with, consider the transport equations of the proposed model:

$$\frac{Dk_T}{Dt} = P_{k_T} + R_{BP} + R_{NAT} - \omega k_T - D_T + \frac{\partial}{\partial x_j}\left[\left(\nu + \frac{\alpha_T}{\sigma_K}\right)\frac{\partial k_T}{\partial x_j}\right] \tag{4.5}$$

$$\frac{Dk_L}{Dt} = P_{k_L} - R_{BP} - R_{NAT} - D_L + \frac{\partial}{\partial x_j}\left[\nu\frac{\partial k_L}{\partial x_j}\right] \tag{4.6}$$

$$\frac{D\omega}{Dt} = \sqrt{\frac{k_T}{v^2}}C_{\omega 1}\frac{\omega}{k_T}P_{k_T} + \left(\frac{C_{\omega R}}{f_W} - 1\right)\frac{\omega}{k_T}(R_{BP} + R_{NAT}) - C_{\omega 2}\omega^2 f_W^2 + C_{\omega 3}f_\omega \alpha_T f_W^2\frac{\sqrt{k_T}}{d^3} + \frac{\partial}{\partial x_j}\left[\left(\nu + \frac{\alpha_T}{\sigma_\omega}\right)\frac{\partial \omega}{\partial x_j}\right] \tag{4.7}$$

$$\frac{Dv^2}{Dt} = \frac{v^2}{k_T}\left[P_{k_T} + R_{BP} + R_{NAT}\right] - v^2\omega - D_v + \psi\left(\eta_{eff}^2 k_T - v^2\right) + \frac{\partial}{\partial x_j}\left[\left(\nu + \frac{\alpha_T}{\sigma_K}\right)\frac{\partial v^2}{\partial x_j}\right] \tag{4.8}$$

The model equations (4.5) and (4.6) are similar to the transport equations in Walters and Cokljat [34]. In the equation for specific dissipation rate (4.7), only the fully

turbulent production (first term on the right-hand side) is modified to include the effects from v^2, while the remaining terms are similar to the transport equation in Walters and Cokljat [34]. In the v^2 equation (4.8), the fully turbulent production, destruction, and gradient transport terms (first, second and third, and fifth terms on the right-hand side) are analogous to the similar terms in the k_T, k_L, and ω equations. Here, the anisotropic (near-wall) dissipation term for v^2 is defined as

$$D_v = \nu \frac{\partial \sqrt{v^2}}{\partial x_j} \frac{\partial \sqrt{v^2}}{\partial x_j} \tag{4.9}$$

The production terms for TKE and LKE are modeled as

$$P_{k_T} = \nu_{T,s} S^2 \tag{4.10}$$

$$P_{k_L} = \nu_{T,l} S^2 \tag{4.11}$$

In the proposed model, the small-scale eddy-viscosity ($\nu_{T,s}$) is modified to incorporate the RC effects via the effective small-scale turbulence ($k_{T,s}$) and is proposed as

$$\nu_{T,s} = f_v f_{INT} C_\mu \sqrt{k_{T,s}} \lambda_{eff} \tag{4.12}$$

where $k_{T,s}$ is defined as

$$k_{T,s} = f_{SS} f_W v^2 \tag{4.13}$$

The viscous damping function (f_v), intermittency damping function (f_{INT}), turbulent viscosity coefficient (C_μ), effective turbulence length scale (λ_{eff}), shear-sheltering damping function (f_{SS}), and wall damping function (f_W) are identical to the definitions proposed in Walters and Cokljat [34]. In regions of the flowfield with negligible RC effects, the modified small-scale eddy-viscosity $\nu_{T,s}$ returns to its standard form as defined in Walters and Cokljat [34] and the proposed model behaves identical to the standard k-k_L-ω model. Similarly, the large-scale turbulence contribution is modified as

$$k_{T,l} = v^2 - k_{T,s} \tag{4.14}$$

and the large-scale (nonturbulent) eddy-viscosity is modeled as

$$\nu_{T,l} = min\left\{ f_{\tau,l} C_{11} \left(\frac{\Omega \lambda_{eff}^2}{\nu}\right) \sqrt{k_{T,l}} \lambda_{eff} + \sqrt{\frac{v^2}{k_T}} \beta_{TS} C_{12} Re_\Omega \Omega d^2,\ \frac{0.5\,(k_L + k_{T,l})}{S} \right\} \tag{4.15}$$

In Eq. (4.15), the wall distance d is modified as

$$d = \frac{\lambda_{eff}}{C_\lambda} \tag{4.16}$$

In regions far from the walls and in the freestream, $k_{T,s} \rightarrow k_T$ and $k_{T,l} \rightarrow 0$, and the splat mechanism becomes nonexistent.

The curvature effects enter the proposed model via the RC term (fourth term on the right-hand side of Eq. (4.8)) which carries a definition similar to the one proposed in Dhakal and Walters [51]. To derive the RC term, consider the ratio (η) of rotating to nonrotating eddy-viscosity, i.e.,

$$\eta = \frac{C_\mu^{rot}}{C_\mu^{nonrot}} \tag{4.17}$$

where C_μ is a rotation-sensitive eddy-viscosity coefficient derived by York et al. [48] for rotating (C_μ^{rot}) and nonrotating systems (C_μ^{nonrot}). A functional relationship between η and rotation rate (ω^*) was derived by Dhakal and Walters [51], and the same is incorporated in the present model as well. The relationship takes the form of a fifth order polynomial:

$$\eta\,(x) = a_5 x^5 - a_4 x^4 + a_3 x^3 - a_2 x^2 + a_1 x + a_0 \tag{4.18}$$

where $x = \omega^*/S$. However, for two- and three-dimensional flows, x is redefined to ensure frame invariance of the eddy-viscosity coefficient as adopted in York et al. [48]:

$$x = \frac{2}{9}\left(1 - \frac{W}{S}\right) \tag{4.19}$$

The polynomial coefficients a_0 to a_5 are derived in Ref. [51] and are given in Table 4.1. In Eq. (4.19), the strain rate magnitude (S) is defined as

$$S = \sqrt{2S_{ij}S_{ij}} \tag{4.20}$$

where

$$S_{ij} = \frac{1}{2}\left(\frac{\partial U_i}{\partial x_j} + \frac{\partial U_j}{\partial x_i}\right) \tag{4.21}$$

The effective rotation rate magnitude (W) is defined as

$$W = \sqrt{2W_{ij}W_{ij}} \tag{4.22}$$

and the RC effects enter the eddy-viscosity expression via the W_{ij} term which is defined as

$$W_{ij} = \Omega'_{ij} + e_{mji}\omega_m + \frac{-2}{C_4 - 2}e_{mji}\omega_m \tag{4.23}$$

In the above equation, Ω'_{ij} represents the rotation rate tensor in a reference frame rotating with angular velocity ω_m, and C_4 is 0.4. The term ω_m is assumed to be the local Lagrangian rotation rate of the principal axes of the mean strain rate tensor and is computed from the mean velocity field:

$$\omega_i = A_{ij}^{-1} S_{pl}\dot{S}_{lq}e_{pqj} \tag{4.24}$$

where $\dot{S}_{ij}$ is the material derivative of the mean strain rate tensor, and

$$A_{ij}^{-1} = \frac{II_S^2\delta_{ij} + 12III_S S_{ij} + 6II_S S_{ik}S_{kj}}{2II_S^3 - 12III_S^2} \tag{4.25}$$

In the above equation, II_S and III_S are the second and third invariants of the mean strain rate tensor.

Table 4.1 Polynomial coefficients

a_0	a_1	a_2	a_3	a_4	a_5
1.0	18.57	112.0	331.5	437.8	145.7

In viscous dominated near-wall regions, the wall-normal fluctuations are expected to be damped out faster than wall parallel fluctuations, hence the transverse turbulent velocity scale (v^2) is limited to be less than or equal to the TKE using a near-wall limitation on the polynomial term (η_{eff}), and is defined as

$$\eta_{eff} = F_W \min(1, \eta) + (1 - F_W)\eta \tag{4.26}$$

The blending function (F_W) that becomes unity very close to the wall and zero far from the wall is modified as

$$F_W = tanh\left[\left(\frac{200\nu}{\omega^{eff} y^2}\right)^4\right] \tag{4.27}$$

where

$$\omega^{eff} = \frac{\left(\omega + \frac{(D_T + D_L)}{(k_T + k_L)}\right)}{0.09} \tag{4.28}$$

The blending function enforces the value of v^2 to be no greater than the value of k_T in regions very close to the wall.

Note that the blending function (F_W) defined in Eq. (4.27) is different from the wall damping function (f_W) used in Eq. (4.13). Also, in the present model, ψ in the RC term (Eq. (4.8)) is defined as $\psi = C_R\omega$, where $C_R = 1.8$. In ANSYS FLUENT, the scalar transport functions of the proposed model (e.g., k_T, k_L, ω, v^2, etc.) were defined as user-defined scalars, all other model variables (e.g., P_{k_T}, P_{k_L}, η_{eff}, F_W, etc.) were defined as

user-defined memory variables, and user-defined source terms, supplied through UDF subroutines written by the author, were specified for the solution of the transport equations (Eqs. (4.5) – (4.8)).

4.2.4 Boundary Conditions

At the inlet boundary, the value for k_T is set as for any form of a two-equation model and is calculated from the freestream turbulence intensity, defined by:

$$Tu_\infty = \frac{\sqrt{\frac{2}{3}k_T}}{U_\infty} \tag{4.29}$$

If the inlet boundary is considered completely outside the wall boundary layer, the inlet value for k_L is zero, since the LKE associated with pretransitional fluctuations is zero. The inlet value for ω is chosen to coincide with the available freestream conditions, such that an appropriate turbulence decay rate and/or turbulent viscosity ratio is prescribed. The inlet value for v^2 is set equal to the value for k_T based on the assumption that flow at the inlet boundaries is not influenced by any RC effects.

At solid walls, the boundary conditions for the turbulence variables are $k_T = k_L = v^2 = 0$, and a zero-flux condition is enforced for ω

$$\frac{\partial \omega}{\partial \eta} = 0 \tag{4.30}$$

where η is the local wall-normal coordinate direction. Unlike other two-equation models, the boundary condition for ω is defined similar to an approach adopted by many low Re k-ε models, in which a viscous wall destruction term that accounts for the increased levels of dissipation in the viscous sublayer is incorporated into the three transport equations k_T, k_L, and v^2. As $d \rightarrow 0$, the viscous destruction terms ωk_T and $v^2\omega \rightarrow 0$ with $O(\eta^2)$. Hence, in near-wall regions, viscous dissipation in the transport equations is dominated by the

wall destruction term. This approach was followed in the parent k-k_L-ω model and in the proposed model as well.

4.3 Dynamic Hybrid RANS-LES Modeling Methodology

The practical issues present in many current hybrid models, as outlined in Secs. 1.3 and 2.5, are assumed to be fundamental, and a new formulation which resolves the zonal transition weakness and excludes functions dependent on the local grid spacing is required with the additional capability of capturing the flow transition and curvature effects accurately. This motivates the development for a new hybrid modeling framework under the non-zonal category called DHRL. The new hybrid model proposed herein dynamically determines the RANS and LES regions in the computational domain and dynamically adjusts the interface between the two regions based solely on the continuity of total turbulence production governed by the two stress parameters – modeled subgrid stress and modeled Reynolds stress. This ensures a smooth and continuous turbulence production across the interface. The proposed hybrid model utilizes a single grid that spans from RANS to LES regions and generates turbulent fluctuations in the LES region naturally by the instabilities present in the flow. No interface conditions such as synthetic turbulence or controlled forcing [61] are required to generate turbulent structures in the LES region. Furthermore, the DHRL framework is highly generalized, allowing coupling of any desired combination of LES model with any given RANS model. In the present research effort, the DHRL model comprises of the proposed four-equation model (k-k_L-ω-v^2) for the RANS component and the MILES scheme for the LES component. Key features of the DHRL model with T-RC effects are summarized below:

- No explicit grid dependence terms are used in the hybrid formulation.

- RANS-to-LES zonal transition is based on the continuity of total turbulence production.
- The model is capable of resolving both flow transition from laminar-to-turbulent and rotation and/or streamline curvature effects. These effects enter the hybrid model via the RANS component which utilizes the proposed four-equation model.
- The filtering operation in the DHRL formulation is simulation specific, i.e., dictated by the simulation.
- In steady flows, i.e., no resolved fluctuations, the DHRL model produces baseline RANS results.

4.3.1 Formulation

To derive the formulation of DHRL model, firstly consider the resolved momentum equation for incompressible, Newtonian flow with no body forces:

$$\frac{\partial \hat{u}_i}{\partial t} + \hat{u}_j \frac{\partial \hat{u}_i}{\partial x_j} = -\frac{1}{\rho}\frac{\partial \hat{P}}{\partial x_i} + \frac{\partial}{\partial x_j}\left(2\nu \hat{S}_{ij}\right) - \frac{\partial}{\partial x_j}\left(\tau_{ij}\right) \tag{4.31}$$

Both Eqs. (4.2) and (4.31) are similar and represent the conservation of momentum, however, difference lies in the filtering operation used. Reynolds-averaged variables are used in Eq. (4.2) and an undefined filtering (^), i.e., a filtering operation that is dictated by the simulation is used in Eq. (4.31). The last term on the right-hand side represents the turbulent/subfilter stress which needs to be modeled for closure of the resolved momentum equation. In a hybrid RANS-LES approach, the subfilter stress transitions between a modeled Reynolds stress in near-wall regions of the flowfield and a modeled SGS in regions far away from the wall. The subfilter stress is defined as

$$\tau_{ij} = \widehat{u_i u_j} - \hat{u}_i \hat{u}_j \tag{4.32}$$

In the DHRL methodology, we represent the large-scale motions of turbulent flow by a 3D unsteady velocity field called the resolved velocity ($\hat{u}_i$), a fundamental quantity in LES. The resolved velocity field consists of both Reynolds-averaged (mean) velocity

($\overline{u}$) and resolved fluctuating (u'') components. The remaining turbulent motions, called the unresolved fluctuating field is denoted by u_i'. Using this representation, the instantaneous velocity field (u_i) is decomposed into three components:

$$u_i = \overline{u_i} + u_i'' + u_i' \tag{4.33}$$

This decomposition considers both the effects of ensemble-averaged and spatially-averaged velocity fields. Equation (4.33) can be written in terms of the resolved velocity field as

$$u_i = \hat{u}_i + u_i' \tag{4.34}$$

where $\hat{u}_i = \overline{u_i} + u_i''$. The resolved velocity field is directly computed from the simulation and the unresolved fluctuating field is modeled via the subfilter stress term. Substituting velocity decomposition (Eq. (4.34)) into the subfilter stress definition (Eq. (4.32)) yields:

$$\tau_{ij} = \widehat{\hat{u}_i\hat{u}_j} + \widehat{\hat{u}_i u_j'} + \widehat{u_i'\hat{u}_j} + \widehat{u_i' u_j'} - \hat{u}_i\hat{u}_j \tag{4.35}$$

Assuming negligible correlation between resolved and unresolved velocity fluctuations results in an expression for the subfilter stress as

$$\tau_{ij} = \widehat{\hat{u}_i\hat{u}_j} + \widehat{u_i' u_j'} - \hat{u}_i\hat{u}_j \tag{4.36}$$

The first and third terms together (right-hand side of Eq. (4.36)) are modeled as a linear function of the SGS that would be obtained using an LES model, and the second term is modeled as a linear function of the Reynolds stress that would be obtained using a RANS model. Following the concept of scale-similarity, the components of Eq. (4.36) can be written as

$$\widehat{\hat{u}_i\hat{u}_j} - \hat{u}_i\hat{u}_j = \alpha\left(\widehat{u_i u_j} - \hat{u}_i\hat{u}_j\right) \tag{4.37}$$

$$\widehat{u_i' u_j'} = \beta \overline{u_i' u_j'} \tag{4.38}$$

and Eq. (4.36) can be expressed as

$$\tau_{ij} = \alpha \left(\widehat{u_i u_j} - \hat{u}_i \hat{u}_j \right) + \beta \overline{u_i' u_j'} \tag{4.39}$$

The spatially varying proportionality constants, α and β, are assumed to be complementary throughout the domain, hence the subfilter stress is expressed as a weighted average of the modeled SGS (τ_{ij}^{SGS}) and modeled Reynolds stress (τ_{ij}^{RANS}):

$$\tau_{ij} = \alpha \tau_{ij}^{SGS} + (1 - \alpha)\, \tau_{ij}^{RANS} \tag{4.40}$$

To obtain an expression for the unknown model coefficient α, the velocity decomposition defined in Eq. (4.34) and a secondary filter are applied on the subfilter stress (Eq. (4.40)):

$$\tau_{ij}^{RANS} - \overline{\tau_{ij}} = \left(\overline{u_i u_j} - \overline{u_i} \overline{u_j} \right) - \left(\overline{\widehat{u_i u_j}} - \overline{\hat{u}_i \hat{u}_j} \right) = \overline{\hat{u}_i \hat{u}_j} - \overline{u_i} \overline{u_j} = \overline{u_i'' u_j''} \tag{4.41}$$

The secondary filter, represented by the Reynolds-averaging operation, is based on the concept of dynamic LES model coefficient evaluation [89]. Also, to obtain Eq. (4.41), the resolved and modeled velocity components are once again assumed to be uncorrelated. Combining Eqs. (4.40) and (4.41), and taking the scalar product of the result with the mean strain rate tensor ($\overline{S_{ij}}$) yields:

$$\alpha = \frac{\overline{u_i'' u_j''}\, \overline{S_{ij}}}{\left(\tau_{ij}^{RANS} \overline{S_{ij}} - \overline{\tau_{ij}^{SGS}}\, \overline{S_{ij}} \right)} \tag{4.42}$$

Based on the production of TKE due to resolved turbulent scales ($\overline{u_i'' u_j''}\, \overline{S_{ij}}$), modeled Reynolds stress ($\tau_{ij}^{RANS} \overline{S_{ij}}$), and mean component of the modeled SGS ($\overline{\tau_{ij}^{SGS}}\, \overline{S_{ij}}$), the value of α varies from 0 to 1. In regions of the flowfield with high resolved production, the effect of the modeled Reynolds stress on the momentum equation is reduced and the

model behaves in pure LES mode, with the value of α limited to 1. On the contrary, in regions of the flowfield with no resolved fluctuations (especially in near-wall regions), α is 0 and the model behaves in pure RANS mode. The key to the success of any hybrid approach depends on the behavior of the model in regions of the flowfield with significant presence of both resolved and modeled RANS production (i.e., resolved scale production less than RANS production). In these regions, the DHRL model behaves in a transitional mode wherein an additional RANS stress compensates for the reduced LES content, thereby leading to a smooth variation of turbulent production across the region. Another key aspect of the DHRL framework is that any desired combination of RANS model can be used with any given LES model to compute τ_{ij}^{RANS} and τ_{ij}^{SGS}, respectively.

4.3.2 Implementation

In the present research effort, the proposed four-equation model (RANS component) is combined with the MILES scheme (LES component) to develop a hybrid model for complex turbulent flows with a potential to obtain improved accuracy in predictions compared to RANS models, and at a significant reduction of computational cost compared to LES models. Since the MILES scheme is used for the LES component, the explicitly modeled SGS term (second term in the denominator of Eq. (4.42)) is zero. To impose the MILES methodology, the momentum equations were modified by specifying the eddy-viscosity to be effectively zero, with an additional source term added to include the integrated effect from the contribution of the RANS stress term. Another important aspect of the new model includes the computation of the RANS model terms

based solely on the mean velocity field. For other details regarding model implementation, interested readers can refer to Walters et al. [90].

CHAPTER V

VALIDATION OF THE FOUR-EQUATION RANS MODEL

Any new turbulence model, such as the four-equation EVM and DHRL, must be subject to a wide range of tests ranging from simple to complex validation cases before commenting on the accuracy and the potential of the models. In this chapter, the proposed four-equation model is validated against several 2D test cases involving flow transition and RC effects. In chapter VI, the four-equation model is tested on a complex 3D case comprising of an axisymmetric hill, and in chapter VII, the DHRL model which employs the four-equation model along with the MILES scheme is validated against several benchmark problems. Results obtained from the numerical simulations of each test case are presented in detail. The complete list of validation cases on which the proposed models were tested against is given in Table 3.1 (See Sec. 3.2).

5.1 Numerical Method

CFD simulations of all the test cases were performed using the pressure-based solver in ANSYS FLUENT. For all the RANS model simulations, the SIMPLE scheme [91] was used for pressure-velocity coupling, the PRESTO! scheme was used for discretization of pressure terms, and gradients were computed using a Green-Gauss cell based method [92]. A second-order upwind-based discretization scheme was used for the convective terms of all equations and unsteady terms for transient simulations were discretized using a second-order implicit (three-point backward difference) scheme.

Upwind schemes are generally preferred for spatial discretization in order to obtain accurate results and numerical stability at high Re for incompressible flows [93].

For a steady-state computation, the problem is said to obtain a state of convergence when the solution does not change with additional iterations, while in an unsteady computation, it must be ensured that the solution at each time step is fully converged and time-averaged flow parameters do not change with additional time steps. Simulations with the k-k_L-ω-v^2 model adopted either a steady or unsteady RANS approach as dictated by the test case. For all unsteady simulations, a fixed time stepping method was used with the time step size for each case set to correspond to a convective CFL number of 1, based on the freestream velocity and the minimum streamwise cell size in the domain. Additional simulations were performed with CFL numbers of 0.5 and 2 to ensure time step size independence of the simulations. Based upon the time step study, a time step-size of 0.01 T (for 2D rotating channel flow and ZPG boundary layer flow over a flat plate), a time step-size of 0.001 T (for 2D flow over a circular cylinder and flow over an elliptic airfoil), with a maximum of 20 iterations per time step, were found to be sufficient and were used for the respective results shown here. Here, T is the flow-over time, equal to the chord length divided by the freestream velocity ($T = c/U_\infty$). All test cases were run to full convergence, based on reduction of residuals at each time step of at least three orders of magnitude as well as numerically steady-state condition of monitored simulation variables for steady-state cases. For unsteady cases, running time-averages of all dependent variables were monitored and simulations were continued until the time-averaged values became stationary. To achieve this, a maximum of 20 outer iterations per

time step were found to be sufficient. Unless stated otherwise, all the results presented below are time-averaged quantities.

A grid sensitivity study was performed for all of the test cases by systematically refining the grid until the solution remained effectively unchanged between the coarser grids and their refined versions. Each refinement level represented an increase in cell count of approximately 60% or higher versus the next coarsest grid level. Based upon the above procedure, the results presented here were judged to be grid-independent for all cases. More details regarding grid independence study for each test case are given in the following sections.

For purposes of evaluating computational cost of the proposed RANS model, additional simulations were performed on the elliptic airfoil test case using the four-equation model and the transition-sensitive k-k_L-ω model under identical conditions. It was observed that approximately 12000 and 8000 time steps were required for the proposed model and the k-k_L-ω model, respectively, to obtain convergence of the time-averaged quantities of flow variables. Also, the proposed RANS model requires about 18% more computation time per iteration than its predecessor (k-k_L-ω), which is expected given the fact that an additional transport equation (v^2) is solved every iteration.

5.2 Test Case 1: Two-Dimensional Channel Flow

To assess the ability of the proposed four-equation model to capture system rotation effects accurately, a simple 2D rotating channel flow was first considered. This classic test case has been the subject of numerous experimental and computational studies [50,94], and a schematic of the problem is shown in Fig. 5.1. Numerical simulations were performed on a fully developed channel flow with Reynolds number (Re_τ) equal to 194,

based on the wall friction velocity and channel half-height ($H/2$), and rotation numbers (Ro) equal to 0.0 (nonrotating case) and 0.5 (rotating case). The rotation number is defined as $Ro = \omega_m H/U_m$, where ω_m is the angular velocity of the reference frame relative to inertial frame and U_m is the average velocity through the channel. The new model results were compared with the DNS data of Kristoffersen and Andersson [95] for validation purposes. As discussed in Sec. 2.2, ASMs provide the capability to model curvature effects directly as well as the effect of Reynolds stress tensor anisotropy. Due to the unavailability of ASMs in FLUENT solver, and the additional complexity involved in implementing the models using user-defined functions (UDFs), the results obtained from the new model were compared in this study only with the UDF implemented curvature-sensitive SST k-ω-v^2 model and the fully turbulent model SST k-ω available in ANSYS FLUENT. The pressure-driven channel flow was modeled using a 2D domain with a Cartesian grid size of 20 × 200 (streamwise × wall normal) and with periodic boundary conditions applied in the streamwise direction. The generated grid has y^+ values less than unity at the walls and results were determined to be grid independent based on the procedure outlined above. The baseline mesh for the nonrotating and rotating channel flow cases is shown in Fig 5.2.

Fig. 5.3 shows the velocity profiles normalized by the average channel velocity for the nonrotating channel flow test case. The new model predicts a symmetric velocity profile and is in close agreement with the DNS data. Figures 5.4–5.6 show the velocity, TKE, and turbulent shear stress profiles, respectively, for the rotating channel case. Here, the TKE and turbulent shear stress are normalized by the square of the average wall friction velocity. The characteristic asymmetry caused by the imposed rotation (Ro = 0.5)

in the velocity profiles is correctly predicted by the new model and also by the curvature-sensitive SST k-ω-v^2 model. As expected, the SST k-ω model predicts a symmetric velocity profile for the rotating case, since the model has no sensitivity to flow rotation effects.

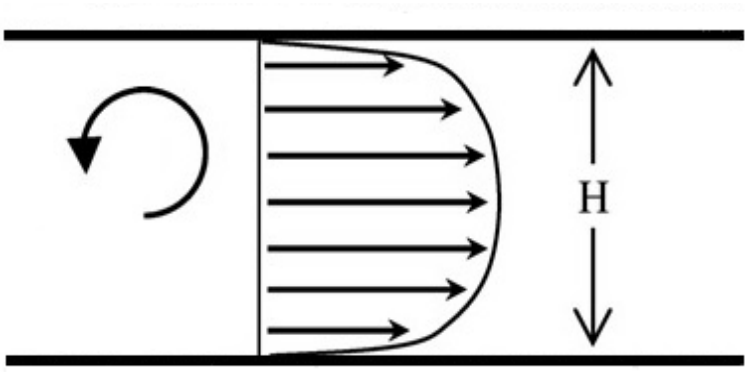

Figure 5.1 Schematic representation of fully developed rotating turbulent channel flow test case

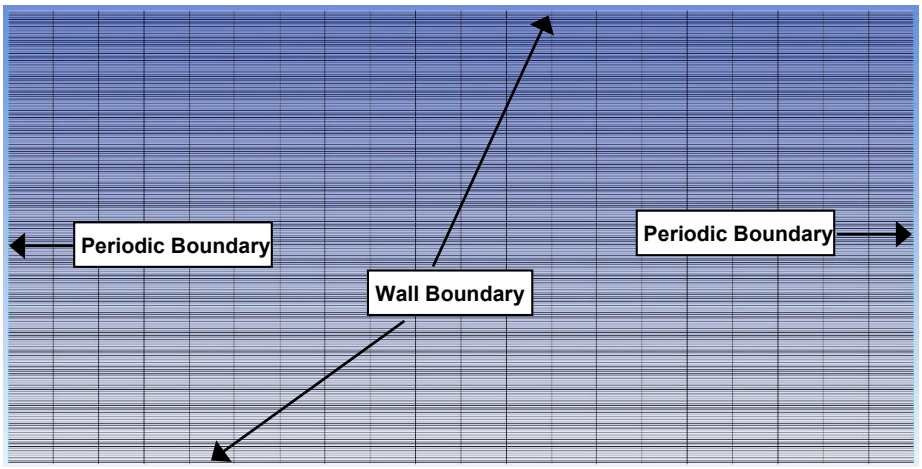

Figure 5.2 Baseline mesh for channel flow test case showing grid density and boundary conditions

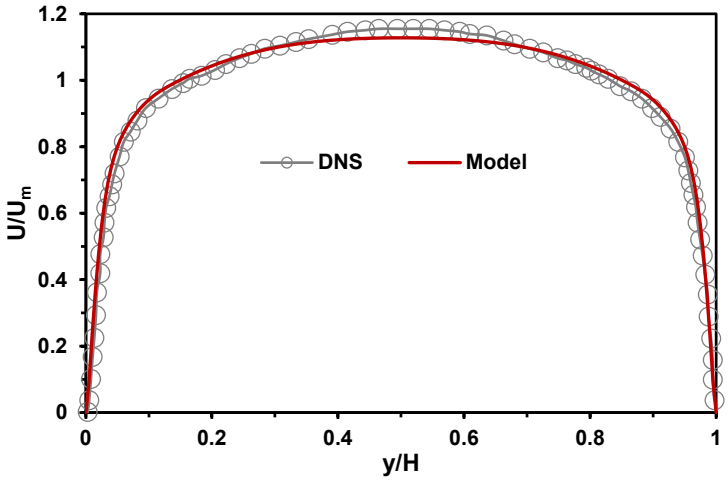

Figure 5.3 Mean velocity profiles for nonrotating (*Ro* = 0.0) channel flow case comparing new model with DNS data

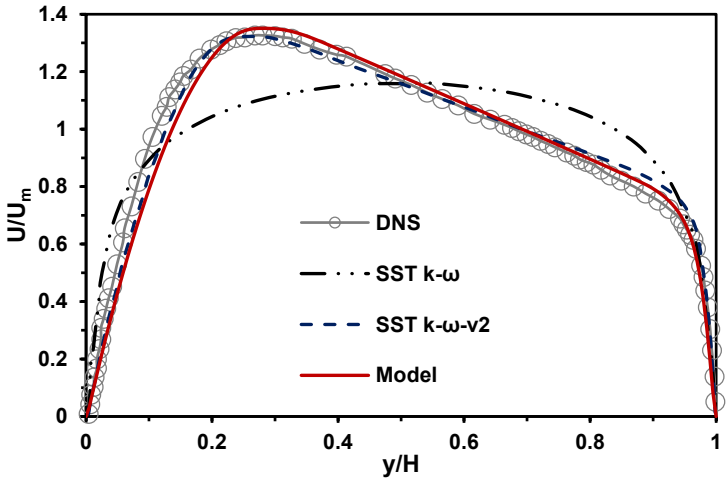

Figure 5.4 Mean velocity profiles for rotating (*Ro* = 0.5) channel flow case

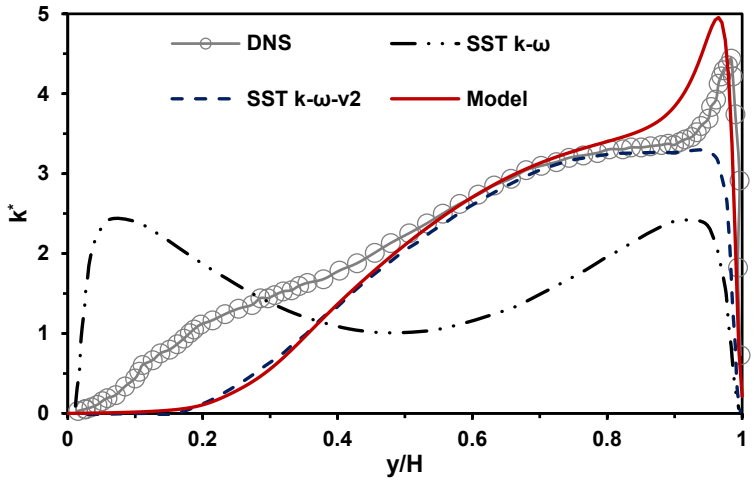

Figure 5.5 TKE profiles for rotating (*Ro* = 0.5) channel flow case

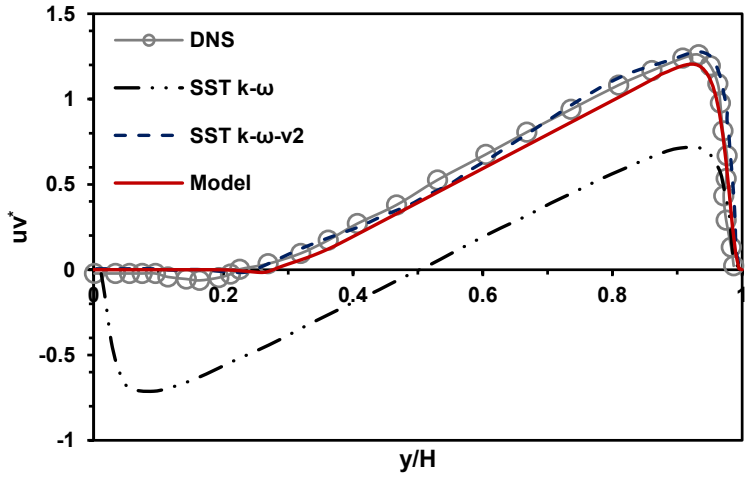

Figure 5.6 Turbulent shear stress profiles for rotating (*Ro* = 0.5) channel flow case

From Fig. 5.5, it is observed that the TKE profiles produced by the new model and the SST k-ω-v^2 model are similar, however, the peak region near the pressure side of the channel is better predicted by the new model and is qualitatively in closer agreement with the DNS data. Turbulent shear stress profiles predicted by the new model and the

SST k-ω-v^2 model (Fig. 5.6) are similar and in good agreement with the DNS profile. Again, the SST k-ω model, being insensitive to rotation, fails to accurately predict the TKE and turbulent shear stress profiles for the Ro = 0.5 case. The rotating channel flow results presented here indicate that the new model yields an appropriate response to flow rotation effects and produces results in close agreement with the DNS data. More importantly, the model yields results in close agreement with the curvature-sensitive SST k-ω-v^2 model for fully turbulent flows, as expected.

5.3 Test Case 2: Two-Dimensional ZPG Flow over a Flat Plate

Flow over a 2D flat plate without streamwise pressure gradients or curvature effects is the simplest test case to verify the transition behavior of the proposed four-equation model. The chosen flat plate cases match the European Research Consortium on Flow, Turbulence and Combustion (ERCOFTAC) T3A-, T3A, and T3B test cases [96], which are widely used for the verification and validation of transition-sensitive CFD models. In the simulations performed on the flat plate, the transition behavior predicted by the model in response to freestream turbulence intensity (Tu_∞) was assessed. The skin friction coefficients (C_f) and boundary layer profiles of velocity, total fluctuation energy (k_{TOT}), LKE, and TKE predicted by the model were compared with available experimental data.

The computational domain and mesh constructed for the flat plate test case with a semi-circular leading edge (LE) is shown in Fig. 5.7. The domain extended 0.05 m upstream and 2 m downstream of the plate LE, where velocity inlet and pressure outlet boundary conditions were specified, respectively. To ensure negligible acceleration of the freestream velocity due to finite plate thickness and boundary layer development, the top

boundary, specified as a symmetry plane, was located far from the wall (1.26 m) in the wall normal direction. The results confirmed a freestream acceleration of less than 5% over the entire length of the plate for all three test cases. In order to allow a natural stagnation of the freestream flow and boundary layer start, a symmetry condition was applied at the bottom of the domain, upstream of the LE. The simulations used a 2D structured grid with a total of 49,156 cells, and the same grid was used for all the three test cases. The mesh was generated with grid points clustered near the wall and near the plate LE regions. The y^+ values for the first grid point away from the wall were maintained less than one over the entire plate, and grid independence was verified using the procedure outlined above.

The dimensionless LE freestream conditions for each of the three flat plate cases are listed in Table 5.1. The inlet values of k_T and ω for each case were chosen so that the streamwise decay of freestream turbulence closely matched the results reported in the experiments. Figure 5.8 shows the representative agreement between the freestream turbulence values predicted by the model and experiments. The inlet values for v^2 were set identical to the values of k_T and the inlet value of k_L was set to zero. The computational domain, grid, boundary conditions, and numerical method used for this test case were similar to those reported in Walters and Cokljat [34].

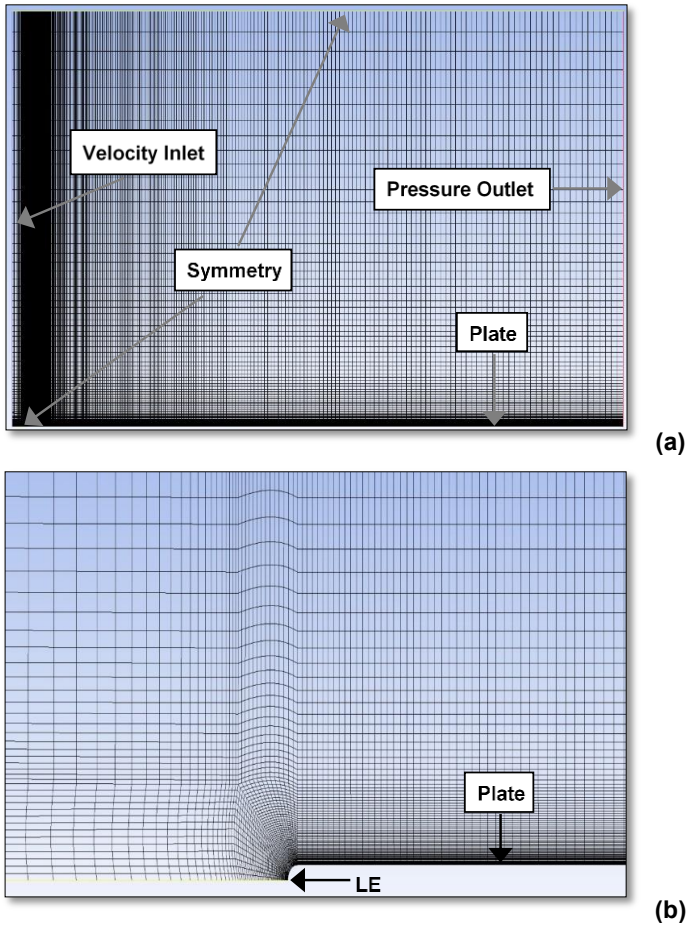

Figure 5.7 (a) Computational domain and boundary conditions used for ZPG flat plate test case, and (b) close-up of grid near flat plate LE

Table 5.1 LE freestream conditions for T3 ZPG flat plate test cases

Test Case	Tu (%)	μ_T/μ
T3A-	0.874	8.73
T3A	3.3	12.0
T3B	6.5	100.0

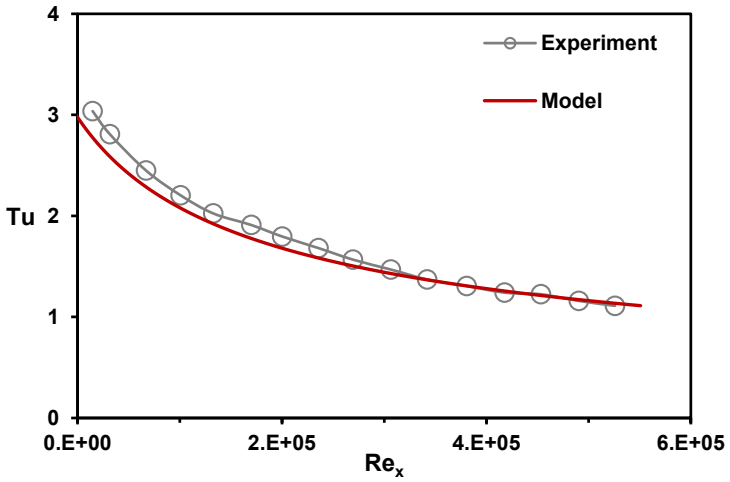

Figure 5.8 Streamwise decay of freestream turbulence intensity for test case T3A, compared to experimental data

The predicted mean skin friction coefficient versus Re for each of the three test cases, along with the results obtained from the simulations of fully laminar and fully turbulent cases, are shown in Fig. 5.9. The plots indicate that the model predicted values in good agreement with experimental data for all three values of Tu_∞, although transition occurs slightly too quickly in test case T3A. The ability of the new model to resolve transition effects accurately can be highlighted by making a comparison with the results of fully turbulent cases, which are also shown in the plots for reference purposes. Unlike the transition-sensitive model presented here, the conventional linear EVM, which would closely match the fully turbulent case, predicts a turbulent boundary layer from the start of the plate LE and fails to capture any laminar-to-turbulent flow transition effects. This is the expected behavior from traditional EVMs, as they do not possess the ability to resolve the flow transition effects accurately.

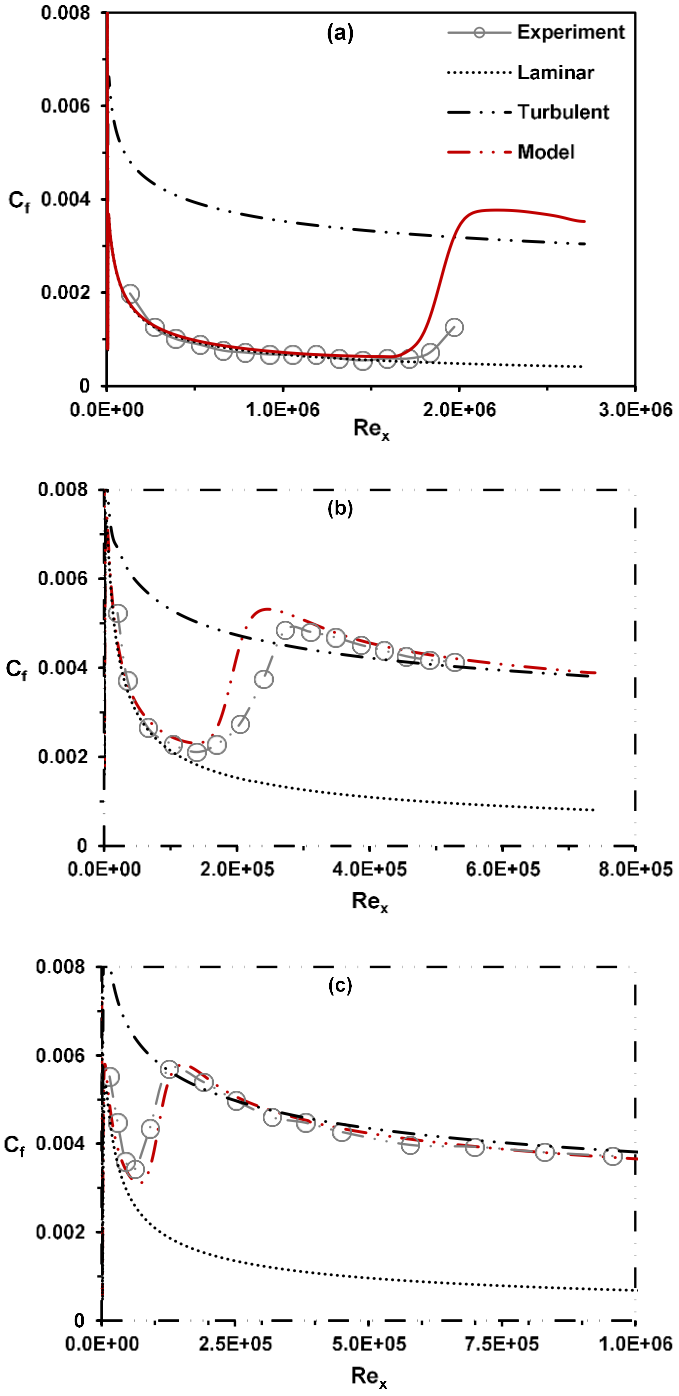

Figure 5.9 Streamwise distribution of skin friction coefficient (C_f) for each of the three flat plate cases: (a) T3A-, (b) T3A, and (c) T3B

The new model indicates the flow transition behavior over the flat plate clearly, and more importantly, it accurately responds to the changes in freestream turbulence intensity. As Tu_∞ is increased, the flow transition point moves upstream on the plate. From the examination of the results, it is observed that, for test case T3A-, transition is predicted to begin at $Re_x \approx 1{,}600{,}000$ and end at $Re_x \approx 2{,}200{,}000$. For test case T3A, transition is predicted to begin at $Re_x \approx 160{,}000$ and end at $Re_x \approx 280{,}000$, and for T3B, transition begins at $Re_x \approx 70{,}000$ and ends at $Re_x \approx 160{,}000$. The transition start and end locations were obtained from the local minimum and maximum of shear stress in the mean C_f distribution.

The predicted boundary layer profiles of mean velocity, total fluctuation energy, LKE, and TKE in comparison with the experimental data are shown in Fig. 5.10. The profiles were computed for the T3A test case in the pretransitional, transitional, and turbulent regions of fluid flow over the flat plate at locations corresponding to $Re_x = 1 \times 10^5$, 2×10^5, and 4×10^5 respectively. Agreement between the experimental data and computational results for the boundary layer profiles of mean velocity and k_{TOT} are quite good. The shape factors for the mean velocity profile reported in the experiments for pretransitional, transitional, and turbulent regions are 2.39, 1.90, and 1.47, respectively, and the corresponding values predicted with the new model are 2.43, 1.88, and 1.44. At $Re_x = 1 \times 10^5$, the plots confirm that the pretransitional boundary layer mean velocity profile is laminar. The peak level of k_L increases up to the transition region, wherein a transfer of energy takes place from k_L to k_T, and a corresponding change in the profiles is observed. At $Re_x = 4 \times 10^5$, the velocity profiles indicate a turbulent boundary layer.

Moreover, the magnitude of k_L reduces to a minimum value as the boundary layer develops further downstream of the flow transition point.

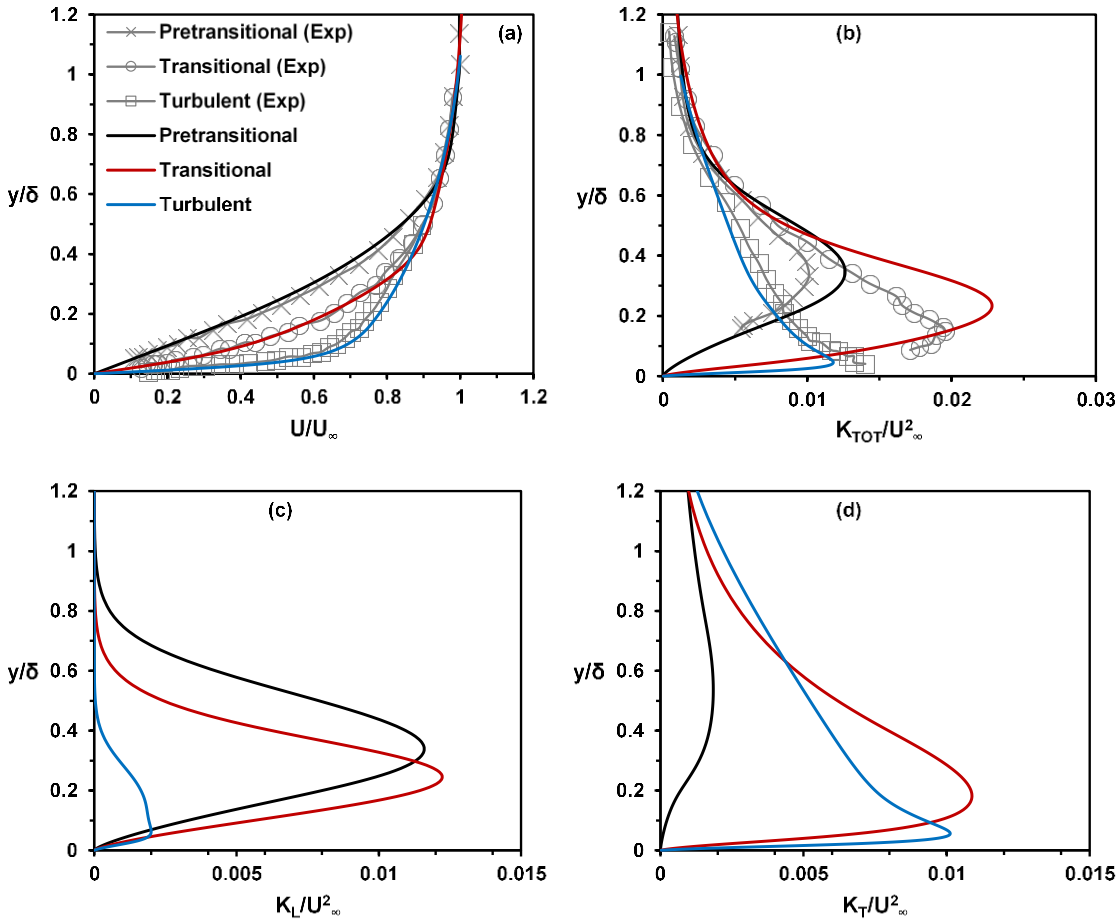

Figure 5.10 Normalized profiles of (a) mean velocity (U), (b) total fluctuation kinetic energy (k_{TOT}), (c) LKE (k_L), and (d) TKE (k_T) in pretransitional, transitional, and turbulent regions of boundary layer in test case T3A

Overall, the flat plate test case results presented here indicate that the new model performs well with regard to the laminar-to-turbulent flow transition prediction. This result is significant since it demonstrates that, in the absence of any RC effects, the

addition of the v^2 transport equation has no significant impact on the model results compared to the original k-k_L-ω model.

5.4 Test Case 3: Two-Dimensional Flow over a Circular Cylinder

A simple test case to demonstrate the ability of the new model to address both T-RC effects simultaneously is flow over a circular cylinder. Depending on the range of Re, flow over a blunt body like that of a cylinder can exhibit highly complex and varying behavior, which is often challenging for RANS-based CFD prediction. As described by Schlichting and Klaus [39], subcritical flow over a circular cylinder is in the range of $300 \lesssim Re_D \lesssim 1.3 \times 10^5$. Here, the boundary layer is laminar and flow separation takes place upstream of 90 deg, which is then followed by transition to turbulence in the wake region. At critical Reynolds numbers ($1.3 \times 10^5 \lesssim Re_D \lesssim 3.5 \times 10^6$), the laminar boundary layer separates, transitions to turbulence, and reattaches to the cylinder surface, leading to the formation of a small separation bubble, and separates again farther downstream producing a turbulent wake region. Finally, at supercritical Re ($Re_D \gtrsim 3.5 \times 10^6$), attached boundary layer transition from laminar to turbulent is observed upstream of 90 deg, which is then followed by the turbulent boundary layer separation at about 120 deg. Additional discussion on experimental and computational studies of low to high Re flows over a circular cylinder can be found in Refs. [97-99].

For model validation purposes, a series of 2D unsteady simulations were performed on a cylinder in the range of $10^4 \leq Re_D \leq 10^7$. This range of Re was specifically chosen for the test cases, since curvature and transition effects play a nontrivial role in determining the flow behavior over the cylinder. Additionally, contrast between the predictions of fully turbulent, transition-sensitive, curvature-sensitive, and

the new model could be highlighted. Specifically, it is expected that both T-RC effects will be more pronounced at lower Re. Results presented below compare the performance of a fully turbulent conventional EVM (SST k-ω), a transition-sensitive model (k-k_L-ω), and a curvature-sensitive model (SST k-ω-v^2) to the new model and available experimental results.

The 2D circular cylinder had a unit diameter and Reynolds number based on the cylinder diameter (Re_D) was varied from 10^4 to 10^7. To ensure that the boundary locations did not influence the flow, all farfield boundaries were placed 10 diameters from the cylinder. The upstream and downstream boundaries were specified as velocity inlet and pressure outlet, respectively, and the top and bottom boundaries were specified with a periodic condition. The cylinder surface was defined as a solid wall. The inlet boundary conditions for the test case were defined with an air velocity of 15.345 m/s, turbulence intensity of 0.2%, and a turbulent length scale of 0.1 times the diameter of the cylinder. The Re_D was varied by changing the dynamic viscosity (μ) of the fluid, while holding all other quantities as constant. The boundary conditions and numerical method used for this test case were similar to those reported in Ref. [97]. A high quality, multi-block grid was generated for all the cylinder test cases and mesh sizes for each Re are given in Table 5.2. Structured cells were used for the region next to the cylinder wall with a y^+ value of unity and the rest of the grid was constructed with unstructured cells. The grid transition from structured cells near the wall region to unstructured cells outside the wall boundary layer was defined smoothly in such a way that the centroid of the triangular cell matched the half height of the rectangular cell. The computational domain and mesh used for the simulations of $Re_D = 10^7$ test case is illustrated in Fig. 5.11. All grids were judged to yield

mesh independent results based on the procedure discussed above. Table 5.3 shows an example of such a grid sensitivity study. Here, the mean drag coefficient values obtained from the simulations of the circular cylinder test case for various grid sizes are shown. Figure 5.12 shows the mean pressure coefficient (C_P) profiles obtained from the simulations of the circular cylinder test case using both medium and fine grids plotted for flow at Re_D of 10^4.

Table 5.2 Mesh size for each cylinder test case

Re_D	Mesh Size
10^4	337,256
10^5	365,836
10^6	397,624
10^7	442,484

The profiles of normalized TKE and streamwise velocity at the first grid point from the wall along the top of the cylinder, for the new model in comparison with SST k-ω-v^2, are shown in Figs. 5.13 and 5.15. The actual values in the plots are mesh dependent and therefore not significant in themselves; however, the plots do serve to identify the locations of transition, separation, and reverse flow on the cylinder surface. Transition is indicated by a rapid increase in TKE to non-negligible levels, while separated flow regions are indicated by negative values of the mean streamwise velocity. The plots highlight the predictive capability of the model to accurately capture the flow transition effects, while the SST k-ω-v^2 indicates a fully turbulent boundary layer over the entire cylinder surface.

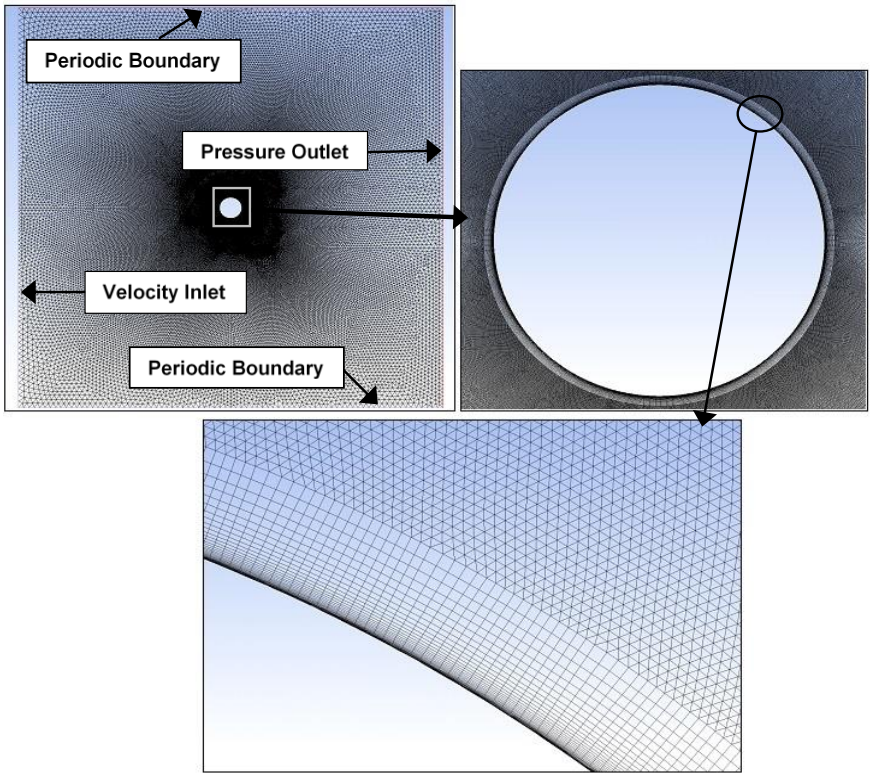

Figure 5.11 Computational grid, boundary conditions, and close-up of mesh near the surface of circular cylinder test case for flow $Re_D = 10^7$

Table 5.3 Comparison of drag coefficient data for circular cylinder test case at $Re_D = 10^4$ versus grid size

Grid size	Drag coefficient (c_d)	% difference
263,048	1.52	-
337,256 (Medium)	1.597	5.07
541,600 (Fine)	1.624	1.69

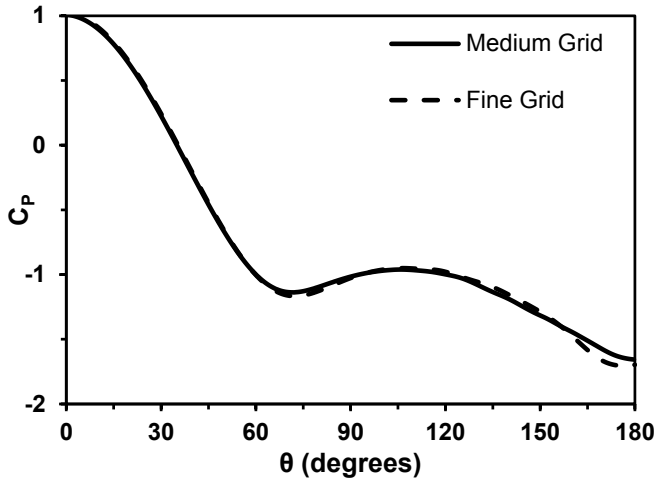

Figure 5.12 Example grid sensitivity study for circular cylinder test case at $Re_D = 10^4$

As discussed previously, at $Re_D = 10^6$, the flow is in the critical regime. Hence, the laminar boundary layer separates from the cylinder surface, transitions to turbulence, reattaches as a turbulent boundary layer, and finally separates downstream of 90 deg. The model predicts a laminar boundary layer separation at 102 deg and turbulent boundary layer separation at 123 deg. In contrast, the SST k-ω-v^2 model predicts a turbulent boundary layer from the LE stagnation point ($\theta = 0$ deg) and predicts flow separation at 112 deg, about 11 deg earlier than the new model predictions. For the supercritical flow, at $Re_D = 10^7$, the new model predicts an attached boundary layer transition upstream of 90 deg and turbulent flow separation at 119 deg. The SST k-ω-v^2 model again predicts a turbulent boundary layer from the stagnation point onward and turbulent flow separation, similar to the results for $Re_D = 10^6$.

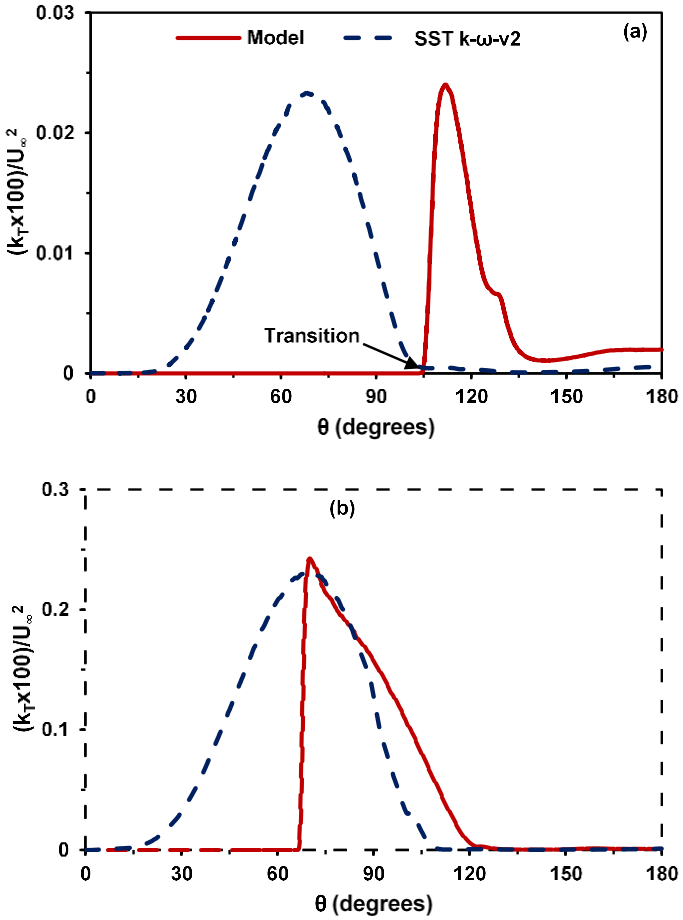

Figure 5.13 Time-averaged TKE along the top of the cylinder for Re_D (a) 10^6 and (b) 10^7

Figure 5.15 shows a plot of the time-averaged coefficient of drag (C_D) versus Re_D for each of the turbulence models used in this study, in comparison with the experimental values [39]. In the subcritical flow regime, C_D values predicted by the model are closer to the experimental data when compared to the predictions of other turbulence models. The differences in the predictions are attributed to the ability of the new model to resolve both curvature and transitional effects on the flowfield. Both the transition-sensitive k-k_L-ω model and the new model captured the drag crisis region accurately and matched closely

with the experimental data. The new model predicts values of C_D greater than one for subcritical flow, which is followed by a sudden drop in values in the critical flow regime and finally, a gradual increase in C_D for supercritical flow.

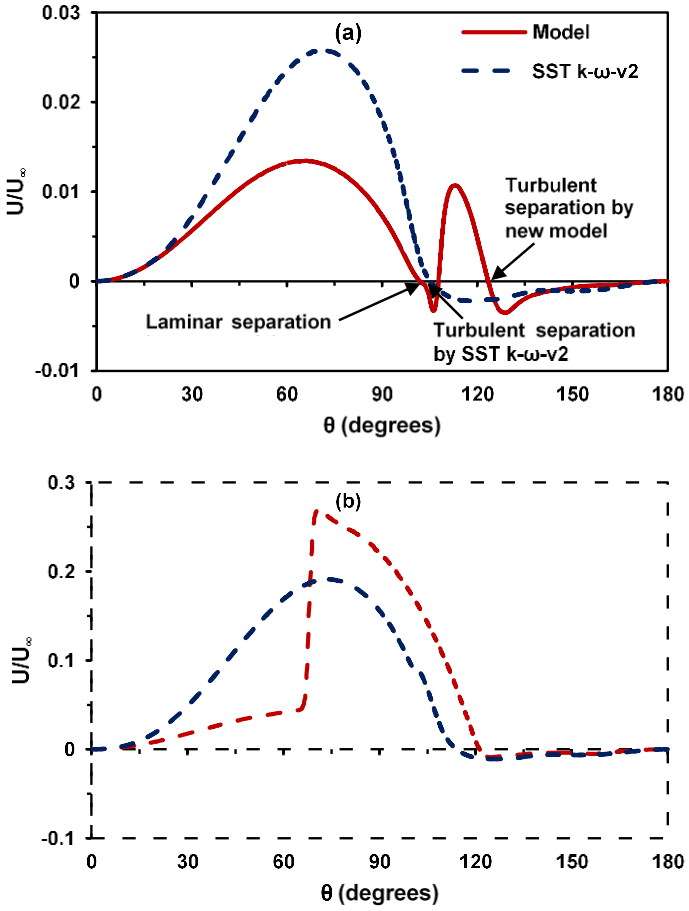

Figure 5.14 Time-averaged streamwise velocity distribution along the top of the cylinder for Re_D (a) 10^6 and (b) 10^7

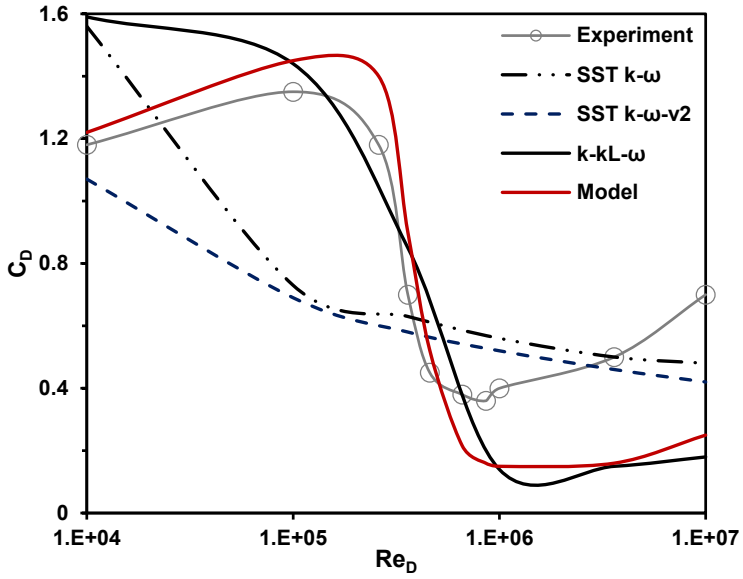

Figure 5.15 Time-averaged drag coefficient curves for all the turbulent models used in this study and in comparison with experimental results

Although the qualitative flow behavior predicted by the new model matches closely with the experiments, the drag coefficient values are slightly over predicted in the drag crisis region and are under predicted in the supercritical flow region. Similar flow predictions are observed from the k-k_L-ω model. This error in the C_D values predicted by the new model is due to the over prediction of flow separation angle in the supercritical flow case. The fully turbulent and curvature-sensitive models fail completely to predict the drag crisis region, since they predict a fully turbulent boundary layer over the entire cylinder surface regardless of Re, and it is observed that the C_D values decrease monotonically as a function of Re_D. Note, however, that the drag coefficient is better predicted in the subcritical region using the new model, which accounts for curvature effects, than using the k-k_L-ω model. For a surface with constant radius of curvature, the effect on the boundary layer development will be less pronounced as the Reynolds

number increases and the boundary layer thickness becomes smaller. For flow at Re_D = 10^4, the ratio of boundary thickness to cylinder radius is relatively high, and curvature effects are expected to play a more significant effect than, for example, the case of Re_D = 10^7. This is apparent in the results, as the new model and the k-k_L-ω model show increasingly similar results as Re increases.

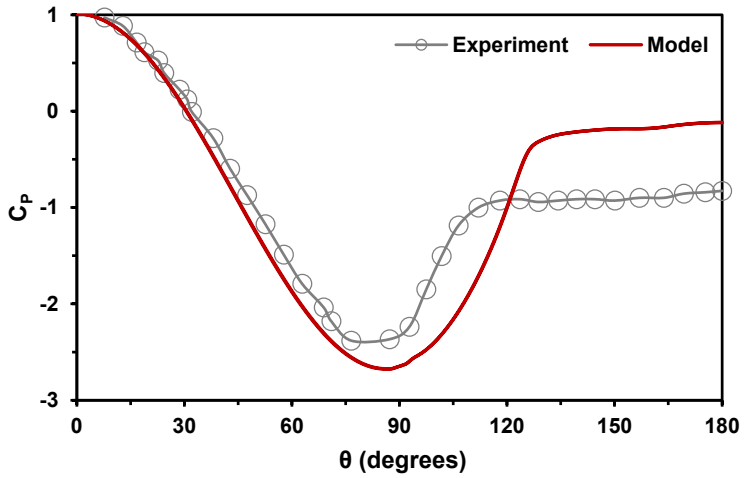

Figure 5.16 Time-averaged pressure coefficient distribution along the top of the cylinder at Re_D = 3.6 x 10^6 in comparison with experiments.

Discrepancy in the C_P profile can be attributed to the delayed prediction of flow separation point by the new model

Figure 5.16 shows the distribution of the mean pressure coefficient (C_P) over the cylinder wall for the supercritical flow case Re_D = 3.6 x 10^6. Here, the experimental data of Achenbach [100] is compared with the predictions of the new model. CFD predictions match well with the experiment profile for the upstream half of cylinder, but discrepancies in the C_P profiles are clearly visible for the downstream half of cylinder. It was reported in the experiments that the flow separated from the cylinder surface at an

angle of 116 deg, whereas the new model predicts flow separation at an angle of 120 deg. The discrepancies observed in the time-averaged pressure coefficient profile and in drag coefficient values can be attributed to the delayed prediction of flow separation point using the new model, which is apparently not significantly influenced by RC effects.

Mean velocity contours for the circular cylinder case obtained using the new model at Re corresponding to 10^4, 10^5, 10^6, and 10^7 are shown in Fig. 5.17. At $Re_D = 10^4$ and 10^5, flow is in the subcritical flow regime. For $Re_D = 10^4$, the new model predicts a laminar boundary layer over the entire surface of cylinder and flow separation takes place upstream of 90 deg. For a flow Reynolds number of 10^5, the model again predicts a laminar boundary layer over the surface of cylinder and flow separation is observed just downstream of 90 deg. Here, the separated flow transitions to turbulence in the wake region close to the cylinder surface. At a critical Re of 10^6, a LSB is observed on the cylinder surface due to the flow transition from laminar to turbulent. While the bubble is not clearly visible in the velocity contours shown, it is predicted by the new model at an angle of 102 deg. The reattached turbulent boundary layer separates at a location farther downstream on the cylinder surface as compared to the flow separation for earlier cases. At a supercritical Re of 10^7, the model predicts an attached boundary layer transition from laminar to turbulent upstream of 90 deg, which is followed by a turbulent flow separation at an angle of 119 deg. The turbulent wake region predicted by the model is clearly observed in the mean velocity contours for $Re_D = 10^6$ and 10^7. On the whole, the new model successfully resolves the flow characteristics observed in all the three distinct flow regimes and its predictions are in relatively good agreement with the experimental results.

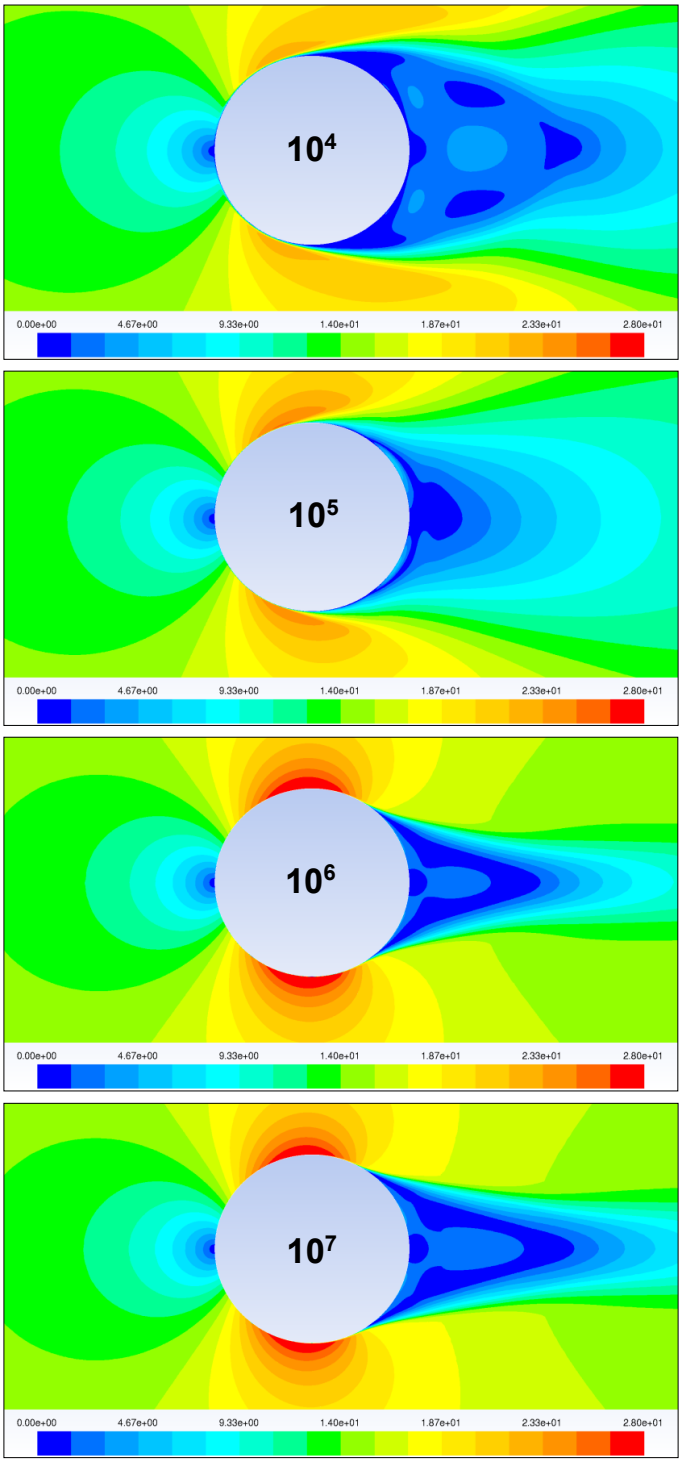

Figure 5.17 Mean velocity contours of circular cylinder for the new model at various Re

5.5 Test Case 4: Flow over an Elliptic Airfoil

As a final 2D test case in this study, low Re flow over an elliptic airfoil is considered. The particular elliptic airfoil used in this study has practical applications in unmanned aerial vehicles (UAVs) [17]. Though the test case looks simple in terms of geometry, the complex physics involved make it a challenging one for turbulence closure models. Elliptic airfoils have blunt leading and trailing edges, which can cause flow separation and reattachment on the surface of airfoil leading to the formation of LSBs and vortex shedding in the flow field aft of the airfoil. These complex flow transition effects, combined with non-negligible streamline curvature effects due to the low Re, pose a challenge for traditional CFD simulations, since the boundary layer around the airfoil must be accurately predicted to successfully determine the flow separation, transition, and reattachment phenomena. These in turn dictate the overall aerodynamic characteristics of the airfoil. For low Re flow, a laminar flow region is found to exist on the surface of the airfoil for a large range of angle of attack (α). At a critical value of α, the laminar boundary layer separates from the airfoil surface, transitions to turbulence, reattaches as a turbulent boundary layer, and finally separates from the downstream portion of the airfoil. In these cases, use of traditional EVMs results in inaccurate prediction of flow characteristics. Hence, a turbulence model sensitive to both T-RC effects is needed for the CFD simulations of elliptic airfoils. Further discussion on transitional and turbulent flow behavior over an elliptic airfoil can be found in Refs. [78,101].

In the present study, we have employed a 2D elliptic airfoil with a thickness to chord length ratio of 16%. Numerical simulations using the new model were performed

on the static test case for a range of α from 0 deg to 20 deg and flow Re, based on chord length and freestream velocity of 3×10^5. This Re was specifically chosen since it lies in the transitional range with a possibility of completely laminar, laminar-to-turbulent transition, and turbulent flow over the airfoil. This Re is also characteristic of the operating range for UAVs, for which boundary layer transition plays an important role in determining the aerodynamic characteristics of the airfoil [21,102]. Simulations were also performed on the airfoil using traditional EVMs, transition-sensitive models, and curvature-sensitive models for purposes of comparison with the new model.

A hybrid unstructured grid with 180,000 cells was constructed for the test case with higher grid point densities near regions with high surface curvature or steep flow gradients. Grid independence was verified as discussed previously. A structured O-type mesh was generated near the airfoil surface while the rest of the domain was filled with an unstructured triangular mesh. The grid transition from structured cells near the wall region to unstructured cells outside the wall boundary layer was defined smoothly in such a way that the centroid of the triangular cell matched the half height of the rectangular cell. The farfield boundaries were placed 10 chord lengths away from the airfoil and the surface of the airfoil was defined as a solid wall. The upstream and bottom boundaries were specified as velocity inlets, while the top and downstream boundaries were specified as pressure outlets. To ensure that the boundary locations did not influence the flow, additional simulations were performed on the test case with boundaries placed at 20 chord lengths away from the airfoil. No significant differences were observed in the results from the different geometries. The overall computational domain with the boundary conditions and a close-up of mesh in the vicinity of the LE are illustrated in

Fig. 5.18. All simulations were performed on the same grid with an inlet air velocity of 4.38 m/s, a turbulent viscosity ratio of 10, and a turbulence intensity of 0.12%.

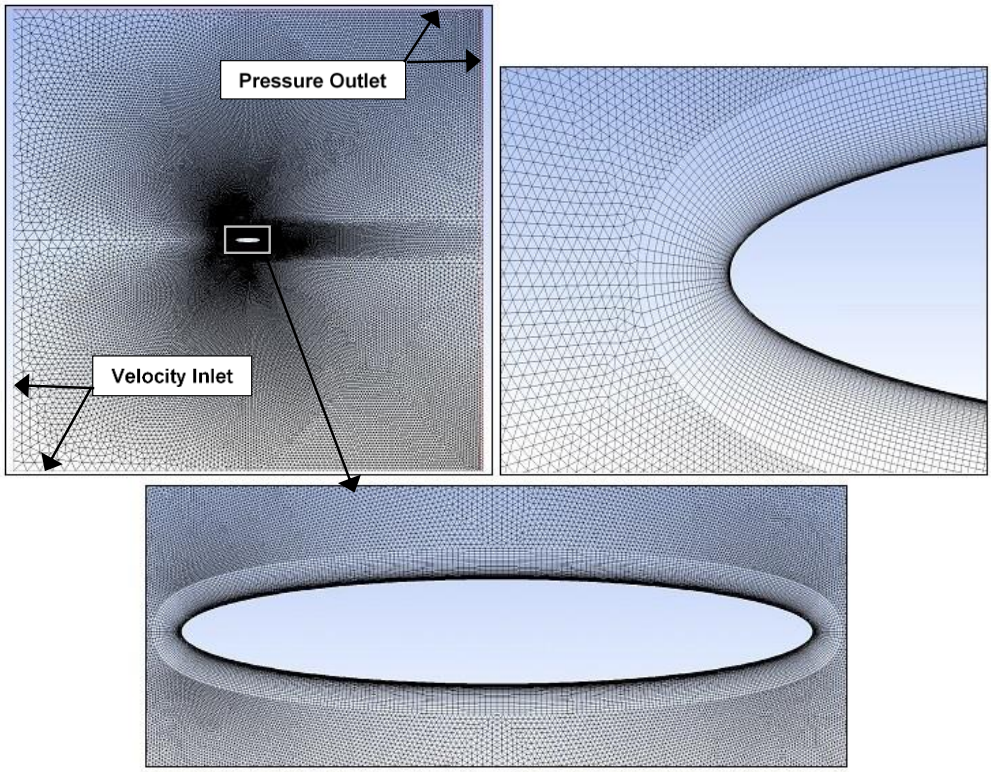

Figure 5.18 Computational domain for elliptic airfoil test case and close-up of mesh in the vicinity of the LE highlighting the multi-topology grid

Figure 5.19 shows the lift and drag coefficient plots obtained from the simulations versus the smooth and tripped case experimental data of Kwon and Park [103]. It is observed that both the new model and the transition-sensitive k-k_L-ω model predict a laminar boundary layer on the suction surface of airfoil for α up to 6 deg. Thereafter, both the models predict a LSB on the suction surface near the LE for $\alpha \geq 6$ deg, and hence, a shift in the lift curve slope predicted by the models between $\alpha = 4$ deg and 6 deg matches

accurately with the experiments. On the other hand, both SST k-w and curvature-sensitive SST k-ω-v^2 models fail to predict the flow transition behavior over the suction surface of the airfoil and therefore, a discrepancy is observed in the predicted lift coefficient values. Although flow transition behavior was captured accurately by the k-k_L-ω model, it failed to predict the airfoil stall point accurately. Similarly, the fully turbulent SST k-ω model predicted the stall of the elliptic airfoil considerably later than the experimental data indicate. However, the new model predicted the stall point of the airfoil at α = 11 deg and the lift coefficient curve matched very closely with the experiments. The curvature-sensitive SST k-ω-v^2 also predicted stall close to the experimental results at α = 12 deg. Both of the curvature-sensitive models predict earlier stall due to boundary layer separation. The convex curvature of the airfoil surface leads to a suppression of the turbulent shear stress [43] which manifests in the models as a reduction of the eddy-viscosity. As a consequence, the near wall momentum in the boundary layer is reduced, leading to separation at lower angle of attack than predicted by the traditional EVMs.

All of the turbulence models predicted the drag coefficient values reasonably well in comparison with experimental results prior to airfoil stall. Significant discrepancies in the drag values are only observed for the k-k_L-ω and SST k-w models for $\alpha > 10$ deg, and this can be attributed to the delayed stall prediction. On the whole, the new model, being sensitive to both flow transition and curvature effects, most accurately predicted the lift and drag coefficient values of the elliptic airfoil in comparison with the smooth case experimental data. To the authors' knowledge, this is the first time in the open literature that the qualitative aerodynamic characteristics of an elliptic airfoil at low Re have been accurately predicted by a single RANS based eddy-viscosity turbulence model. Most

significantly, the simulations indicate that transition-sensitive modeling is necessary to predict flow transition from laminar-to-turbulent at low angles of attack, and curvature-sensitive modeling is necessary to accurately resolve the stall point of the airfoil.

Mean pressure distribution over the airfoil surface for various angles of attack is shown in Fig. 5.20. For α = 0 deg, 2 deg, and 4 deg, the new model and the SST k-w-v^2 model predictions match the trends of the experimental data, though both show an underprediction of the negative pressure on the suction surface. This underprediction was present for all of the models investigated. Qualitatively, however, there are some differences, as the new model results tend to indicate earlier separation on the downstream portion of the suction surface, which is consistent with the differences in the experimental data between the smooth and tripped cases. Particularly, for the case of α = 4 deg, the differences between the two models contribute to the fact that the lift curve for the new model more closely matches the smooth case experimental data, while that for the SST k-w-v^2 model more closely matches the tripped case data. The most significant difference between the two models was noted for the case of α = 6 deg, for which a pressure plateau region next to the negative pressure peak point (indicating the formation of a LSB) was predicted by the model on the suction surface near the LE of the airfoil. The predicted bubble size matched closely with the smooth case results. For all angles of attack, the pressure coefficient distributions of the SST k-w-v^2 model matched closely to the tripped case results as a turbulent boundary layer was predicted from the LE of the airfoil onward. Due to the unavailability of experimental data, pressure distributions over the airfoil surface are not shown for α > 6 deg. As α increased, it was observed from the new model predictions that the separation bubble moved toward the LE with a gradual

reduction in size and finally burst at a flow angle of 12 deg, indicating that the airfoil had stalled.

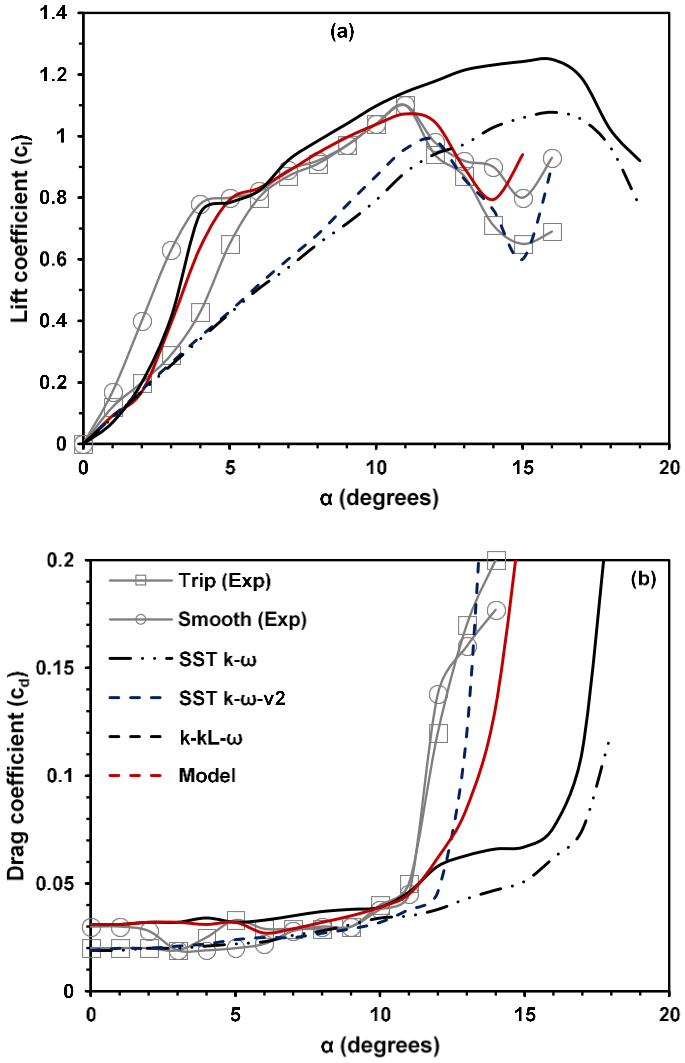

Figure 5.19 (a) Lift coefficient (c_l) and (b) drag coefficient (c_d) curves for elliptic airfoil plotted as a function of angle of attack (α)

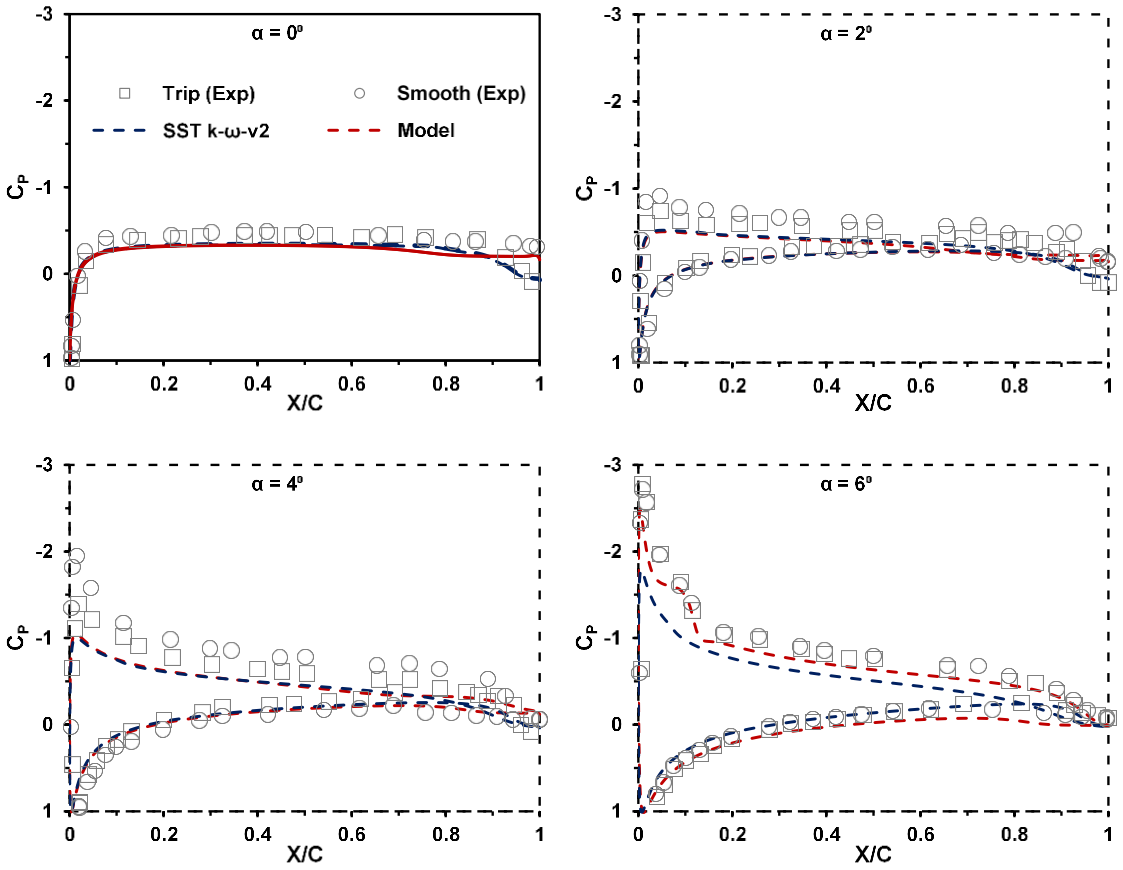

Figure 5.20 Time-averaged pressure coefficient profiles over elliptic airfoil for the new model in comparison with curvature-sensitive SST k-ω-v^2 model and experimental results

Time-averaged TKE contours for the elliptic airfoil obtained from the new model are shown in Fig. 5.21. The contours are shown for α ranging from 0 deg to 9 deg. The new model predicts laminar boundary layers over the surface of the airfoil for $\alpha < 6$ deg, and hence, very low levels of TKE were observed near the airfoil surfaces. For $\alpha \geq 6$ deg, the model captured the flow transition downstream of the separation bubble on the suction surface of the airfoil. The reattached turbulent boundary layer was much more energetic than the laminar boundary layer upstream of the bubble and resulted in an attached flow over most of the airfoil surface. As a consequence, higher TKE distribution

was observed on the suction surface of the airfoil near the flow transition and reattachment points. For the TKE contours shown in Fig. 5.21, higher energy distributions are observed for α = 9 deg, near the LSB region and near the separated flow region around the trailing edge.

Figures 5.22 and 5.23 show a comparison of mean velocity contours obtained from the new model and the SST k-w-v^2 model for α = 6 deg and 9 deg. In the experiments performed by Kwon and Park [103], flow transition was observed in the smooth case for $\alpha \geq 6$ deg on the suction surface near the LE of airfoil. Thereafter, lift coefficient (c_l) curves for both smooth and tripped cases behaved similarly. The new model accurately captured the flow behavior observed in the experiments. At α = 6 deg, the new model predicts the laminar boundary layer separation, transition to turbulent flow, and reattachment on the suction surface near the LE of airfoil. In contrast, SST k-w-v^2 predicts a turbulent boundary layer from the LE of the elliptic airfoil for all angles of attack. As a result, flow separates earlier from the trailing edge when compared to the flow separation points predicted by the new model. It can be seen in the contours that the SST k-w-v^2 model failed to predict the formation of a LSB, and the flow separation point near the trailing edge occurs farther upstream when compared to the predictions of the new model.

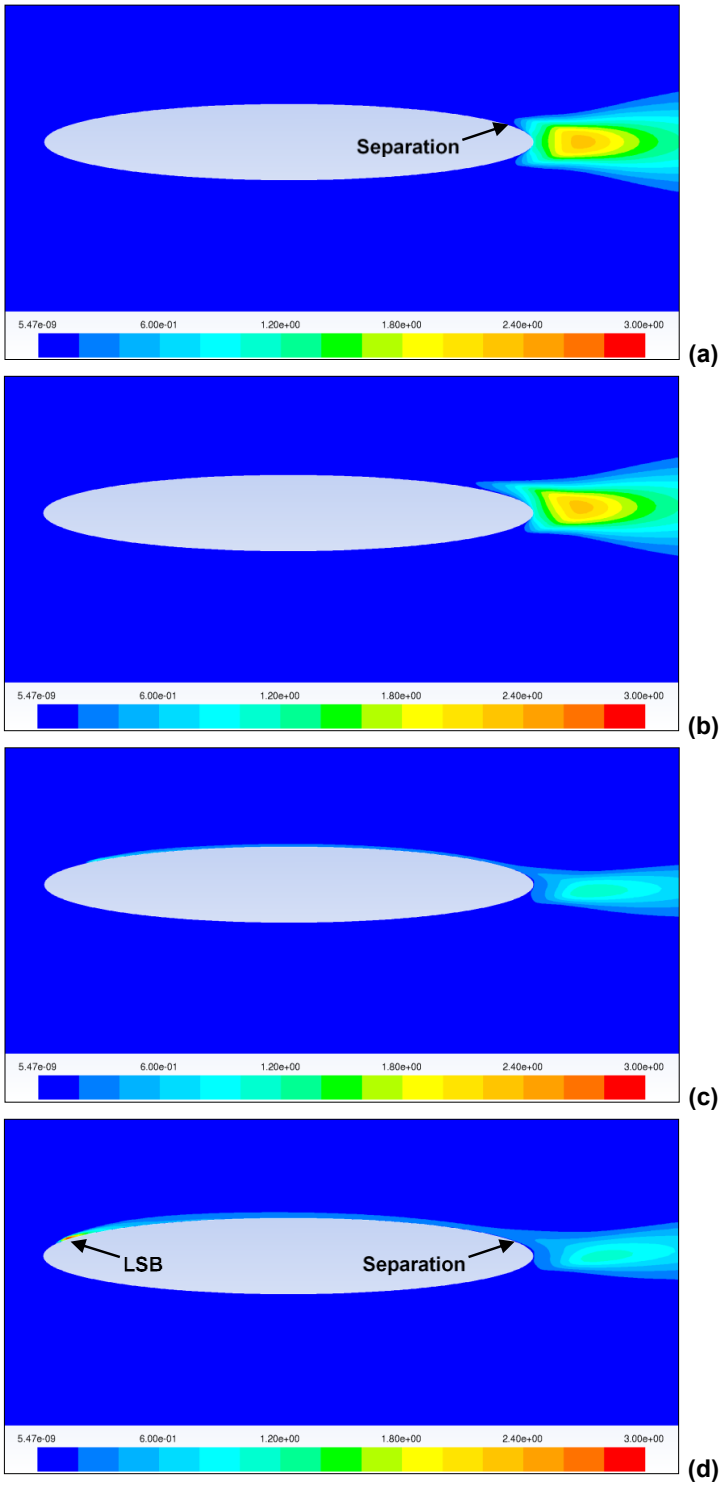

Figure 5.21 TKE distributions around elliptic airfoil test case from the new model at α (a) 0 deg, (b) 3 deg, (c) 6 deg, and (d) 9 deg

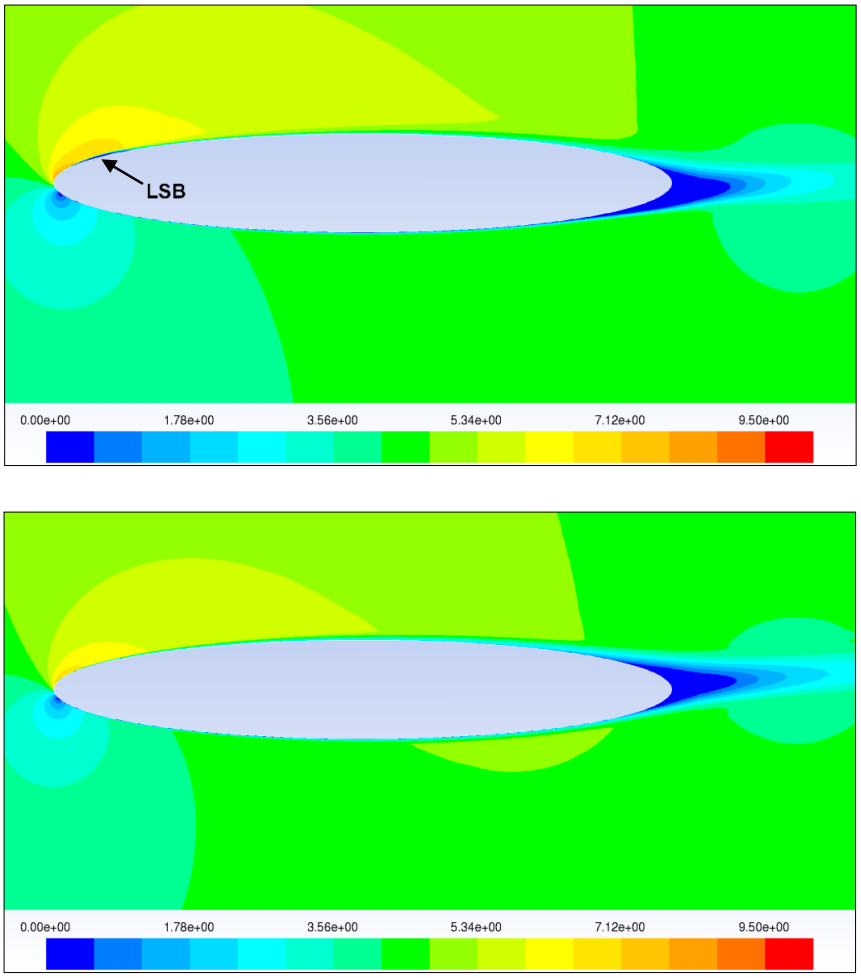

Figure 5.22 Mean velocity contours of elliptic airfoil at $\alpha = 6$ deg for (a) new model and (b) curvature-sensitive SST k-ω-v^2. LSB is observed on the suction surface near LE for the new model

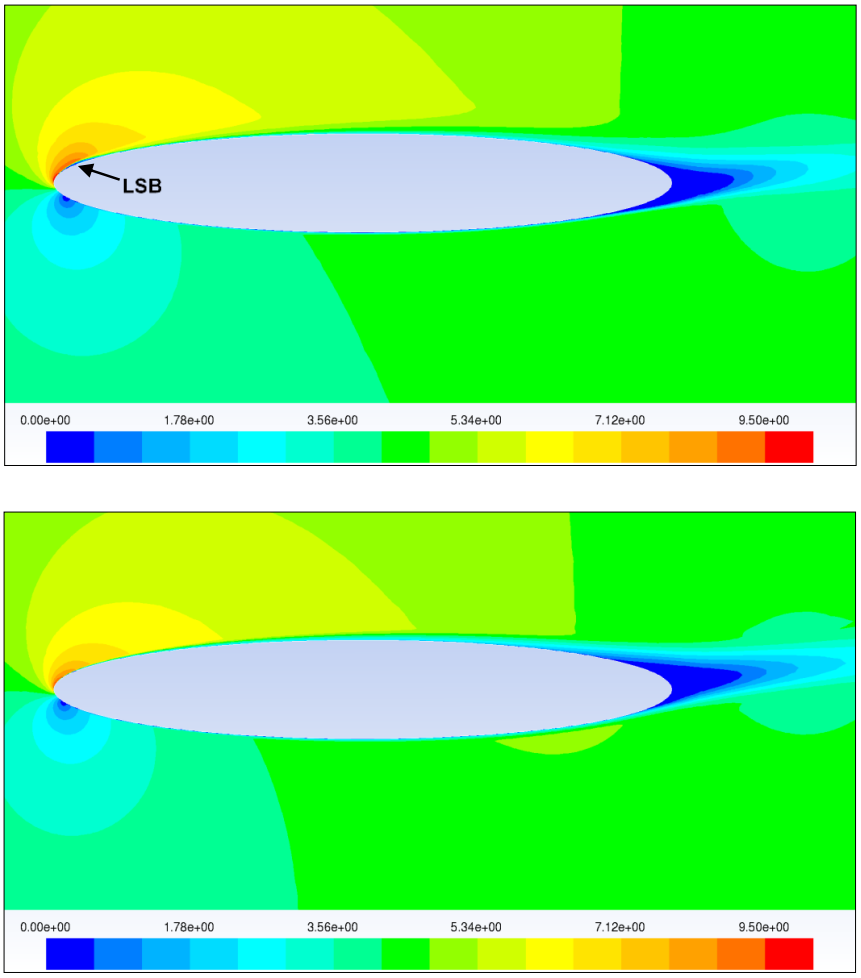

Figure 5.23 Mean velocity contours of elliptic airfoil at $\alpha = 9$ deg for (a) new model and (b) curvature-sensitive SST k-ω-v^2

Overall, the new model predictions show closer agreement with the experimental data than the predictions using any of the other models, including the transition-sensitive k-k_L-ω model. The new model is capable of accurately predicting the non-linear increase in the lift coefficient curve at low angles of attack, and the stall point of the airfoil. The model also predicts the formation of a LSB on the suction surface of airfoil due to the

flow transition from laminar-to-turbulent, and more accurately predicts the turbulent separation location on the aft surface of the airfoil.

5.6 Summary and Conclusions

A new RANS-based model has been proposed in this study, which incorporates the capability to resolve streamline curvature and flow rotation effects into a modified version of the transition sensitive k-k_L-ω model. A new transport equation for a structural variable related to the transverse velocity fluctuations (v^2), initially proposed for the curvature-sensitive SST k-ω-v^2 model, was added to the transition-sensitive k-k_L-ω model. The added transport equation introduces the physical effects of RC into the model. The eddy-viscosity in the new model was redefined in such a way that RC effects are reproduced by the model in turbulent flows and in the absence of any significant streamline curvature effects, the value of v^2 equals k_T and the results predicted by the model are similar to the predictions of the transition sensitive k-k_L-ω model. The new model was implemented into the commercial solver ANSYS FLUENT. To assess the model performance, simulations were performed on several test cases involving flow transition and streamline curvature effects.

For the rotating channel flow test case, the new model successfully captured the effect of system rotation and produced results in close agreement with the DNS data. As expected, the new model results agreed well with the curvature-sensitive SST k-ω-v^2 model for fully turbulent flows. For the ZPG flat plate test case, the new model accurately predicted flow transition from laminar to turbulent on the surface of the plate and agreed well with the experimental results. As the freestream turbulence intensity was increased, the flow transition point moved upstream toward the LE of the plate and this

flow behavior was also captured by the model. For the circular cylinder test case, the performance of fully turbulent models were compared with the new model to accurately capture the flow transition behavior on the cylinder surface and drag crisis region in the critical flow regime. Although the new model captures the flow transition behavior and other qualitative trends not observed in the results from fully turbulent models, discrepancies were observed between the drag coefficient values of the experimental and computational results. These discrepancies observed in the supercritical flow were attributed to the delayed prediction of flow separation from the cylinder surface.

On the whole, improved results were obtained using the new model when compared to the predictions of fully turbulent EVMs. For the elliptic airfoil test case, the new model produced results in close agreement to the experimental results in terms of lift and drag, and the predicted stall point of the airfoil matched closely with the experimental results. In contrast, fully turbulent models were unsuccessful in predicting the boundary layer transition and hence, failed to predict the nonlinear increase in lift coefficient values at low angles of attack and also stall of the airfoil. Overall, the results indicate the potential ability of the new model to successfully resolve the complex effects of flow transition and streamline curvature effects with reasonable engineering accuracy, for a relatively small increase in computational cost. Results also suggest that the model has potential as a practical tool and is highly desirable for solving low Reynolds number flows over blunt bodies for the prediction of flow transition and curvature effects. Future research efforts will focus on testing the new model's performance on practical three-dimensional applications, and extending the proposed concept to more advanced closure methods, specifically nonlinear EVMs or ASMs.

CHAPTER VI

COMPUTATIONAL FLUID DYNAMICS STUDY OF SEPARATED FLOW OVER A THREE-DIMENSIONAL AXISYMMETRIC HILL

This study investigates the ability of the proposed four-equation EVM in accurately predicting turbulent flow separating from a 3D axisymmetric hill by means of numerical simulations. The four-equation model is designed to exhibit physically correct responses to flow transition, streamline curvature, and system rotation effects. The model was earlier tested on various canonical and complex 2D cases with results showing significant improvement in predictions when compared to other popularly available EVMs. In this study, we present a more complex 3D application of the model. The test case includes a hill of height 2δ mounted in a channel and subjected to an approach turbulent boundary layer thickness of δ. The flow Reynolds number based on the hill height (Re_H) is 1.3×10^5. For validation purposes, CFD simulation results obtained using the k-k_L-ω-v^2 model are compared with two other RANS models – fully turbulent SST k-ω and transition-sensitive k-k_L-ω, and with experimental data. Results obtained from the simulations in terms of mean flow statistics, pressure distribution, and turbulence characteristics are presented and discussed in detail. These indicate that both the complex effects of flow transition and streamline curvature have to be taken into account to significantly improve RANS-based CFD predictions for applications involving blunt or curved bodies in low Re regime.

6.1 Introduction

Boundary layer flows over 3D curved bodies such as an axisymmetric hill are of considerable interest to the CFD community due to the complexities involved in the accurate prediction of flow separation patterns and wake structure downstream of the hill. On the lee side of a hill, the flowfield is generally dominated by two unsteady phenomena – large vortical structures shed intermittently or periodically, and multiple patches of spatially varying boundary layer separations and reattachments. Such unsteady phenomena, commonly observed in highly loaded aircraft wings and marine and naval applications have a significant impact on the efficiency and operational characteristics. Moreover, understanding the mechanics of flow (speed, direction, and turbulence) over a hill is important in a wide range of applications, including extraction of wind energy, safety of structures, dispersion of air pollution, and aviation safety [104]. To study these complex flows using numerical simulations, firstly, it is vital to understand the underlying mechanisms of flow separation and 3D vortex formation on curved surfaces; and secondly, a simple, robust, and computationally inexpensive turbulence model capable of accurately resolving the flow features must be developed. In this study, we investigate a recently proposed four-equation RANS model capable of capturing both flow transition and rotation/curvature effects from curved bodies in a low Re separated flow over a 3D hill test case.

In the test case considered, as the flow approaches the hill, it accelerates on the windward side and around the sides of the hill, but decelerates on the lee side. Depending upon the height and shape of the hill and the speed of flow, lee side separation patterns vary. At low Re, flow separates on the lee side and reattaches at the foot with the viscous

layer downstream of the hill containing low-frequency motions. At high Re, flow separation is observed aft or at the center of the hill. Flow coming in from the sides of the hill and vortical separations occurring on the lee side merge into two large streamwise vortices that energize the boundary layer downstream of the hill. These vortices produce large levels of turbulence near the centerline with low frequency motions and contribute to the turbulent diffusion process. Previous experimental studies have confirmed and documented this flow phenomena in detail. Ishihara et al. [105] investigated a laminar boundary layer flow with $Re_H = 1.1 \times 10^4$ over an axisymmetric hill that had a ratio between the incoming turbulent boundary layer thickness and the hill height of $H = 9\delta$. Simpson et al. [106] studied a higher Re flow of 1.3×10^5 over an axisymmetric hill with a smaller hill height of $H = 2\delta$. The study was carried out using advanced laser-Doppler velocimeter (LDV) techniques. Further experiments were carried by Byun et al. [107] for two different hill heights of $H = \delta$ and 2δ using 3D fiber-optic LDV techniques. The large hill topology was similar to the one used in Ref. [106]. The flow and hill configuration considered in the present study match the experiments by Simpson et al. [106].

Given the complexities involved in predicting flow phenomena on the lee side of the hill, which is characterized by multiple curved flow separations and reattachments and formation of vortices, several numerical studies have been carried out in the recent past to provide a deeper understanding into the flow behavior and bring quantitative improvements to the turbulence models. Most of these studies concentrated on the behavior of either LES or hybrid models in accurately reproducing the flow separation patterns and capturing the wake region effects. Reasonable agreement between LES and/or hybrid models and experiments in terms of mean flow statistics and pressure

distribution were reported in studies from Refs. [108-110], however, notable differences were observed in the prediction of flow topology on the lee side of the hill. Numerical simulations using several non-linear EVMs were presented in Refs. [110,111], which indicate that none of the RANS models were able to capture the important flow features accurately. A single DNS study of the hill flow has been published recently [112], although the flow Re was much lower compared to the experiments at 6500. This is due to the fact that a high Re DNS requires a very large amount of computational resources which is often prohibitively difficult to meet with the current state of technology.

LES is widely used for studies involving highly 3D or separated flows where two-equation EVMs often fail to resolve the complex flow features accurately, and in free shear layer flows where the grid resolution requirements are nearly independent of Reynolds number. However, LES are computationally expensive compared to RANS and hence are not widespread for use in industrial engineering problems. RANS models, to date, are the most common closure approach adopted in industrial CFD applications, given the fact that they are computationally inexpensive, can be applied to general grid structures (i.e., structured, unstructured, and hybrid grids), and produce results with reasonable engineering accuracy for certain classes of flows which exhibit some degree of universal behavior, for example, the prediction of turbulent boundary layer, to fairly complex flow configurations. Although, they are known to have difficulty in dealing with problems for which the details of the geometry are relevant to the turbulence dynamics. This is due to the strong flow-dependent nature of the larger eddies which contribute most to the energy and momentum transfer and cannot be modeled in the same way for different flows as the smaller eddies which have somewhat universal behavior.

Furthermore, RANS models perform poorly in problems involving boundary layer transition from laminar-to-turbulent, and also for the prediction of momentum, heat and mass transfer in regions of separated flow [4]. In the current test case of flow over an axisymmetric hill, the resolution of the flowfield in the presence of both streamwise and spanwise pressure gradients, and complex vortical separations and reattachments of the boundary layer on the lee side proves to be a demanding task for traditional EVMs when compared to attached boundary layer flows. Also, conventional EVMs do not explicitly contain streamline curvature and/or system rotation dependent terms in their formulation. These EVMs typically have to be coupled with empirical transition correlations or additional transport equations that include flow transition effects and empirical functions sensitive to rotation effects, without which these models predict inaccurate results and are not suitable for addressing boundary layer transition and curvature effects in numerical simulations.

An EVM sensitive to both flow transition and RC effects would be a useful tool for CFD predictions of low/high Re flows over blunt/curved bodies, including applications in aerospace, automotive, and marine systems. In the present study, we investigate the proposed four-equation EVM sensitive to both flow transition and curvature effects [76]. The new model, a variant of the commercially available transition-sensitive model k-k_L-ω, is capable of resolving two complex effects with engineering accuracy: (i) laminar-to-turbulent boundary layer transition without any empirical transition functions or problem-dependent modifications needed to explicit fix the transition point; and (ii) streamline curvature and system rotation effects without any ad hoc modifications. To accomplish this, the transport equation for a transverse turbulent

velocity scale (v^2) proposed by Dhakal and Walters [51] was blended with the three-equation transition sensitive k-k_L-ω model proposed by Walters and Cokljat [34]. In the proposed model, the eddy-viscosity was redefined such that RC effects are reproduced in turbulent flows, and in the absence of any significant streamline curvature effects, results predicted by the new model are similar to the predictions of the transition-sensitive k-k_L-ω model. The proposed model solves transport equations for turbulent kinetic energy (TKE) (k_T), laminar kinetic energy (LKE) (k_L), scale-determining variable (also interpreted as the specific dissipation rate ω), and structural variable (v^2) in addition to the mean flow equations.

The objectives of the present study are: to evaluate the performance of the new model versus the transition-sensitive k-k_L-ω and fully turbulent SST k-ω [26] models for the prediction of 3D separated turbulent flow over an axisymmetric hill; and to illustrate the behavior of the four-equation model in the presence of separating flow and vortex shedding from the hill surface. An overview of this chapter is as follows. After the introduction in Sec. 6.1, the computational methodology employed in this work, the geometric description of the axisymmetric hill, and the relevant flow parameters are presented in Sec. 6.2. Results obtained from the numerical simulations are presented in Sec. 6.3, and lastly, conclusions are included in Sec. 6.4.

6.2 Numerical Method and Computational Configuration

CFD simulations of turbulent flow over an axisymmetric hill using the three models – fully turbulent SST k-ω, transition-sensitive k-k_L-ω, and transition and curvature-sensitive k-k_L-ω-v^2 – were performed in the finite-volume solver ANSYS FLUENT. The first two models (SST k-ω and k-k_L-ω) are built-into and commercially

available with the solver. The proposed model (k-k_L-ω-v^2) was directly implemented using the UDF capability available with the solver. For all simulations, an incompressible flow with constant viscosity was considered. A pressure-based double precision solver was used with the SIMPLE scheme [91] for pressure-velocity coupling. The PRESTO! scheme was utilized for discretization of pressure terms, and a least squares cell based method was used for the computation of spatial gradients [92]. The convective terms of all equations were discretized using a second-order upwind scheme. A steady-state RANS approach was adopted for all the CFD simulations carried out in this study. All simulations were run to full convergence, based on the reduction of residuals of each monitored variable until a numerically steady-state condition was obtained.

The hill shape and flow configuration considered in this study matched the experiments by Simpson et al. [106]. The hill shape is defined as

$$\frac{y(r)}{H} = -\frac{1}{6.04844}\left[J_0(\Lambda)I_0\left(\Lambda\frac{r}{a}\right) - I_0(\Lambda)J_0\left(\Lambda\frac{r}{a}\right)\right] \tag{6.1}$$

where $y(r)$ is the shape function of the radius r, J_0 is the Bessel function, and I_0 is the modified Bessel function. The coefficients include height of the hill H = 78mm, Λ = 3.1926, and radius of the circular base of the hill $a = 2H$. The shape of the axisymmetric hill plotted in X-Y plane is shown in Fig. 6.1.

The present test case includes a 3D axisymmetric hill mounted on the bottom surface of a channel. The size of the computational domain in the streamwise, wall normal, and spanwise directions are 32H, 3.2H, and 11.6H, respectively. The inlet, outlet, and spanwise boundaries of the domain were located at a distance of 12.8H, 19.2H, and 5.8H, respectively, from the center of the hill. The size of the computational domain was determined from other numerical studies which used similar flow configuration. A

summary of the computational domain sizes used in the present versus previous studies is given in Table 6.1. The inlet distance from the center of the hill was higher in our study in comparison with other numerical studies, and this was made to ensure negligible flow acceleration effect on the hill.

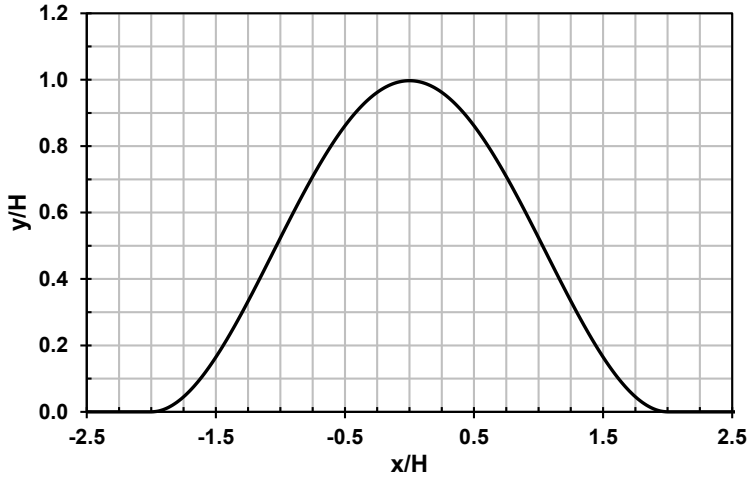

Figure 6.1 Shape of the axisymmetric hill in X-Y plane

Table 6.1 Summary of computational domain sizes used in present vs previous numerical studies

Numerical Studies	Streamwise	Wall normal	Spanwise
Present study	32*H*	3.2*H*	11.6*H*
Patel et al. [109]	9.5*H*	3.2*H*	3.4*H*
Persson et al. [110]	12*H*	3.2*H*	3.4*H*
Wang et al. [111]	16*H*	3.2*H*	4.4*H*
Castagna et al. [112]	20*H*	3.2*H*	8.4*H*
Garcia et al. [113]	20*H*	3.2*H*	11.6*H*
Tessicini et al. [114]	16*H*	3.2*H*	11.6*H*

A high quality 3D structured mesh was generated for the computational domain using the commercial grid generation software GAMBIT. The wall distance for the first-cell had a y^+ value less than unity over the entire bottom surface (wall region) of the domain which includes the hill surface. This approach was followed to accurately resolve the boundary layer region and to capture the flow separation from the hill surface. The computational domain and mesh generated for the test case with a close-up near the vicinity of the hill are shown in Fig. 6.2. The cell spacing was verified using a grid independence study, in which the grid was subsequently refined in all the three directions of the domain until the solution remained effectively unchanged between the grid shown in this study (refined grid) and its coarser version. Figure 6.3 demonstrates an example of this study, wherein the profiles of normalized TKE and velocity obtained from the proposed model using the coarser and refined grids are shown at locations corresponding to $x/H = 3.63$ and $z/H = 0.0$. Acceptable differences were observed in the results from the refined grid used in this study and its coarser version, hence it was assumed that the CFD simulations were grid independent. The refined grid used in this study was generated with a total of 6,856,000 computational cells, and the coarser grid had 3,440,500 cells.

The boundary conditions for upstream and downstream surfaces of the computational domain were specified as velocity inlet and pressure outlet, respectively, and the remaining surfaces which include, bottom, hill, top, and sides were specified as wall boundary (mean velocities set to no-slip). A fully-developed turbulent boundary layer profile was enforced at the inlet plane to match the flow conditions to the experiments. The velocity profile was calculated using a power law approximation defined as

$$v_x = \begin{cases} U_o \left(\frac{y}{\delta}\right)^{\frac{1}{n}}, & y < \delta \\ U_o, & y \geq \delta \end{cases} \tag{6.2}$$

where U_o is the reference velocity of 27.5 m/s, y is the wall normal distance, δ is the boundary layer thickness, and $n = 7$. For this test case, a boundary layer with $Re_\theta \approx 7300$ was obtained at the upstream edge of the hill. A similar inlet velocity profile was also used in the study of Persson et al. [110]. At the inlet plane, a freestream turbulence intensity (Tu_∞) of 0.1% and turbulent viscosity ratio of 10 were prescribed for all the three turbulence models.

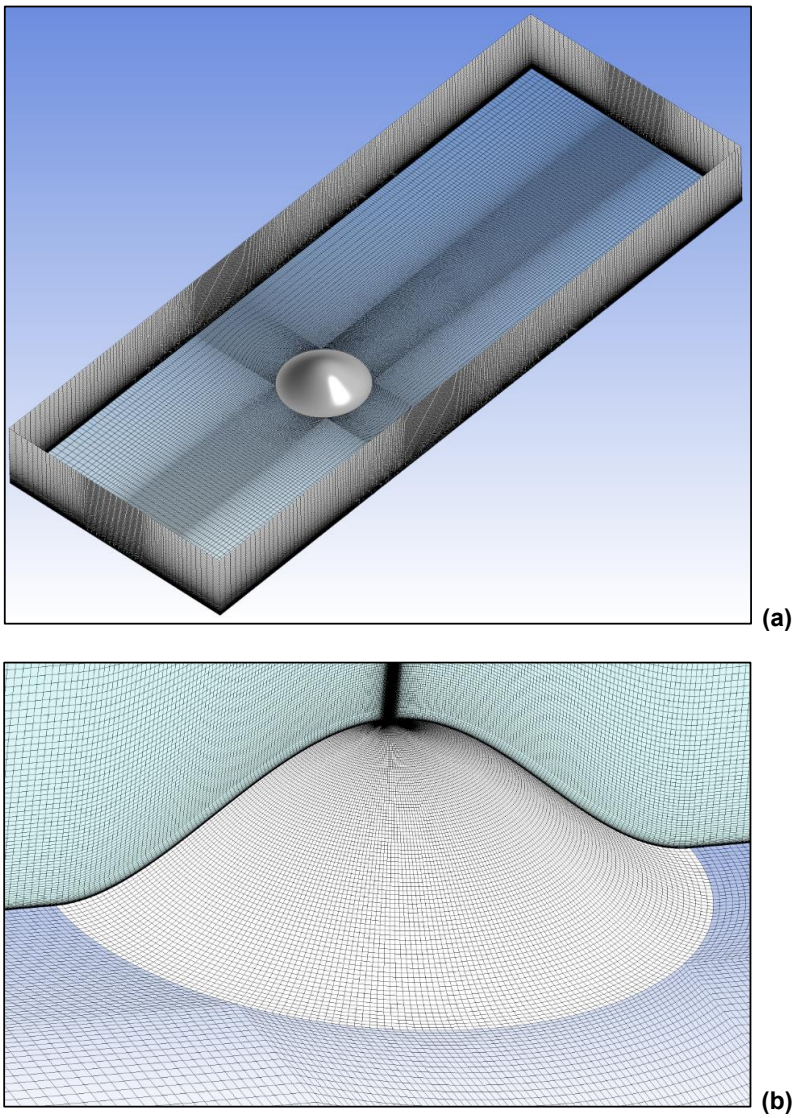

Figure 6.2 (a) Computational domain of the axisymmetric hill test case viewed from top and (b) close-up of the structured mesh in the vicinity of the hill

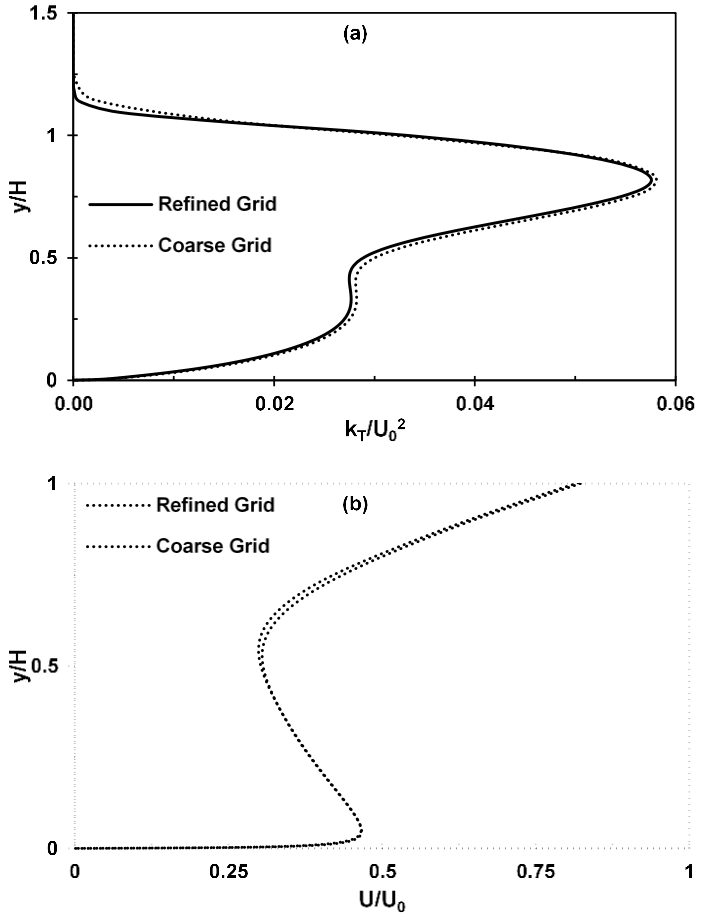

Figure 6.3 Example grid refinement study for the proposed model at (a) $x/H = 3.63$ and (b) $z/H = 0.0$

6.3 Results

Figure 6.4 shows the contours of pressure coefficient (C_p) over the hill surface obtained using all the three RANS models in comparison with experimental data [106]. As the boundary layer approaches the hill, flow decelerates near the leading edge which results in a small recirculation region. This region was predicted by all the three models and is observed in Fig. 6.4 along with a patch of high pressure. However, the presence of a recirculation region was not mentioned in the experiments. As the flow reattaches back

to the surface and accelerates until the top of the hill, a low pressure (maximum suction pressure) region is created. Qualitatively, all the three models predicted this flow phenomena accurately, although SST k-ω produced a larger low pressure region. On the lee side, flow separates from the hill surface due to the presence of an adverse pressure gradient. Pressure values predicted by k-k_L-ω-v^2 matched closely to the experiments, while SST k-ω underpredicted pressure values due to early flow separation from the hill surface and presence of a large reverse flow region (see Fig. 6.6 (d)). The k-k_L-ω model slightly overpredicted the pressure values, however produced better results compared to SST k-ω.

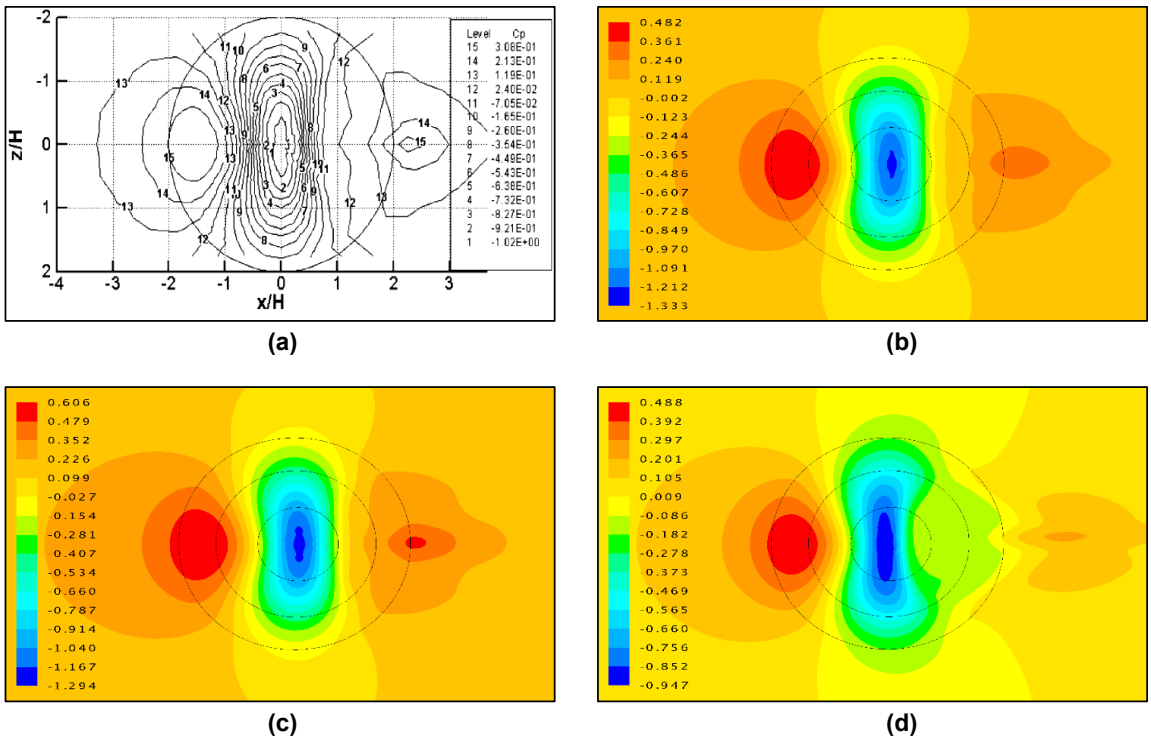

Figure 6.4 Comparison of Cp contours over the hill surface for (a) Experiments, (b) k-k_L-ω-v^2, (c) k-k_L-ω, and (d) SST k-ω models

Pressure coefficient profiles along the centerline of the hill ($z/H = 0$) are shown in Fig. 6.5. It is observed that all the three models predict higher C_p values on the windward side ($x/H < -1.5$) of the hill when compared to experiments [106]. On the hill surface and in the wake region, k-k_L-ω-v^2 predictions match the trends of the experiments very closely. Especially, on the lee side and in the wake region ($x/H > 0.5$), better results are produced by the new model even when compared to the predictions of DES and LES models presented in Persson et al. [110]. The k-k_L-ω model predicted an attached flow for most part of the hill surface on the lee side, followed by flow separation near the foot of the hill (see Fig. 6.6 (c)). This flow behavior resulted in a high pressure in the wake region and the same can be observed from the pressure coefficient curve as well. A higher C_p value was predicted by SST k-ω at $x/H = 0$, when compared with the other two models. A sudden shift in the C_p curve for $x/H > 0$ is observed for SST k-ω due to early flow separation on the lee side, which resulted in a lower pressure value in the wake region.

Flow separation and the formation of a recirculation bubble on the lee side along the centerline of the hill ($z/H = 0$) are shown in Fig. 6.6. The region under the black line in Figs. 6.6 (b)–(d) indicates a recirculation bubble. The new model predicts a flow separation point closer to experimental results at $x/H \approx 1$, although the height of the recirculation region did not match the experiments [107]. The transition-sensitive k-k_L-ω model predicted a delayed and relatively small flow separation region near the foot of the hill. Flow separation using the SST k-ω model was predicted too early and a very large recirculation region was observed on the lee side. The curvature effects resulting from the hill surface leads to a suppression of the turbulent shear stress [43] which manifests in the

new model as a reduction of the eddy-viscosity. This results in the reduction of near wall momentum in the boundary layer and leads to earlier flow separation than predicted by the traditional EVMs. Since both the k-k_L-ω and SST k-ω models do not account for curvature effects in their formulation, discrepancies were observed in the prediction of flow separation locations. On the whole, better predictions were obtained from the k-k_L-ω-v^2 when compared to the other two models.

As the flow approaches the hill, it accelerates over the top and around the sides of the hill due to the presence of favorable pressure gradients. A backflow region is created on the lee side by the accelerating flow coming from the sides of the hill. When the flow passing over the hill meets with this back flow, high APGs are created, leading to flow separation from the hill surface. Furthermore, the presence of both streamwise and spanwise pressure gradients on the lee side pulls the outer flow inwards towards the center plane (X-Y). A combination of all these mechanisms, including flow over the hill, back flow, and flow from the sides results in a pair of recirculation regions on either sides of the center plane. This distinct pair of counter-rotating vortices (CRVP), as explained earlier, energize the boundary layer downstream of the hill. These vortices also produce large levels of turbulence near the centerline with low frequency motions and contribute to the turbulent diffusion process. The CRVP predicted by the k-k_L-ω-v^2 model downstream of the hill is shown in Fig. 6.7 (a). The vortex on the left (+Z) had a clockwise rotation and the vortex on the right (-Z) had a counter-clockwise rotation. The vortices are formed on either sides of the center plane (X-Y) at about $x/H \approx 0.9$. The formation of a CRVP on the lee side and merger into a single large vortex downstream of the hill, as observed in the experiments, is illustrated in Fig 6.8. The new model predicts

higher levels of TKE in the core of the CRVP, as expected. For the k-k_L-ω model, no vortex formation was observed from the velocity streamlines at the measured location (see Fig. 6.7 (b)). However, contours of TKE from the same model indicate the formation of a CRVP downstream of the foot of the hill (see Fig. 6.9). This must be due to the delayed and a tiny flow separation point predicted by the model downstream near the foot of the hill. Interestingly, the CRVP produced by the k-k_L-ω model never merged into a single large vortex as observed in the experiments. In contrast to the other two models, the SST k-ω model failed to predict a distinct CRVP downstream of the hill (see Figs. 6.7(c) and 6.10), instead produced a single large vortex with very high levels of TKE.

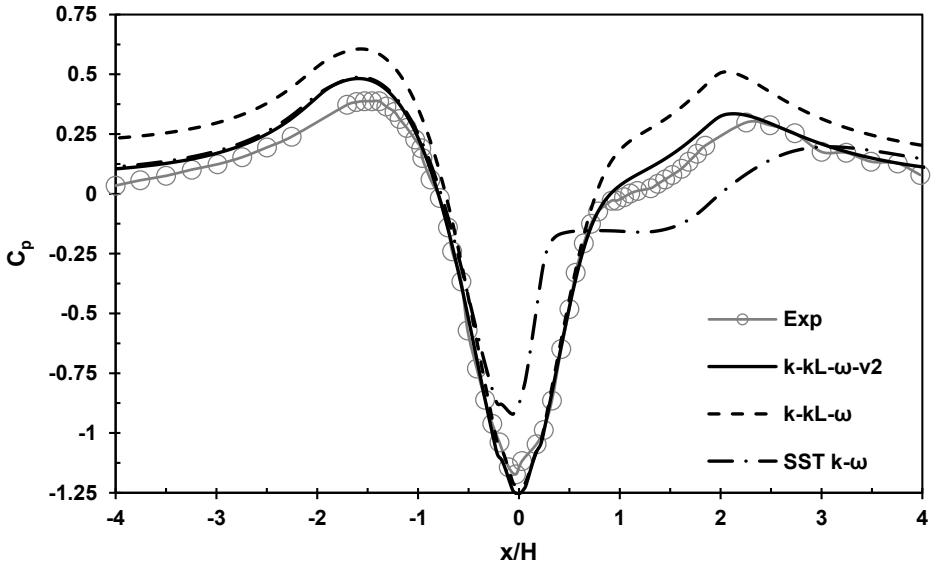

Figure 6.5 *Cp* profiles along the centerline ($z/H = 0$) for all the three turbulent models used in this study and in comparison with experimental data

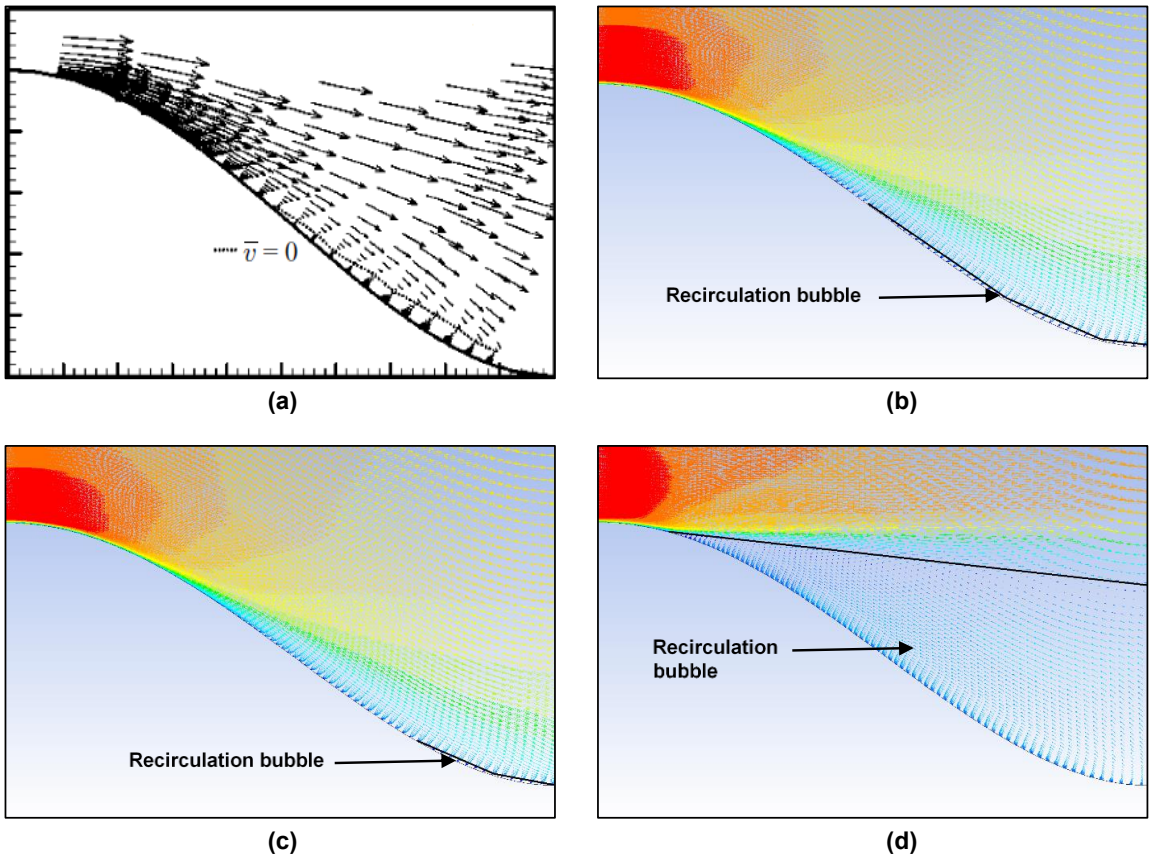

Figure 6.6 Comparison of velocity vectors along the centerline ($z/H = 0$) for (a) experiments, (b) k-k_L-ω-v^2, (c) k-k_L-ω, and (d) SST k-ω models

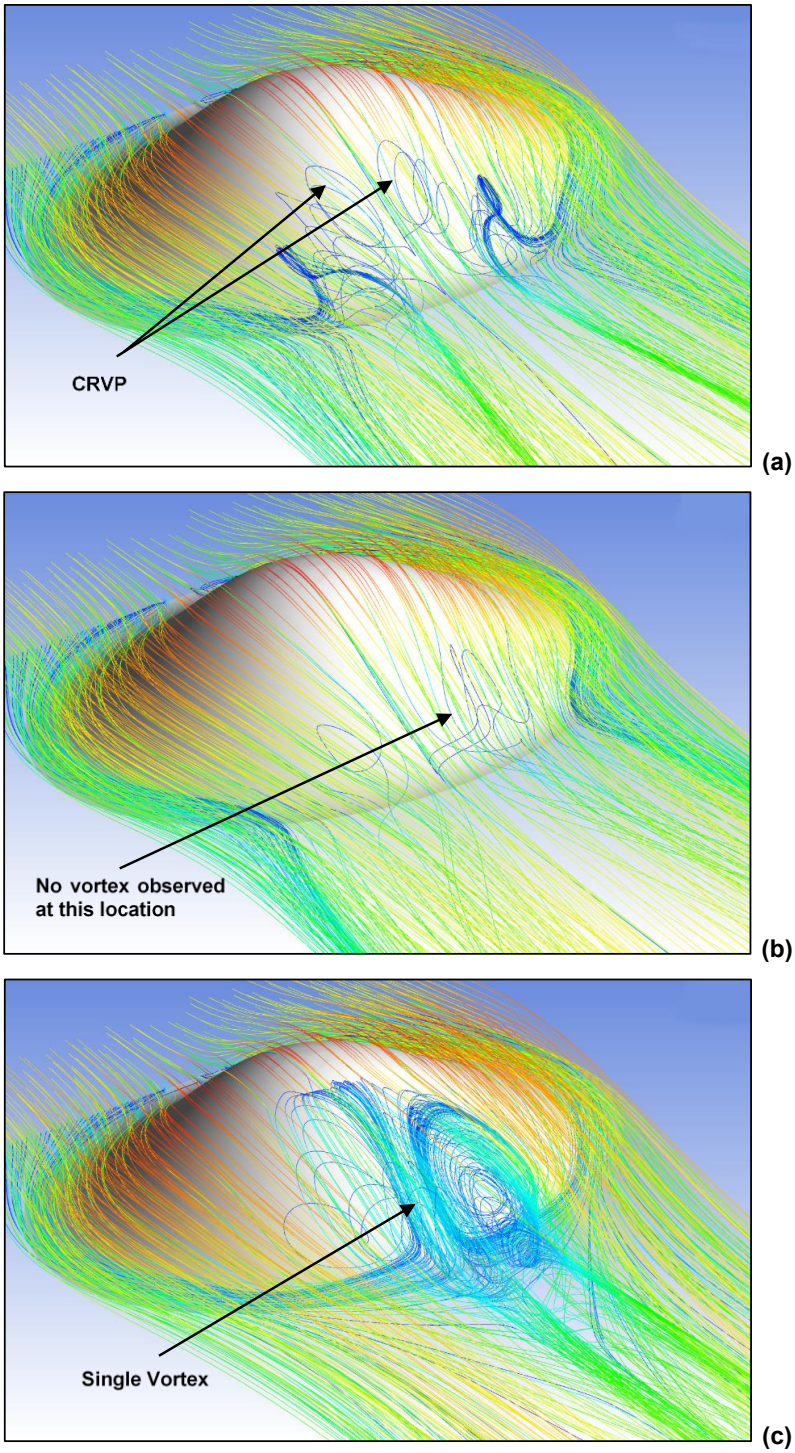

Figure 6.7 Predicted streamlines colored by velocity magnitude for (a) k-k_L-ω-v^2, (b) k-k_L-ω, and (c) SST k-ω models.

A pair of counter-rotating vortices are observed downstream of the hill for the proposed model

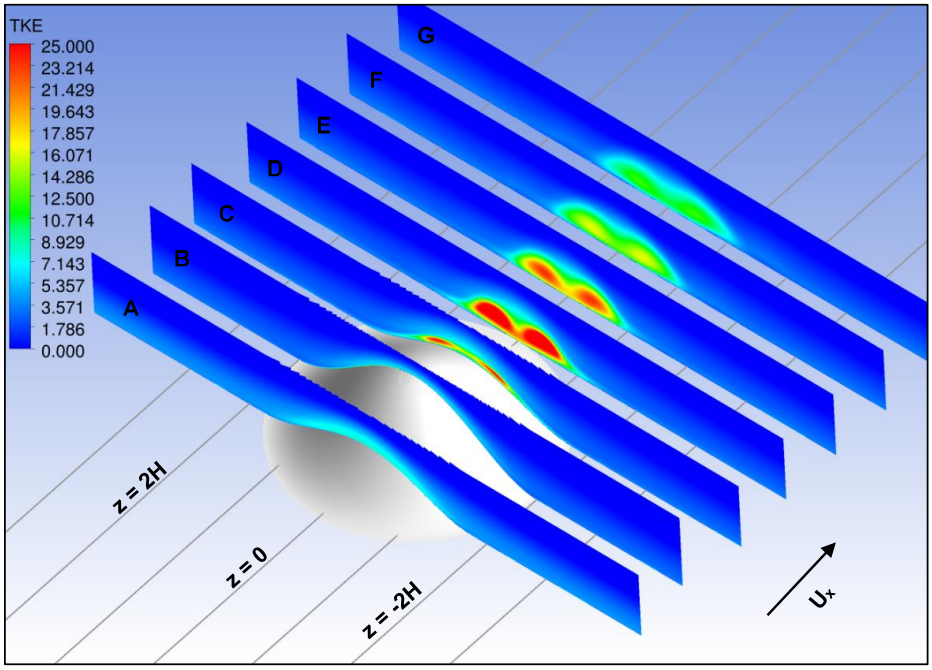

Figure 6.8 Predicted TKE contours for the k-k_L-ω-v^2 model at various planes in the flow direction corresponding to $x = -H$ (A), 0 (B), H (C), $2H$ (D), $3H$ (E), $4H$ (F), and $5H$ (G)

The spanwise variation of friction velocity normalized by the reference velocity (u_τ/U_o) at a location downstream of the hill ($x/H = 3.69$) is shown in Fig. 6.11. At this location, a turbulent boundary layer with flow reattached to the wall is observed. The strong downwash of the vortices observed on the lee side and downstream of the hill resulted in a peak value at the centerline ($z/H = 0.0$). The u_τ values computed from the k-k_L-ω-v^2 model data indicate smooth spanwise variation in contrast to the spatial variability observed in experimental data [107], as expected from any RANS simulation. Also, the k-k_L-ω-v^2 model underpredicts values when compared to the peak values in experiments. Resolving the grid resolution in the spanwise direction might provide better

results. Nevertheless, the k-k_L-ω-v^2 model indicates a maximum friction velocity value at the centerline accurately and the predictions are in qualitatively good agreement with those observed in the experiments.

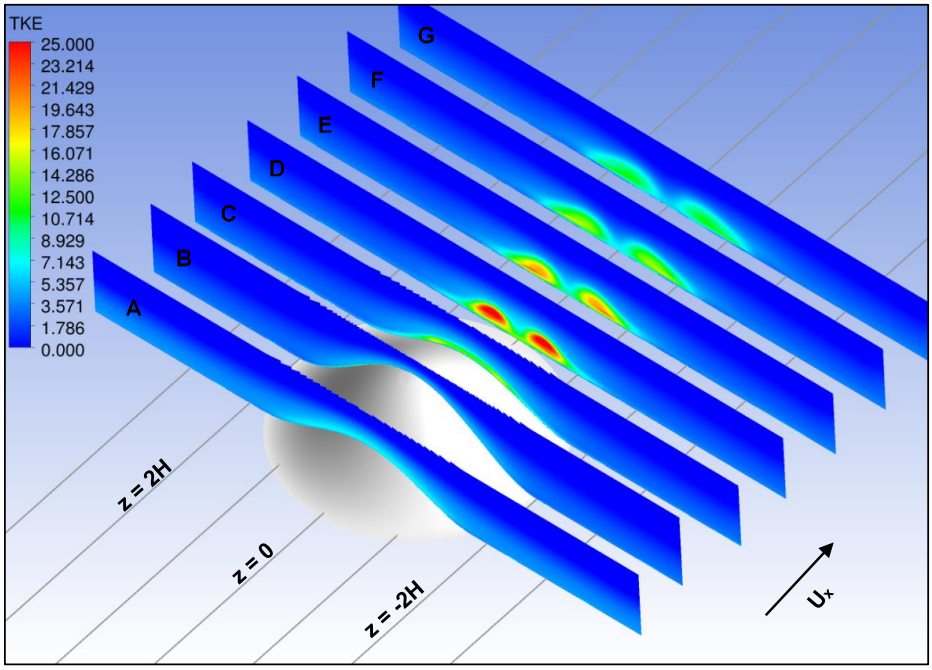

Figure 6.9 Predicted TKE contours for the k-k_L-ω model at various planes in the flow direction.

Here, the plane locations are as in Fig. 6.8

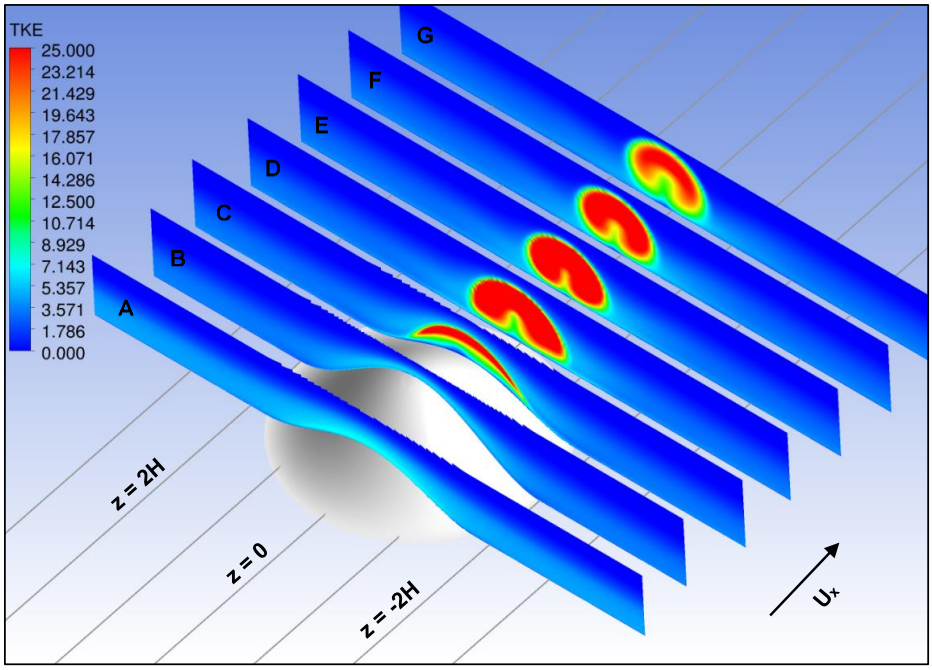

Figure 6.10 Predicted TKE contours for the SST k-ω model at various planes in the flow direction.

Here, the plane locations are as in Fig. 6.8

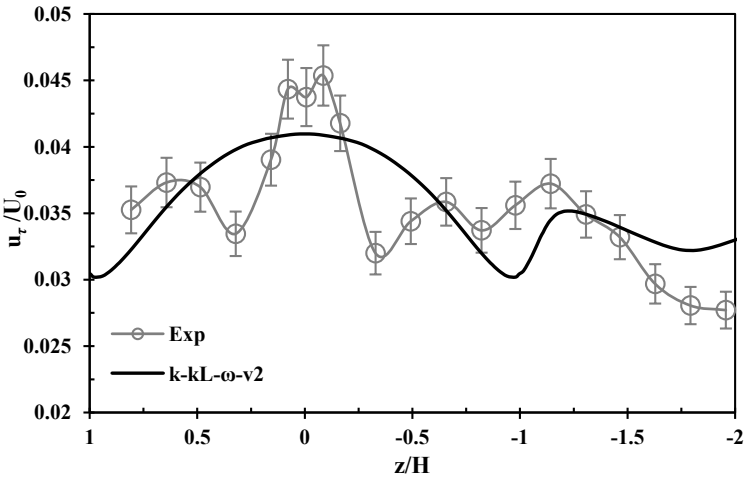

Figure 6.11 Spanwise variation of friction velocity (u_τ) predicted by the new model in comparison with experiments at $x/H = 3.69$.

Here, experimental uncertainty of ±5% is indicated with bars

Lastly, streamwise and spanwise velocity profiles normalized by the reference velocity along the wall-normal direction are presented in Figs. 6.12 and 6.13. These profiles are taken at the streamwise location of $x/H = 3.69$ (downstream of the hill), and at various locations on and either side of the symmetry plane ($z/H = 0.0$) corresponding to $z/H = 0.08$, 0.16, and 0.49. The new model predictions are slightly better than its parent model k-k_L-ω and in general, agree well with the experiments. Interesting to see are the results from the SST k-ω model which are consistently off from the experimental data. As illustrated earlier in Fig. 6.6 (d), the SST k-ω model predicts earlier and larger flow separation on the lee side of the hill, leading to the wrongful prediction of boundary layer velocity profiles in the vicinity of the hill. It is clear from all the velocity profiles shown below and TKE contours (see Figs. 6.8-6.10) that all the three RANS models predict a symmetric flow pattern on either sides of the center plane ($z/H = 0.0$), in contrast to the experimental predictions which indicate the flow to be only near to symmetric in nature. This difference in RANS model predictions and experimental observations are illustrated in the spanwise velocity profile at location $z/H = 0.49$. Except for this location, on the whole, the variations between k-k_L-ω-v^2 and k-k_L-ω models are small and predictions are satisfactory.

6.4 Conclusions

In this study, the canonical problem of turbulent boundary layer flow over a 3D axisymmetric hill was numerically investigated using three RANS models – transition and curvature-sensitive k-k_L-ω-v^2, transition-sensitive k-k_L-ω, and fully turbulent SST k-ω. Results obtained from the CFD simulations, in terms of surface pressure distribution, velocity distribution, turbulence characteristics, and flow patterns were compared to the

experimental data of Simpson et al. [106] and Byun et al. [107]. Fully turbulent SST k-ω model predictions have poor accuracy when compared to experiments in terms of mean flow statistics. The model predicted early flow separation from the hill surface, followed by a large recirculation region on the lee side. This resulted in poor predictions of pressure values on the lee side and in the wake region of the hill. The model failed to predict a CRVP and instead produced a single large vortex downstream of the hill. The transition-sensitive k-k_L-ω model predicted a delayed and tiny flow recirculation region on the lee side, with flow reattachment downstream near the foot of the hill. Due to the delayed separation point, the model predicted a single tiny vortex downstream of the hill. Pressure values were overpredicted on the windward and lee side of the hill, however better results were produced compared to SST k-ω. Results predicted by the k-k_L-ω-v^2 model matched the trends of the experiments very closely. Excellent results were produced by the model in terms of pressure distribution over the hill surface and velocity profiles in the wake region. The new model produced a pair of flow recirculation zones on the lee side of the hill accurately, which was followed by the formation of a CRVP. However, small discrepancies were observed in the prediction of the height of the recirculation region on the lee side, and peak pressure values on the windward side of the hill.

On the whole, results indicate the ability of the new model to successfully resolve the complex effects of flow transition and streamline curvature arising from the hill surface with reasonable engineering accuracy. Results also suggest that the model has potential as a practical tool and may be desirable for solving low/high Re flows over blunt/curved bodies for the prediction of flow transition and curvature effects. Future

research efforts will focus on investigating a dynamic hybrid RANS-LES modeling framework [80] which makes possible coupling of transition- and curvature-sensitive RANS models with arbitrary LES subgrid stress models. Specifically, the proposed four-equation RANS model will be coupled with the MILES scheme and the model's performance will be tested against the axisymmetric hill test case.

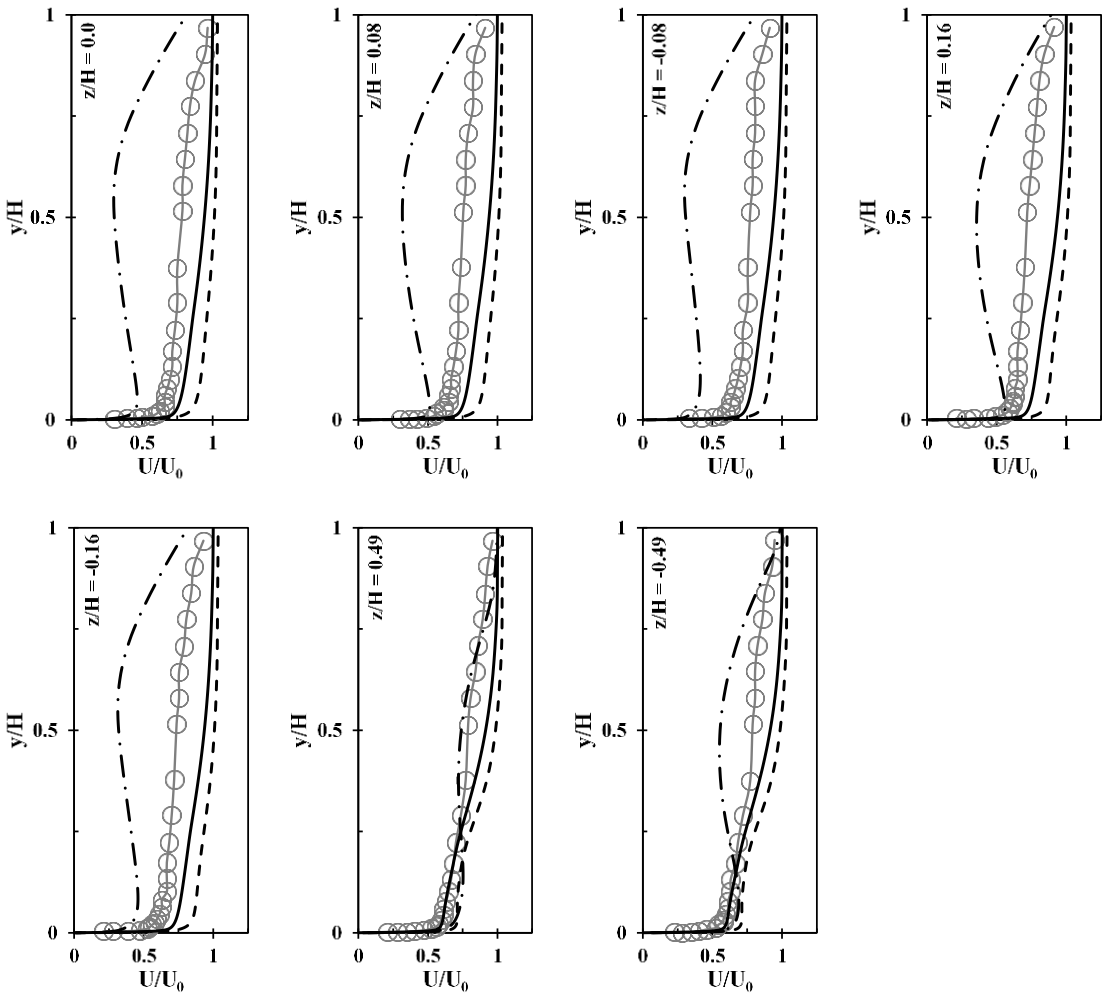

Figure 6.12 Normalized streamwise velocity profiles at various locations across the flow and at $x/H = 3.69$.

Here, experiments correspond to lines with symbols, k-k_L-ω-v^2 (——), k-k_L-ω (- - -), and SST k-ω (—·—·)

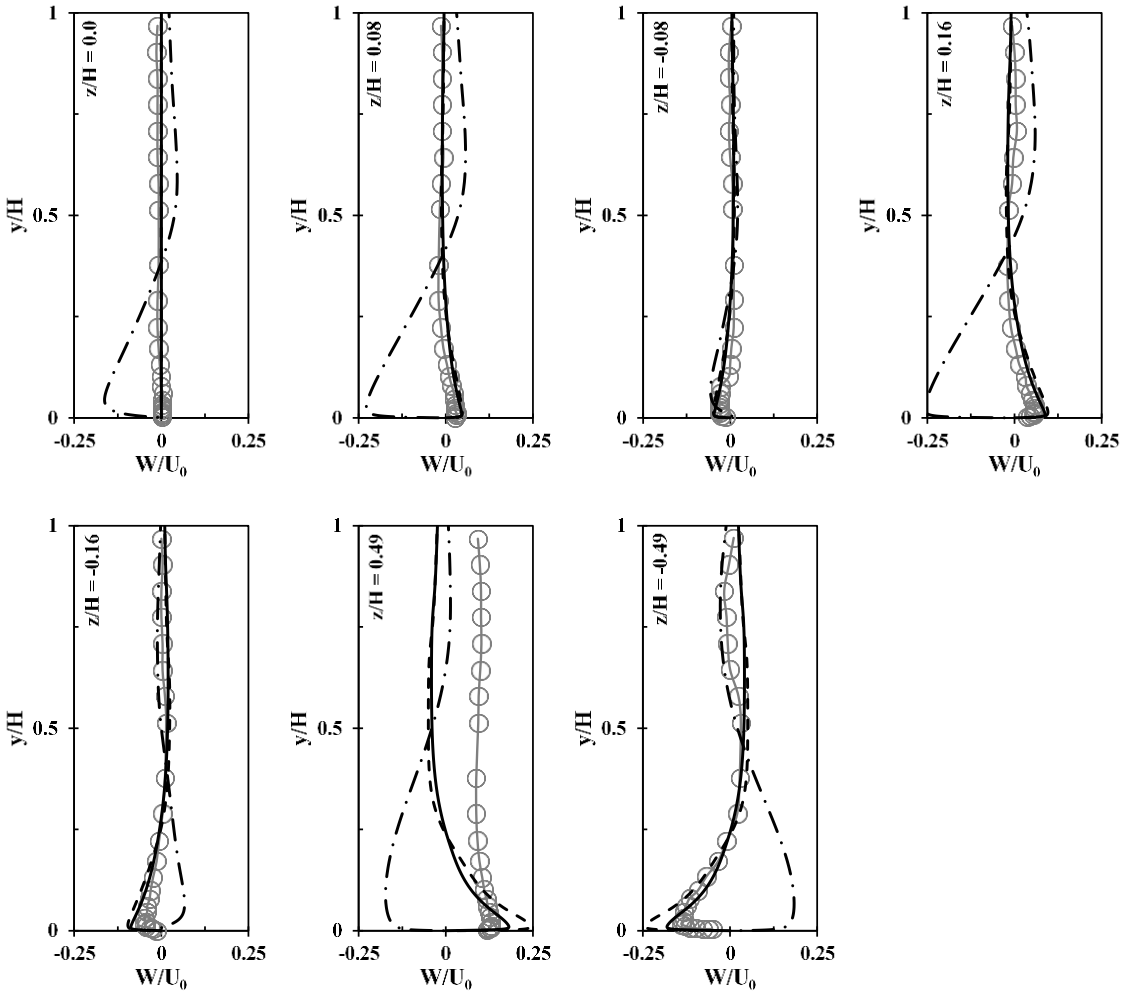

Figure 6.13 Normalized spanwise velocity profiles at various locations across the flow and at $x/H = 3.69$.

Here, experiments correspond to lines with symbols, k-k_L-ω-v^2 (——), k-k_L-ω (- - -), and SST k-ω (—·—·)

CHAPTER VII

A HYBRID RANS-LES MODELING METHODOLOGY SENSITIZD TO TRANSITIONAL AND CURVATURE/ROTATION EFFECTS

7.1 Introduction

This chapter presents a new hybrid model that seeks to combine the strengths of RANS and LES methods. The new model is based on a recently proposed version of a dynamic hybrid RANS-LES framework that addresses several deficiencies inherent in most current hybrid models, including explicit grid dependence, boundary layer model stress depletion, and delayed shear layer breakdown. The DHRL framework is highly generalized, allowing coupling of any desired LES model with any given RANS model. Here, the proposed four-equation EVM capable of predicting both T-RC effects is used for the RANS component, and the MILES scheme is used for the LES component. The new model (DHRL with T-RC effects) is implemented into a commercial CFD code and investigated against three different flow configurations. The test cases include nonrotating and rotating channel flow, ZPG boundary layer flow over a flat plate, and flow over a circular cylinder. Results obtained from the numerical simulations are compared with available results from experiments and with other class of turbulence modeling techniques, including EVMs, hybrid RANS-LES, and LES models.

7.2 Numerical Method

For all the DHRL model simulations, the SIMPLE scheme was used for pressure-velocity coupling, and gradients were computed using a Green-Gauss cell based method. The pressure discretization was changed to second order interpolation scheme [115] with linear reconstruction of pressure data from cell centers to cell faces. To minimize the effects of both dissipative and dispersive errors on the results, discretization of convective terms in all the equations was changed to bounded central differencing (BCD) scheme [116]. This change was required in the DHRL model simulations due to the strong dependency of MILES approach on the choice of numerical schemes used [117]. It was reported in Adedoyin et al. [118] that the use of MILES approach with the BCD scheme produced better results with less dissipation compared to the second order upwind or QUICK [119] schemes available in FLUENT solver. Hence, both channel flow and flat plate test cases utilized the BCD scheme for discretization of convective terms. However, for the cylinder test case, the use of BCD scheme resulted in increased dissipation leading to the wrongful prediction of turbulent flow by the LES component (MILES scheme) in regions upstream of the cylinder. Hence, discretization of convective terms were performed using the second order upwind scheme. This change was necessary for the DHRL model to accurately predict flow transition near the cylinder surface and in the wake region as well. Lastly, all unsteady terms for transient simulations were discretized using a second-order implicit (three-point backward difference) scheme.

For the DHRL model simulations, it was necessary to adopt a transient time method. For all unsteady simulations, a fixed time stepping method was used with the time step size for each case set to correspond to a convective CFL number of 1, based on

the freestream velocity and minimum streamwise cell size in the domain. Additional simulations were performed with CFL numbers of 0.5 and 2 to ensure time step size independence of the simulations. Based upon the time step study, a time step-size of 5e-05 T (for all cases), with a maximum of 20 iterations per time step, were found to be sufficient and were used for the respective results shown in this chapter. Here, T is the flow-over time, equal to the chord length divided by the freestream velocity ($T = c/U_\infty$). All test cases were run to full convergence, based on reduction of residuals at each time step of at least three orders of magnitude.

A grid sensitivity study was performed for all of the test cases by systematically refining the grid until the solution remained effectively unchanged between the coarser grids and their refined versions. Each refinement level represented an increase in cell count of approximately 60% or higher versus the next coarsest grid level. Based upon the above procedure, the results presented here were judged to be grid-independent for all cases. More details regarding grid independence study for each test case are given in the following sections.

For evaluating computational cost of the proposed DHRL model, simulations were performed on the nonrotating channel flow case using the DDES and DHRL models under identical conditions. The DDES employed the two-equation SST k-ω as RANS component and the DHRL employed the four-equation k-k_L-ω-v^2 as RANS component. The DHRL model requires approximately 9% more computation time per iteration than its counterpart DDES model. The DHRL model is expected to be slightly more expensive, since it solves 4 equations in RANS mode and also resolves additional complex effects of flow transition and rotation. However, given the improved accuracy in

results using the DHRL model, the marginal increase in computational cost is completely justifiable.

7.3 Test Case 1: Three-Dimensional Channel Flow

For the DHRL model validation case, we consider a fully developed pressure-driven turbulent flow in a nonrotating ($Ro = 0$) and rotating ($Ro = 0.5$) channel with Reynolds number (Re_τ) equal to 194, based on the wall friction velocity and channel half-height ($H/2$). The rotation number is defined as $Ro = \omega_m H/U_m$, where ω_m is the angular velocity of the reference frame relative to the inertial frame and U_m is the average velocity through the channel. Numerical results from the simulations were compared with the DNS data of Kristoffersen and Andersson [95]. The channel flow was modeled using a computational domain with a Cartesian grid size of 64 × 48 × 48 (streamwise × wall normal × spanwise) and with periodic boundary conditions applied in the streamwise and spanwise directions. The domain extended $2\pi\delta$ in the streamwise and $\pi\delta$ in the spanwise directions, where δ is the channel half-height. The generated grid had $y^+ \approx 1$ at the walls and cells near the centerline had aspect ratios near unity. The computational grid used for this test case is similar to the coarse grid reported in Walters et al. [90] and is shown in Fig. 7.1. A uniform pressure gradient was applied in the streamwise direction to obtain the desired friction velocity for both the nonrotating and rotating cases.

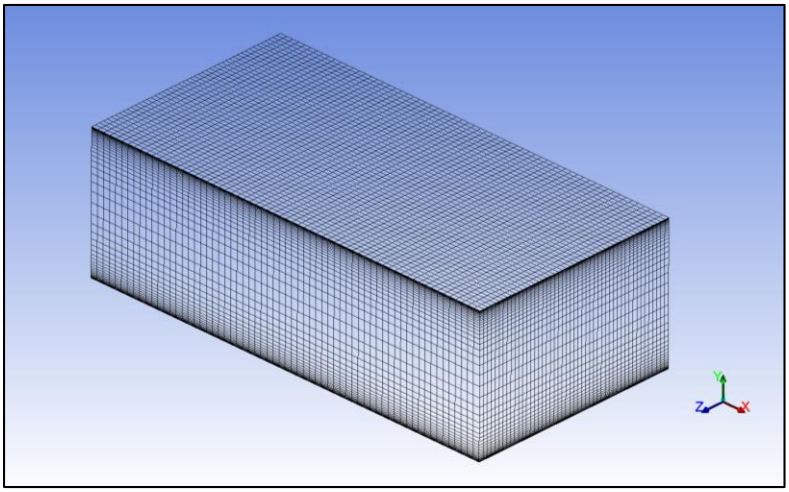

Figure 7.1 Mesh for the nonrotating and rotating channel flow test case

For the nonrotating case, all the three models tested – DHRL with T-RC effects, DDES (with SST k-ω as RANS component), and MILES – predicted the symmetric velocity profile accurately (see Fig. 7.2 (a)). Both DHRL and DDES models predicted the velocity profile without any log-layer mismatch and MILES results were slightly offset from the DNS predictions, which might be due to the use of a coarser grid (see Fig. 7.2 (b)). The well-known log-layer mismatch, generally observed in the hybrid models, is not seen in the DDES profile as the model produced steady state results, i.e., pure RANS results equivalent to the SST k-ω model with no resolved fluctuations. This behavior of the DDES model is illustrated in Figs. 7.3 (a) and 7.4 (a). It was also observed in an earlier study from our group [90] that the DDES model produced RANS type results for wall bounded flows in the low Re regime. In contrast, the DHRL model produced significant levels of resolved fluctuations (see Figs. 7.3 (b) and 7.4 (b)). This result is significant, since for low Re flows, the DHRL model resolves more scales of motion

compared to a RANS type result (in this case the DDES model) and comparatively lesser scales than the MILES approach (see Figs. 7.3 (c) and 7.4 (c)).

The highlight of the new model lies in its ability to accurately capture the flow rotation effects, as observed in Figs. 7.5 and 7.6. The velocity profiles in Fig 7.5 are normalized by the average channel velocity, and total resolved shear stress profiles in Fig. 7.6 are normalized by the square of the average wall friction velocity. The characteristic asymmetry caused by the imposed rotation in the velocity profile is correctly predicted by the new model. In the presence of high system rotation rates, such as the $Ro = 0.5$ case, turbulence is suppressed and flow relaminarization is observed on the stable side of the channel, and turbulence is enhanced on the unstable side of the channel. In this scenario, RANS results are produced on the stable side and LES results are produced on the unstable side of the channel. This phenomenon is clearly illustrated in Fig. 7.7, wherein the profiles of LES weighting coefficient α are shown. One more significant result obtained using the DHRL model is for the nonrotating case, wherein the model stays in a transitional mode, i.e., the value of α lies between 0 and 1 in the entire channel domain. Here, an additional RANS stress compensates for the reduced LES content, thereby leading to a smooth variation of turbulent production across the region. It must be noted that the value of α depends on the local flow physics rather than any grid-based metric.

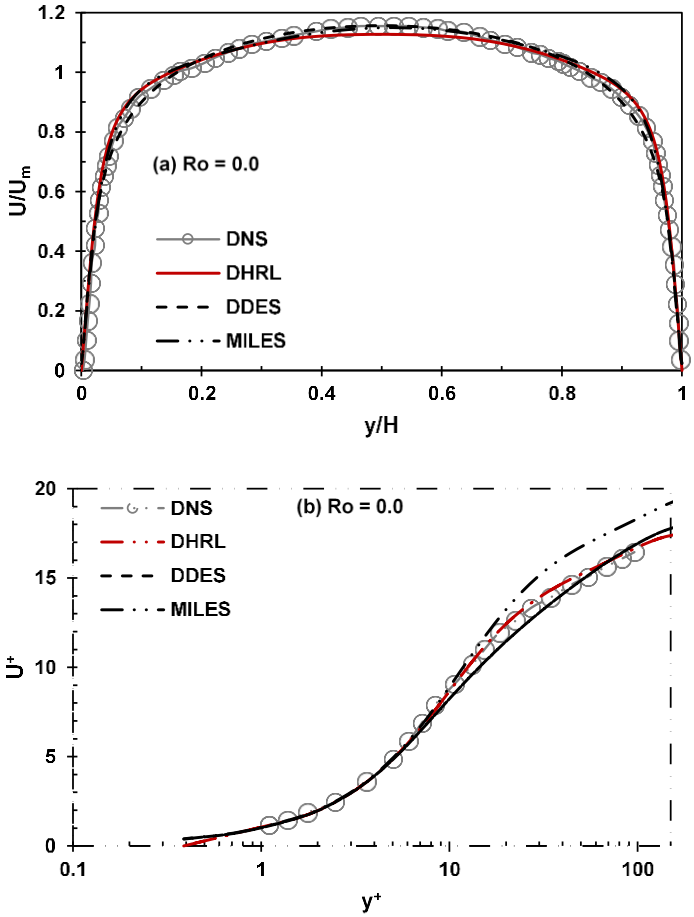

Figure 7.2 Mean velocity profiles for nonrotating (*Ro* = 0.0) channel flow case comparing present predictions with DNS data in: (a) global coordinates and (b) wall coordinates

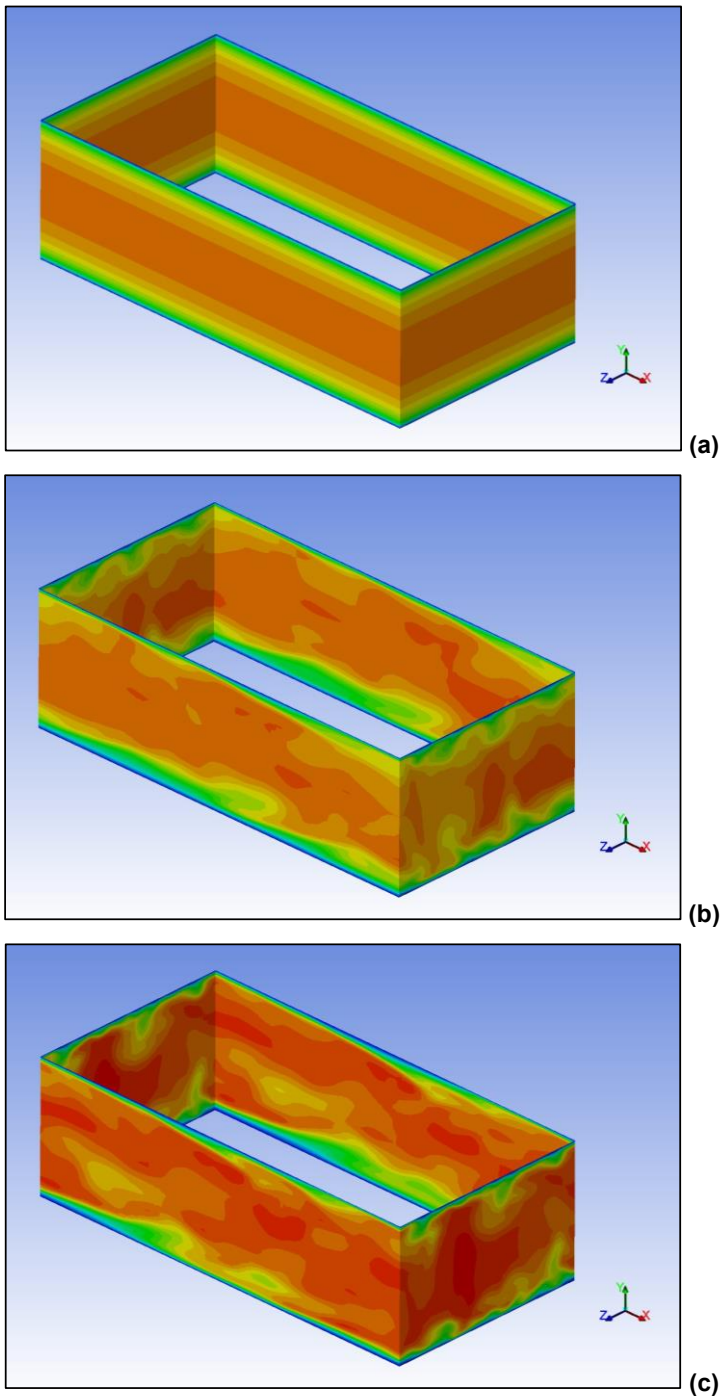

Figure 7.3 Instantaneous x-velocity contours for nonrotating (Ro = 0.0) channel flow case: (a) DDES model, (b) DHRL model, and (c) MILES scheme

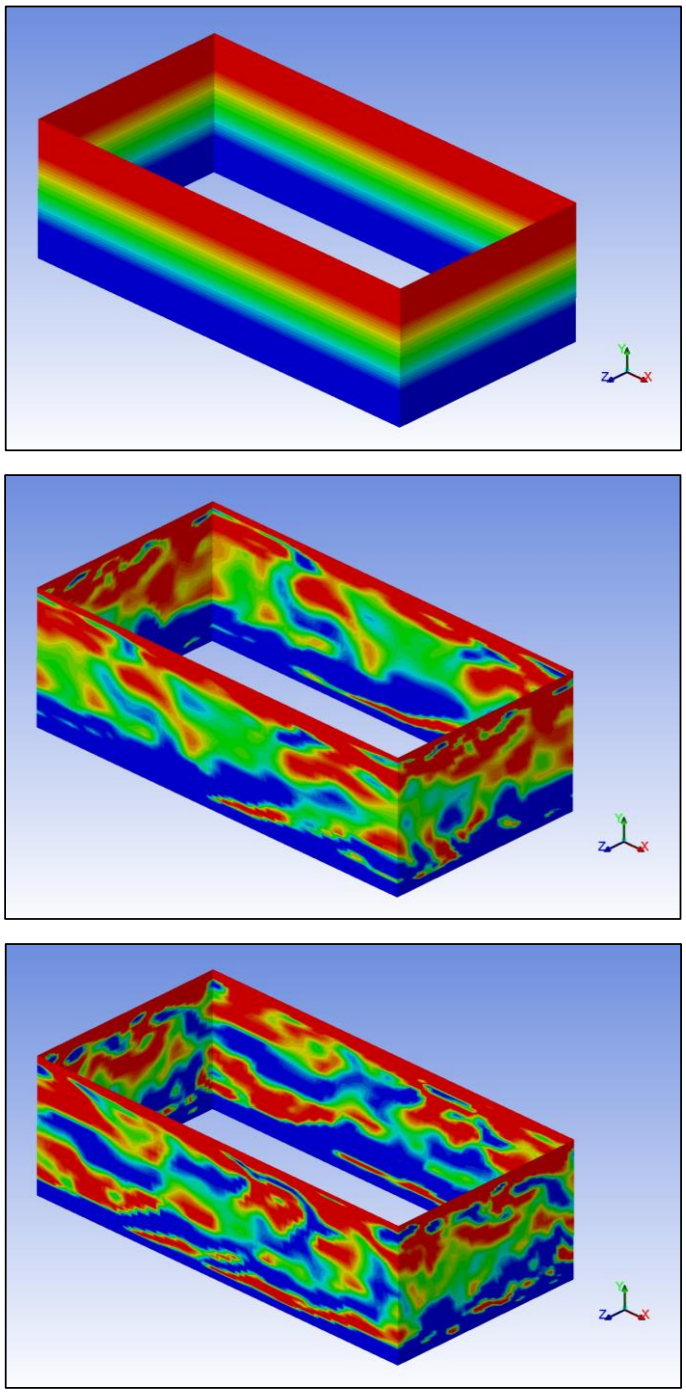

Figure 7.4 Instantaneous z-vorticity contours for nonrotating (Ro = 0.0) channel flow case: (a) DDES model, (b) DHRL model, and (c) MILES scheme

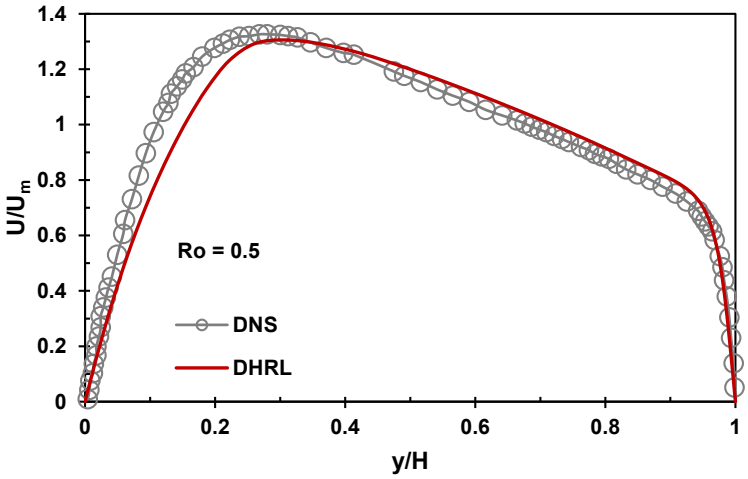

Figure 7.5 Mean velocity profiles for rotating (*Ro* = 0.5) channel flow case comparing DHRL model predictions with DNS data

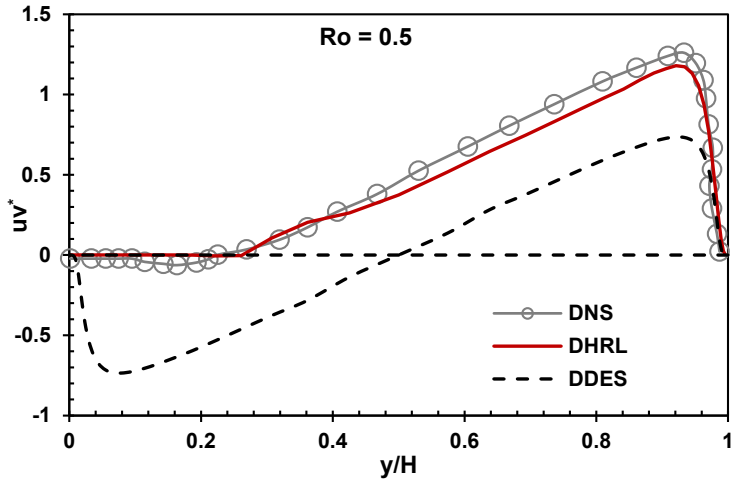

Figure 7.6 Total resolved shear stress profiles for rotating (*Ro* = 0.5) channel flow case

Overall, the channel flow results presented here indicate that the DHRL model yields an appropriate response to flows with and without any rotational effects accurately and produces results in close agreement with the DNS data. More importantly, the model

is capable of producing turbulent fluctuations in attached boundary layer flows, even in the low Re regime, provided the mesh is sufficiently refined.

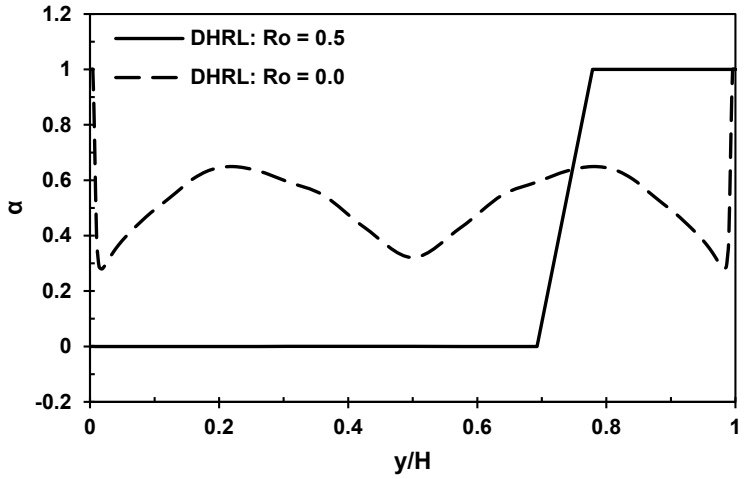

Figure 7.7 LES weighting parameter (α) distribution in nonrotating (Ro = 0.0) and rotating (Ro = 0.5) channel flow case for DHRL model

7.4 Test Case 2: Three-Dimensional Flat Plate T3 Cases

The 3D ZPG flat plate cases considered here match the test cases assembled by ERCOFTAC [96] and Savill [23]. The boundary conditions and grid for the three test cases – T3A-, T3A, and T3B are similar to the ones reported in Chitta et al. [76], however, a 3D flat plate is considered in this study with a spanwise domain size $\Lambda_z = 0.1 \times L$, where L is the length of the plate. We have used periodic boundaries in the spanwise direction. To check the ability of the DHRL model to produce RANS type results on coarser grids, all the flat plate simulations were performed on a coarse mesh with a total of 1,223,200 cells, and the same grid was used for all the three test cases. The mesh was generated with grid points clustered near the wall and near the plate LE regions. The y^+

values for the first grid point away from the wall were maintained less than one over the entire plate, and grid independence was verified using the procedure outlined above. A more refined structured grid with a total of 5,768,520 cells was used for the grid sensitivity tests. The mean skin-friction coefficient (C_f) profiles obtained from the T3B test case using coarse and fine grids is shown in Fig. 7.8. No significant differences were observed in the results from the coarse vs fine grid, hence it was assumed that the CFD simulations were grid independent. It must be noted that, even with the use of a finer grid, the DHRL model was in the RANS mode in most part of the computational domain and similar results were produced for both coarse and fine grids. This was expected since the grid was never fine enough to resolve the large eddies and building a finer grid in order to produce LES results for the flat plate domain is expensive. Nevertheless, the results shown below indicate that the DHRL model produces a true RANS type solution on coarser grids.

Figure 7.9 shows the decay of freestream turbulence intensity (Tu_∞) predicted by the DHRL and DDES models in comparison with experiments for T3A and T3B test cases, indicating that the specified inlet boundary conditions were accurate. The predicted mean skin-friction coefficients (C_f) were compared with the experimental data in Fig. 7.10. The DHRL model sensitive to flow transition effects produced a laminar boundary layer at the start of the plate, eventually leading to flow transition to a turbulent boundary layer downstream of the plate. Note that the DHRL model is in the RANS state due to the use of a coarse grid and the predictions matched the results as reported in Chitta et al. [76]. In contrast, the DDES model produced a turbulent boundary layer from the start of the plate LE. This is due to the use of a fully turbulent SST k-ω model that does not

possess the ability to resolve the flow transition effects in the RANS component of the DDES model. The predicted streamwise mean velocity profiles are compared with the experimental data at various locations on the plate which lie in the pretransitional (Fig. 7.11 (a)), transitional (Fig. 7.11 (b, c)), and post-transitional, i.e., turbulent (Fig. 7.11 (d)) regions. Results predicted by the DHRL model agreed well with the experiments.

The conclusion from this test case signifies the fact that in the use of a coarser grid, the DHRL model produces a RANS type result, and the accuracy of the DHRL model, in this case depends greatly on the RANS model used.

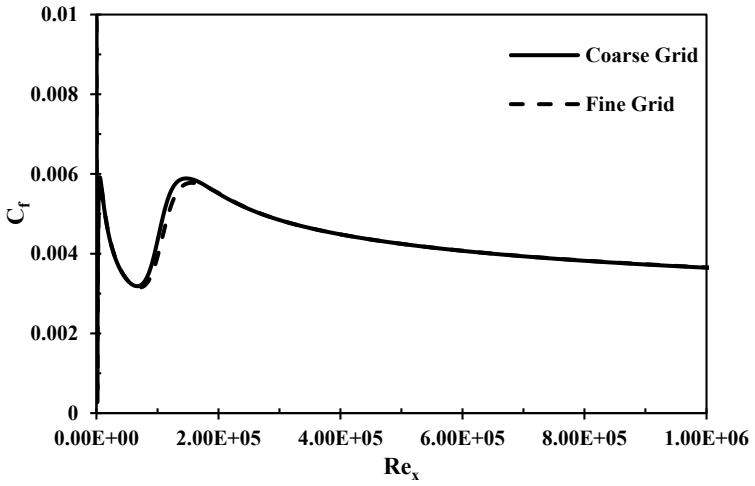

Figure 7.8 Example grid sensitivity study for the DHRL model on a T3B flat plate case

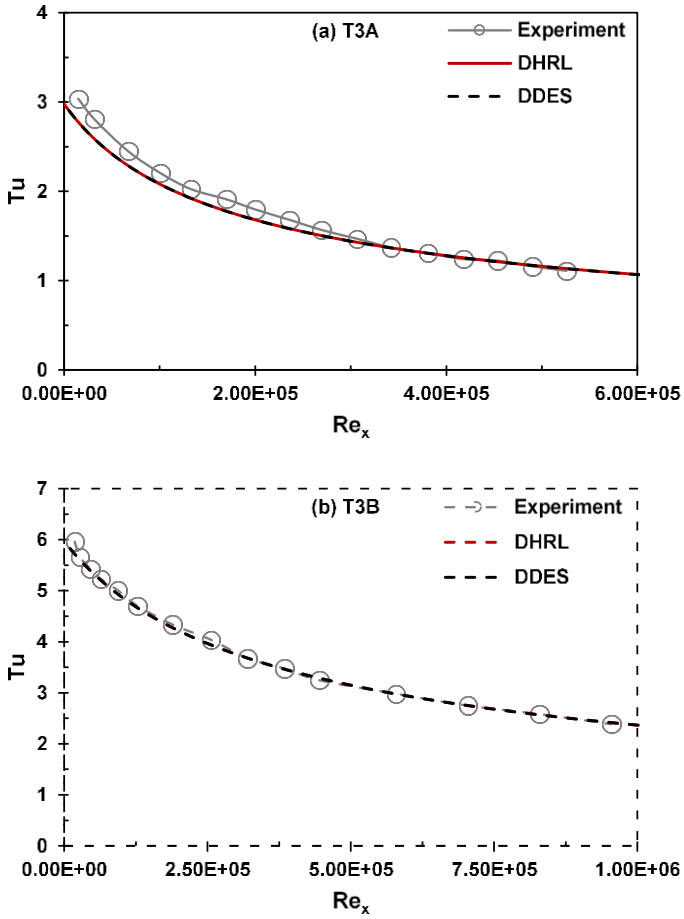

Figure 7.9 Streamwise decay of freestream turbulence intensity in comparison with experimental data for flat plate cases: (a) T3A and (b) T3B

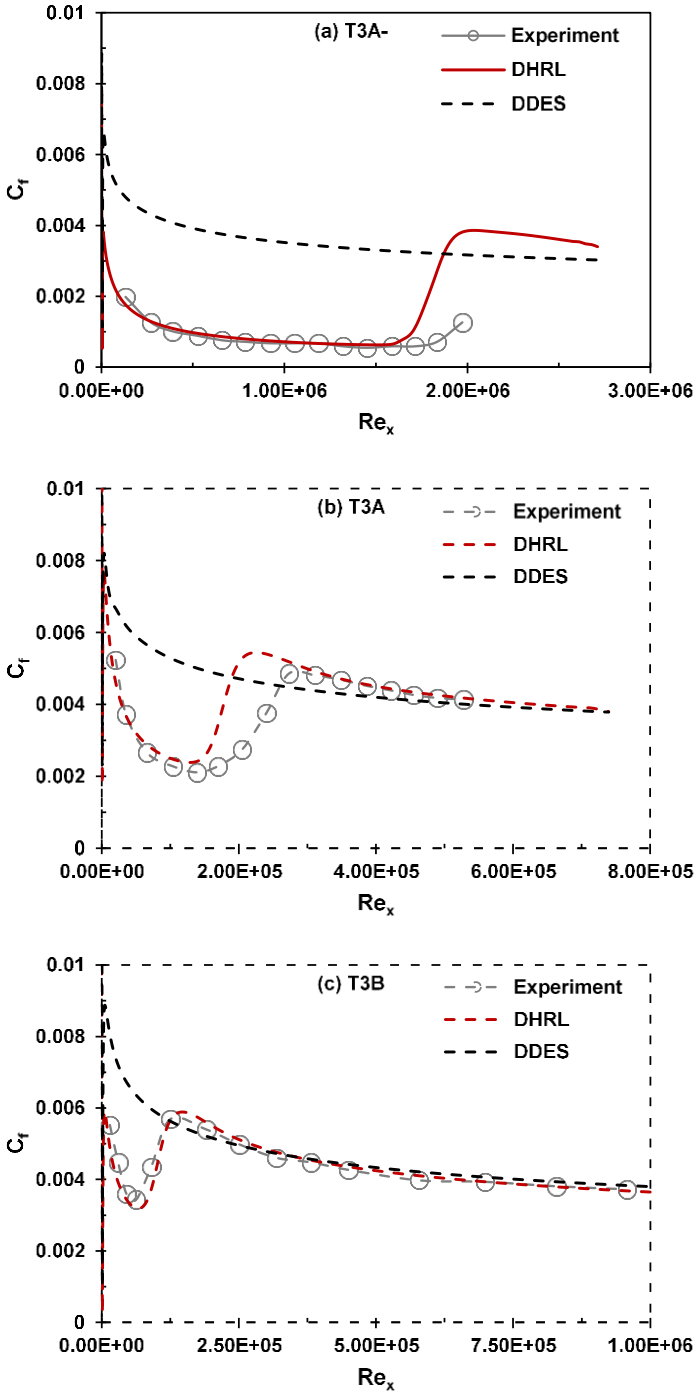

Figure 7.10 Streamwise distribution of mean skin friction coefficient for each of the three flat plate cases: (a) T3A-, (b) T3A, and (c) T3B

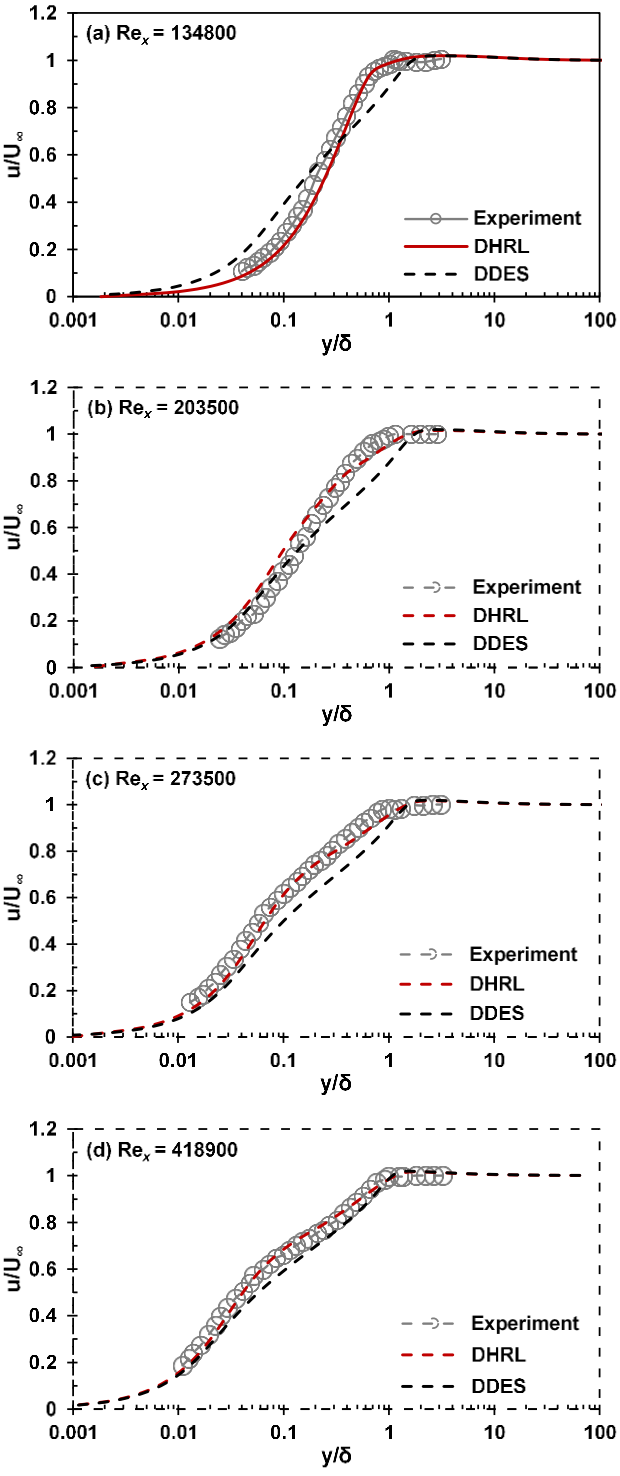

Figure 7.11 Normalized mean streamwise velocity profiles for T3A case at various locations on the plate: (a) Re_x = 134800, (b) Re_x = 203500, (c) Re_x = 273500, and (d) Re_x = 418900

7.5 Test Case 3: Three-Dimensional Circular Cylinder

As a final test case in this study, we consider the flow past a 3D circular cylinder with a flow Reynolds number based on the cylinder diameter, Re_D, ranging from subcritical to supercritical ($10^4 \leq Re_D \leq 10^7$) flow regime. The circular cylinder is an extensively studied test case both experimentally and computationally for the verification and validation of turbulence models. Although simple in terms of geometry, the flow behavior past a cylinder is quite complex to predict as it varies significantly depending on a variety of factors, including flow Reynolds number, aspect ratio and surface roughness of cylinder, Mach number, and freestream turbulence levels. Interested readers can refer to Refs. [97-99] for additional discussion on experimental and computational studies carried out in the past.

A test case similar to the one presented here was earlier studied by the current author for the verification and validation of the four-equation RANS model [76,77]. Although a 2D circular cylinder was used in that study, the results obtained by modeling both the flow transition and surface curvature effects using a single turbulence model showed significant improvement in flow predictions when compared to fully turbulent models. This can be attributed to the four-equation model's ability to capture both transitional and RC effects which are more pronounced in the lower Re cases accurately. It was also noted that, at higher flow Re conditions ($> 10^6$), the model was unsuccessful in accurately predicting the drag crisis region and flow separation angles. At such Reynolds numbers, significant large-scale unsteady flow structures are observed in the separated shear layer and in the wake region of cylinder, which in general are not well predicted by the RANS models, a known fact. Furthermore, for a surface with constant

radius of curvature, the effect on the boundary layer development will be less pronounced as the Re increases and the boundary layer thickness becomes smaller. For example, in the case of flow at $Re_D = 10^4$, the ratio of boundary thickness to cylinder radius is relatively high, and curvature effects are expected to play a more significant role than, say, the case of $Re_D = 10^7$. Nevertheless, it was encouraging to see the improved accuracy in results using the four-equation model in the subcritical flow regime.

In the present study we focus on the behavior of the DHRL model sensitized to T-RC effects in the subcritical to supercritical flow regimes. The hybrid model is expected to capture the flow transition and surface curvature effects prevalent in the subcritical flow regime, and also provide more detailed flow physics in high Re flows due to its ability to mimic a LES type simulation in the separated shear layers. For comparison purposes, simulations were performed using the new hybrid model along with four other models – MILES, DDES, fully turbulent SST k-ω, and transition and curvature sensitive k-k_L-ω-v^2. Also, results obtained from the numerical simulations were compared to available experimental data.

For all cases, the circular cylinder was placed in an O-type computational domain with the farfield boundaries stretching upto 10 diameters from the center of cylinder. The upstream and downstream boundaries were specified as velocity inlet and pressure outlet, respectively. In this study, a spanwise domain size $\Lambda_z = 2 \times D$, where D is the diameter of the cylinder was considered, and we have used periodic boundaries in the spanwise direction. In the literature, numerical studies for similar test cases have considered a spanwise domain size ranging from $1 \times D$ to $\pi \times D$ [120-122] with acceptable differences reported. A high quality, multiblock fully structured grid was generated for all the cases

with a $y^+ < 1$ for the first grid point placed next to the cylinder wall. The baseline mesh sizes generated for each case are reported in Table 7.1. All the meshes consisted of 40 cells in the spanwise direction. The computational domain and mesh generated for the $Re_D = 1 \times 10^4$ case is shown in Fig. 7.12. Extensive grid independency tests and sensitivity of the results to the domain size have been performed and based on the results obtained, all the grids used in this study are judged to yield mesh independent solutions. The grid sensitivity study was performed by systematically refining the grid until the solution remained effectively unchanged between the grids shown in this study (baseline) and their refined versions (fine grid). Each refinement level represented an increase in cell count of approximately 60% versus the next coarsest grid level. The 3D circular cylinder had a unit diameter and flow Re_D was varied from 10^4 to 10^7 by changing the dynamic viscosity (μ) of the fluid, while holding all other quantities as constant. The inlet boundary conditions for the test case were defined with an air velocity of 20 m/s, turbulence intensity of 0.2%, and a turbulent length scale of 0.1 times the diameter of the cylinder.

In the subcritical regime ($Re_D = 10^4$ and 10^5), boundary layer over the entire cylinder surface is laminar and flow transition from laminar-to-turbulent is observed downstream of the cylinder in the wake region. Also, flow separation from the cylinder surface occurs upstream of 90 deg. This flow behavior is illustrated in Figs. 7.13-7.14, which show the mean and instantaneous velocity contours for the circular cylinder at $Re_D = 10^4$ obtained using all the turbulence models tested in this study. Interesting to see is the DHRL models capability to produce significant resolved fluctuations in the separated flow region even at such low Reynolds numbers. Since the flow stays in the laminar

regime all over the cylinder surface and in most part of the wake region, predictions from all the models in terms of pressure coefficient profiles (see Fig. 7.15) and drag coefficient (C_D) values (see Table 7.2) match the trends of the experiments.

Table 7.1 Mesh size for each cylinder test case

Re_D	Mesh size
1×10^4, 1×10^5	1,162,880
1×10^6	1,731,680
1×10^7	4,988,480

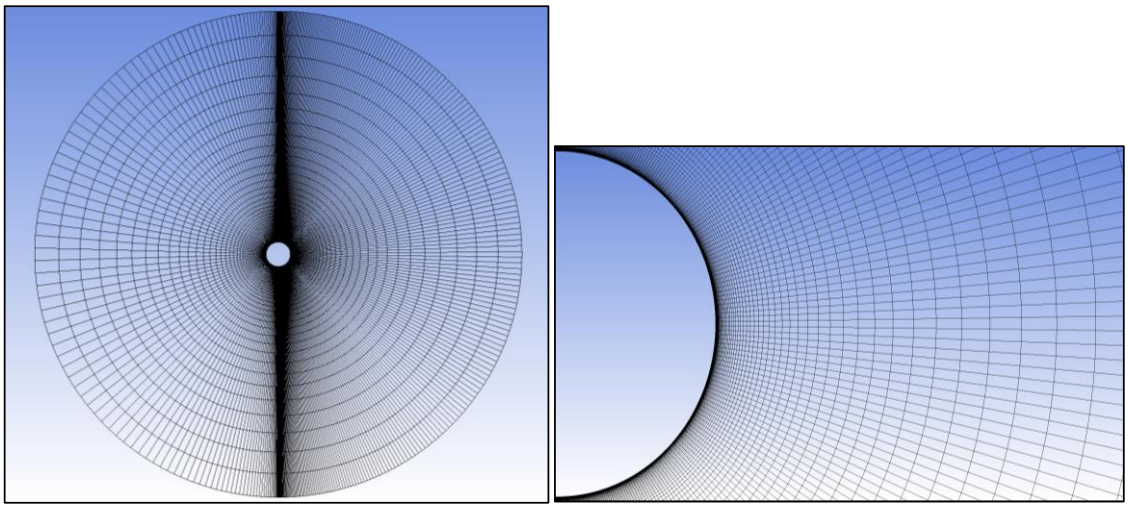

Figure 7.12 Computational domain and close-up of mesh near the wake region of cylinder for flow $Re_D = 1 \times 10^4$.

A similar domain with higher mesh density was used for higher flow Reynolds numbers

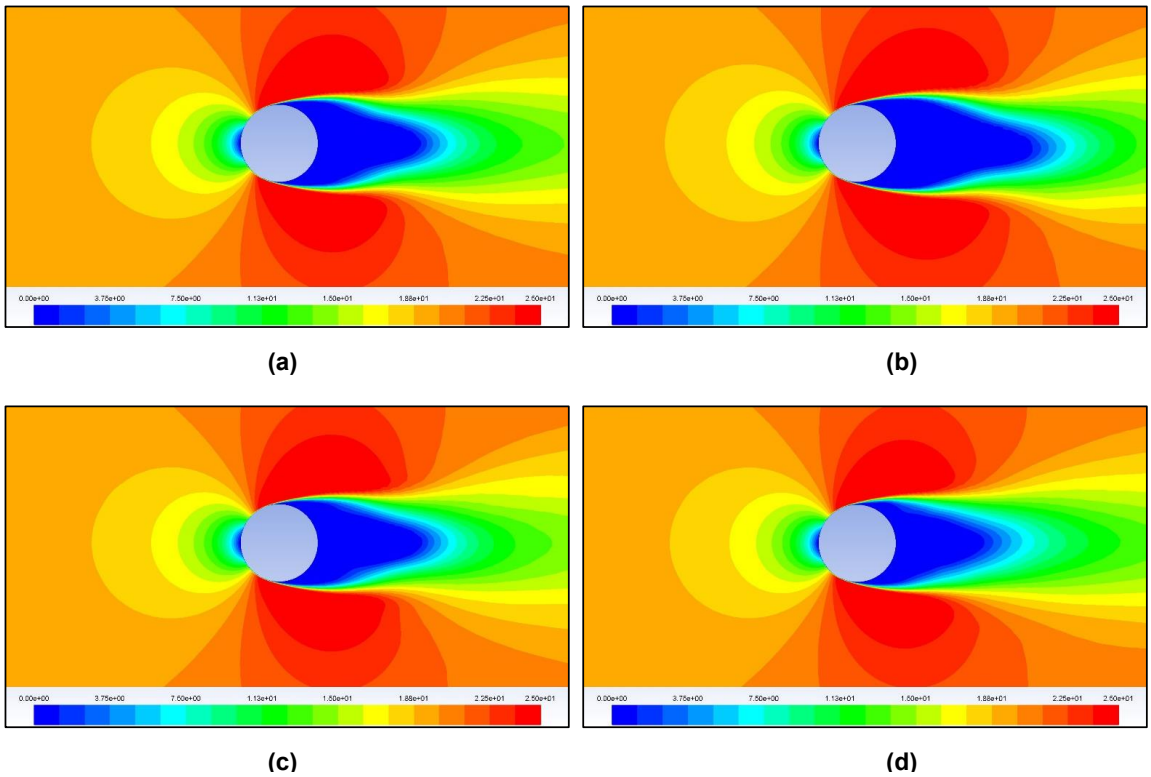

Figure 7.13 Mean x-velocity contours of circular cylinder at $Re_D = 1 \times 10^4$ for: (a) SST k-ω, (b) k-k_L-ω-v^2, (c) DDES, and (d) DHRL

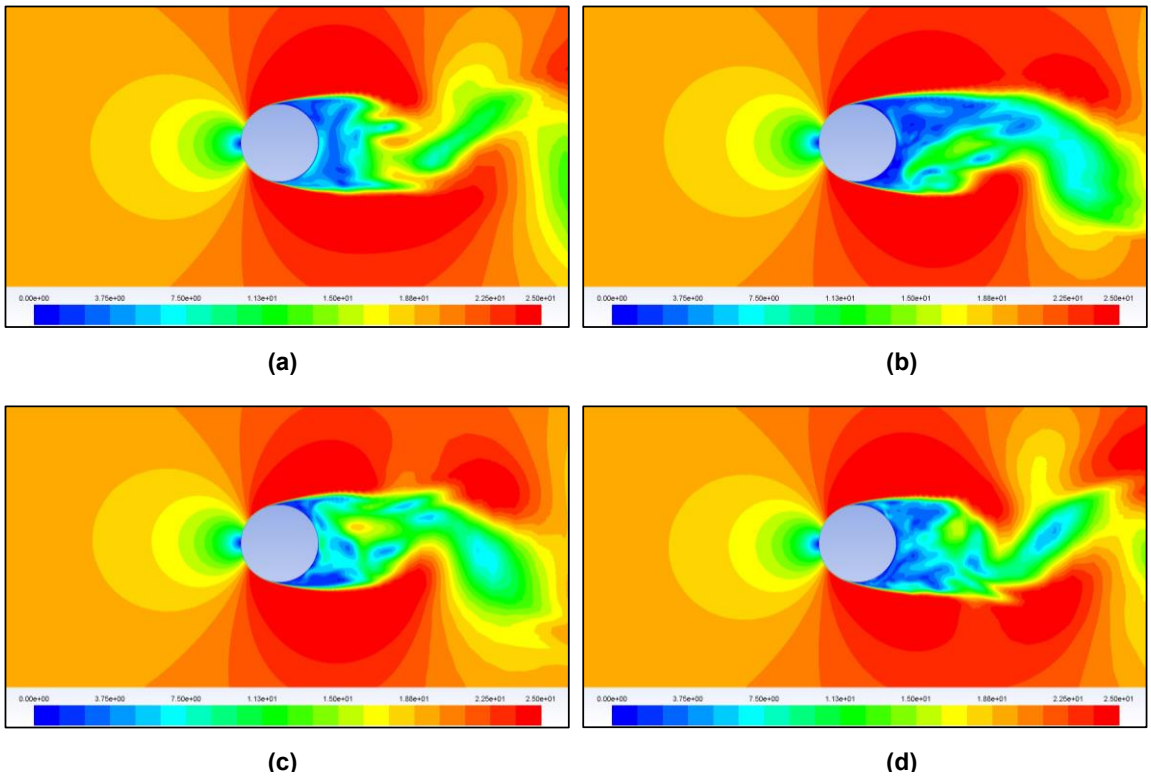

Figure 7.14 Instantaneous velocity contours of circular cylinder at $Re_D = 1 \times 10^4$ for: (a) SST k-ω, (b) k-k_L-ω-v^2, (c) DDES, and (d) DHRL

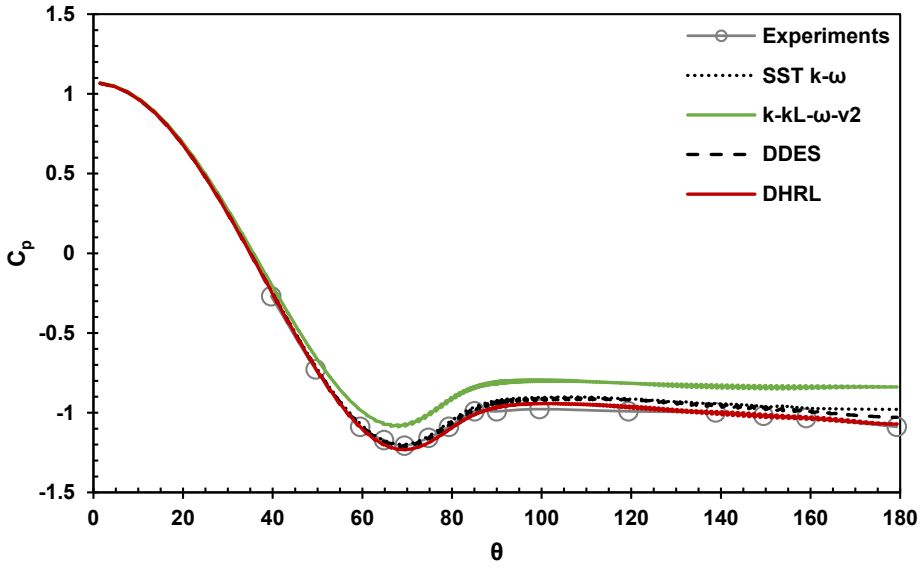

Figure 7.15 Time-averaged pressure coefficient distribution along the top of the cylinder at $Re_D = 1 \times 10^4$ in comparison with experiments by Roshko (1954) at $Re_D = 14500$

The $Re_D = 1 \times 10^5$ test case reveals the predictive differences between a hybrid and RANS model solution, and between the fully turbulent DDES and transition and curvature sensitive DHRL models. For this case, the flow again stays in the laminar regime over the surface of cylinder and flow separation is observed just downstream of 90 deg. The separated flow transitions to turbulence in the wake region close to the cylinder surface. Both DHRL and k-k_L-ω-v^2 models predict this flow phenomena accurately due to their sensitivity to flow transition effects, and both the DDES and SST k-ω models predict a fully turbulent boundary layer all over the cylinder surface (see Fig. 7.16). The turbulent fluctuations in the separated flow region next to the cylinder surface were captured by both the hybrid models DDES and DHRL, while both the RANS models show little fluctuations in their solutions (see Fig. 7.17), as expected. The C_p

profiles over the cylinder wall in comparison with experimental data of Cantwell and Coles [123] are shown in Fig. 7.18, and C_D values for all the turbulence models in comparison with data from Schlichting and Klaus [39] are shown in Table 7.2. DHRL predictions match very well with the experiments and differences between both the hybrid model solutions can be attributed to the DHRL model's ability to resolve curvature effects arising from the cylinder surface, flow transition from laminar-to-turbulent, and the large-scale structures observed in the wake region of cylinder accurately. The inability of the DDES model to resolve the transition and curvature effects resulted in discrepancies in the C_p profile for the downstream half of cylinder. Similar trend of results were observed in the C_D values as well. Also interesting to note is the comparison of results obtained from the DHRL and k-k_L-ω-v^2 models. The C_p profiles from both the models matched upto $\theta \approx 110$ deg and after which the k-k_L-ω-v^2 model overpredicts the pressure values. This is due to the model's inability to resolve the large-scale structures observed in the separated flow region. However, the four-equation model results are clearly superior to the hybrid model DDES and the SST k-ω model. These results provide confidence in satisfying the overall goal of the current research: to present two advanced turbulence modeling techniques to the CFD community with potential as practical tools, one under the hybrid modeling approach and the other under the RANS modeling approach, thereby enabling the end user to select either of the techniques according to the application of interest and availability of computational resources.

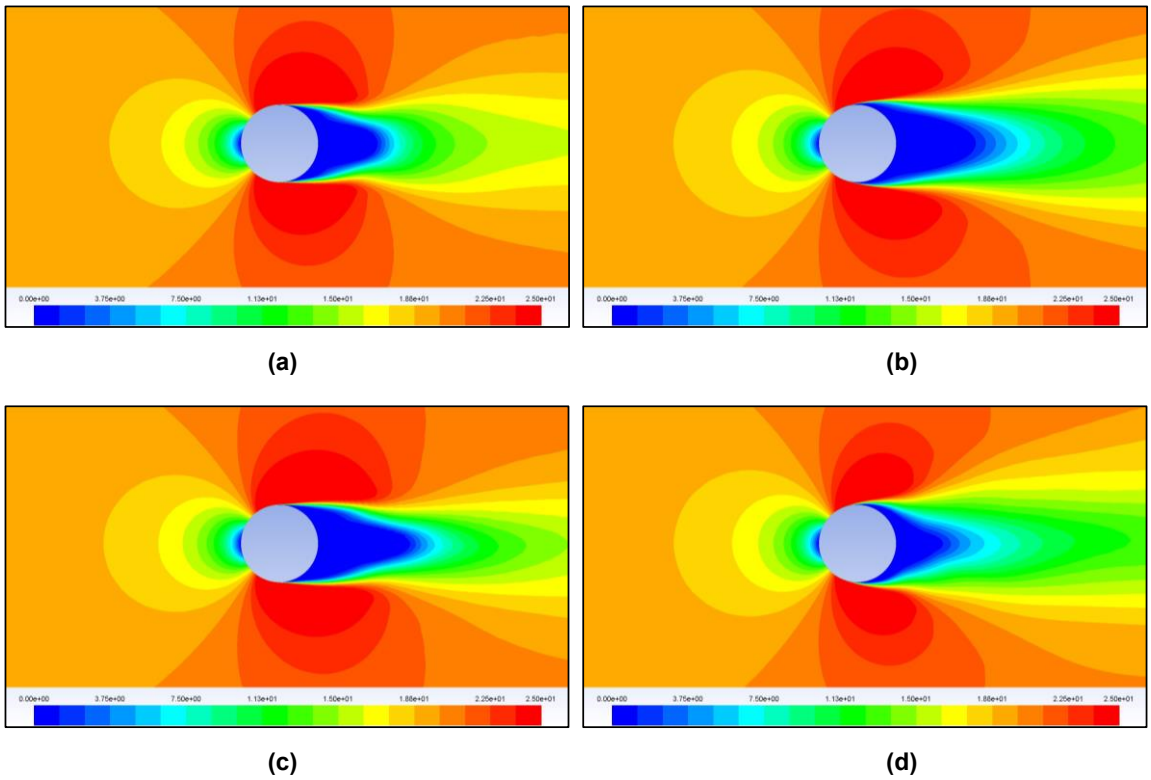

Figure 7.16 Mean x-velocity contours of circular cylinder at $Re_D = 1 \times 10^5$ for: (a) SST k-ω, (b) k-k_L-ω-v^2, (c) DDES, and (d) DHRL

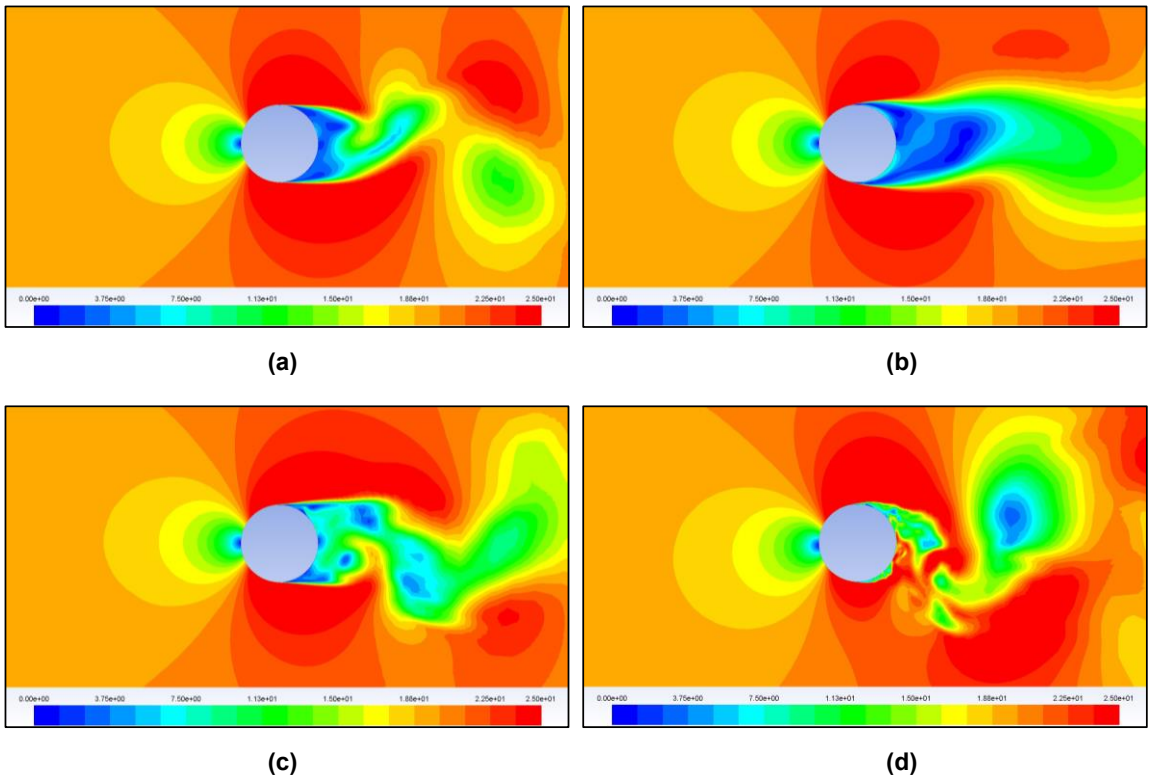

Figure 7.17 Instantaneous velocity contours of circular cylinder at $Re_D = 1 \times 10^5$ for: (a) SST k-ω, (b) k-k_L-ω-v^2, (c) DDES, and (d) DHRL

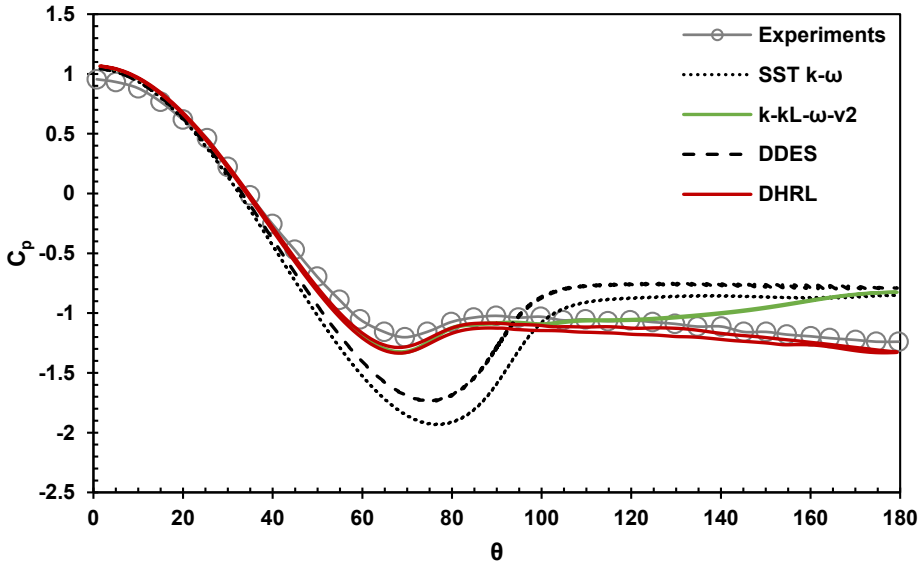

Figure 7.18 Time-averaged pressure coefficient distribution along the top of the cylinder at $Re_D = 1 \times 10^5$ in comparison with experiments by Cantwell and Coles [123] at $Re_D = 1.4 \times 10^5$

The remaining two cases are in the critical ($Re_D = 10^6$) and supercritical regimes ($Re_D = 10^7$). In the critical regime, flow transition takes place on the cylinder surface leading to the formation of a LSB, and the reattached turbulent boundary layer separates at a location farther downstream on the cylinder surface. Again both DHRL and k-k_L-ω-v^2 models predict this flow behavior accurately (see Fig. 7.19). In the supercritical regime, an attached boundary layer transition is predicted by both the DHRL and k-k_L-ω-v^2 models upstream of 90 deg, followed by turbulent flow separation downstream on the cylinder surface. The turbulent wake region predicted by all the models is observed from the mean velocity contours shown in Fig. 7.21. The instantaneous velocity contours for both these flow regimes clearly indicate that the DHRL model produces significant LES content in the wake region of cylinder (see Figs. 7.20 and 7.22). Strangely, the DDES

model produced little unsteadiness far from the wall in the case of $Re_D = 10^6$ and RANS-like behavior in the case of $Re_D = 10^7$. This is also evident from the C_p profiles and C_D values where the DDES results are closer to the SST k-ω results. Note that in Fig. 7.23, all simulation results are compared to experiments by Warschauer and Leene [124] at $Re_D = 1.2 \times 10^6$ and Achenbach [100] at $Re_D = 3.6 \times 10^6$, and in Fig. 7.24, experiments by Roshko [98] at $Re_D = 8.4 \times 10^6$. Nevertheless, C_p profiles from the DHRL model match closely and follow the trends of the experiments.

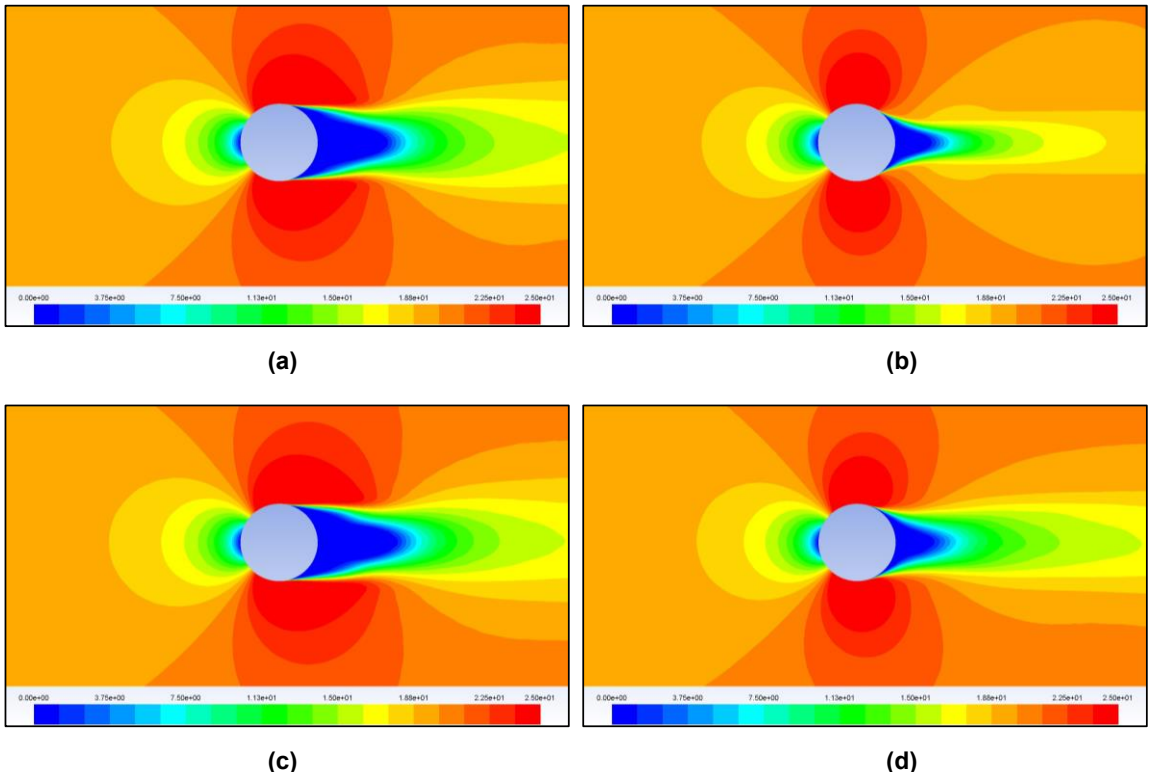

Figure 7.19 Mean x-velocity contours of circular cylinder at $Re_D = 1 \times 10^6$ for: (a) SST k-ω, (b) k-k_L-ω-v^2, (c) DDES, and (d) DHRL

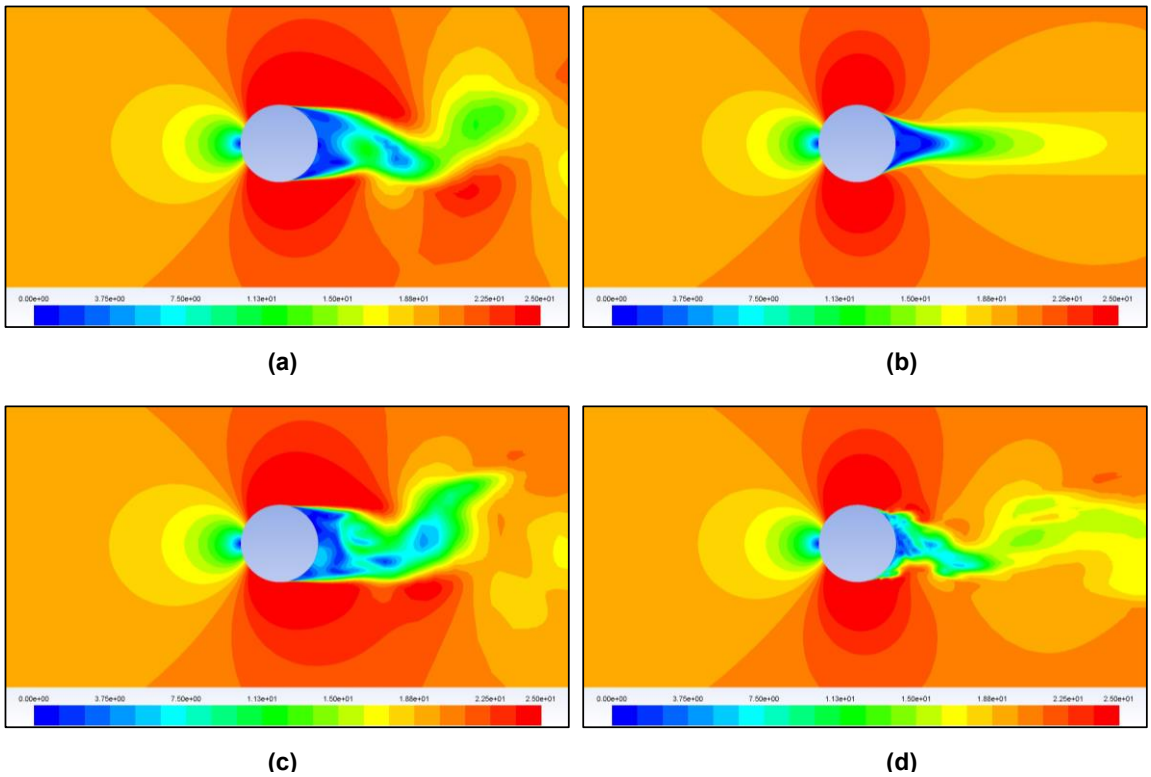

Figure 7.20 Instantaneous velocity contours of circular cylinder at $Re_D = 1 \times 10^6$ for: (a) SST k-ω, (b) k-k_L-ω-v^2, (c) DDES, and (d) DHRL

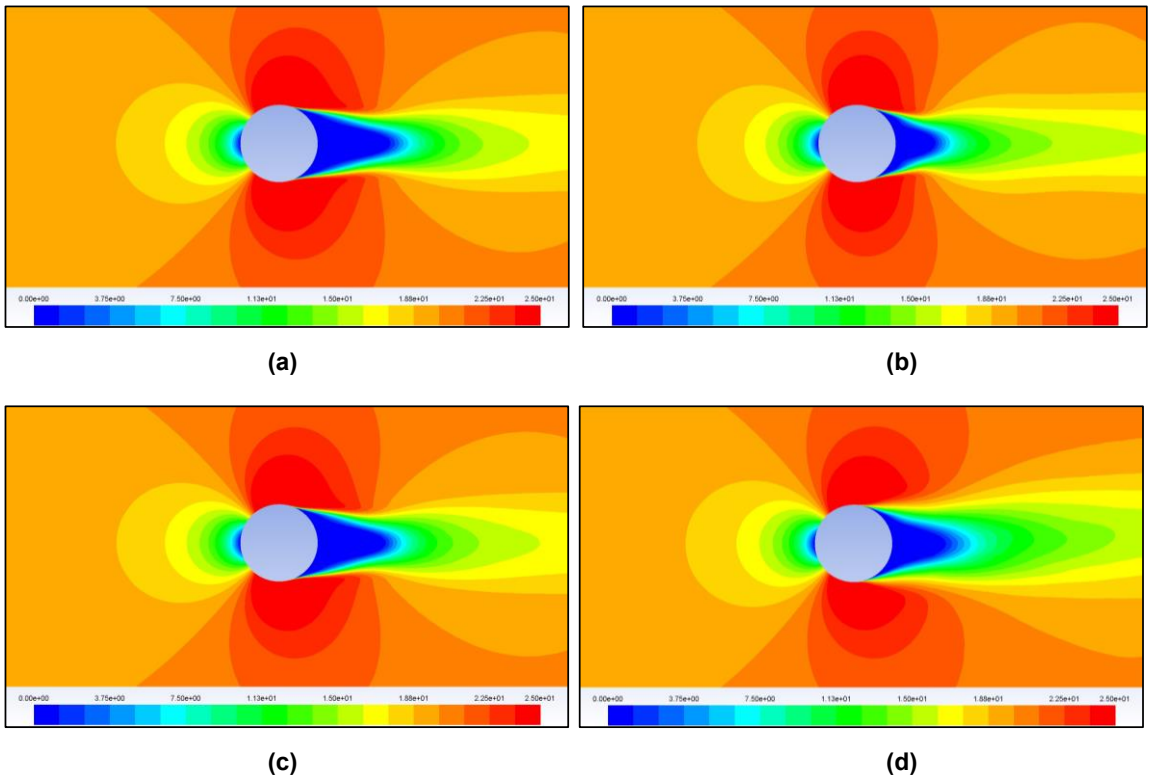

Figure 7.21 Mean x-velocity contours of circular cylinder at $Re_D = 1 \times 10^7$ for: (a) SST k-ω, (b) k-k_L-ω-v^2, (c) DDES, and (d) DHRL

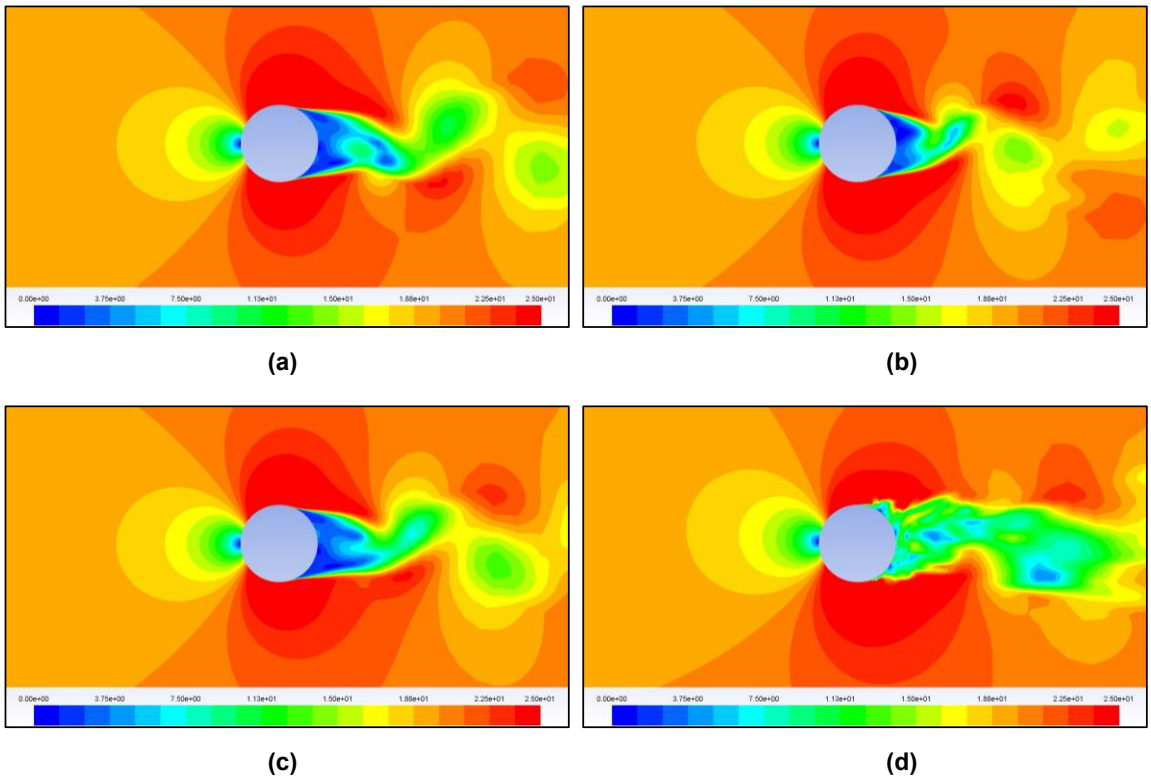

Figure 7.22 Instantaneous velocity contours of circular cylinder at $Re_D = 1 \times 10^7$ for: (a) SST k-ω, (b) k-k_L-ω-v^2, (c) DDES, and (d) DHRL

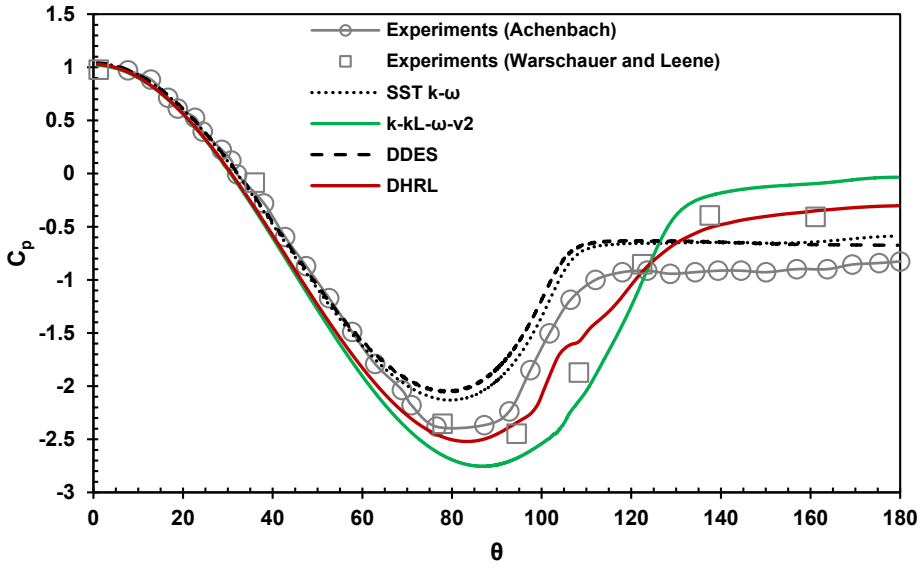

Figure 7.23 Time-averaged pressure coefficient distribution along the top of the cylinder at $Re_D = 1 \times 10^6$ in comparison with experiments by Warschauer and Leene [124] at $Re_D = 1.2 \times 10^6$ and Achenbach [100] at $Re_D = 3.6 \times 10^6$

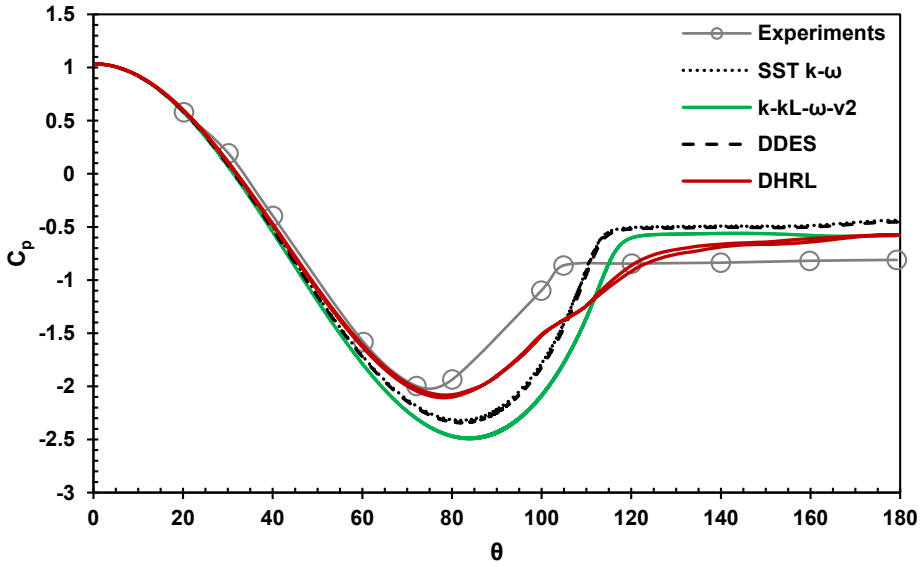

Figure 7.24 Time-averaged pressure coefficient distribution along the top of the cylinder at $Re_D = 1 \times 10^7$ in comparison with experiments by Roshko [98] at $Re_D = 8.4 \times 10^6$

In the tested flow regime from 10^4 to 10^7, the vast differences in the flow behavior and separation patterns are indicated by the drag crisis region, wherein C_D values greater than one are observed in subcritical flow, followed by a sudden drop in values in the critical regime and finally, a gradual increase in C_D for supercritical flows. A closer look into the C_D values reported for the cylinder using the DHRL model indicates a similar trend, and a strong correlation between the DHRL model results and experiments are also observed (see Table 7.2).

The contours of LES weighting coefficient (α) for all the Re tested in this study are shown in Fig. 7.25, which clearly indicate the regions where the hybrid model is in RANS, LES, or transitional modes. A closer look into the contours of α gives insight into the true behavior of the DHRL model in various flow regimes. For example, in the low Re case of 10^4, the boundary layer is practically laminar all over the cylinder and the DHRL model stays in the RANS mode all over the cylinder surface with the LES model in dormant state. In regions where the shear layer separates from the cylinder surface and transitions to turbulent flow downstream, the DHRL model quickly shifts into the LES mode. This behavior of the model highlights the fact that the value of α depends on local flow physics rather than any grid based metric. Similarly, in all the other cases, the DHRL model stays in the LES mode in separated shear layers and in the wake region of cylinder, and solves the RANS equations everywhere else in the domain.

Table 7.2 Time-averaged drag coefficient values for all models investigated in this study in comparison with experiments [39]

Re_D	Experiment	DHRL	DDES	k-k_L-ω-v^2	SST k-ω
1×10^4	1.16	1.13	1.20	1.30	1.23
1×10^5	1.26	1.29	0.94	1.01	0.78
1×10^6	0.37	0.33	0.55	0.16	0.53
1×10^7	0.69	0.78	0.38	0.46	0.37

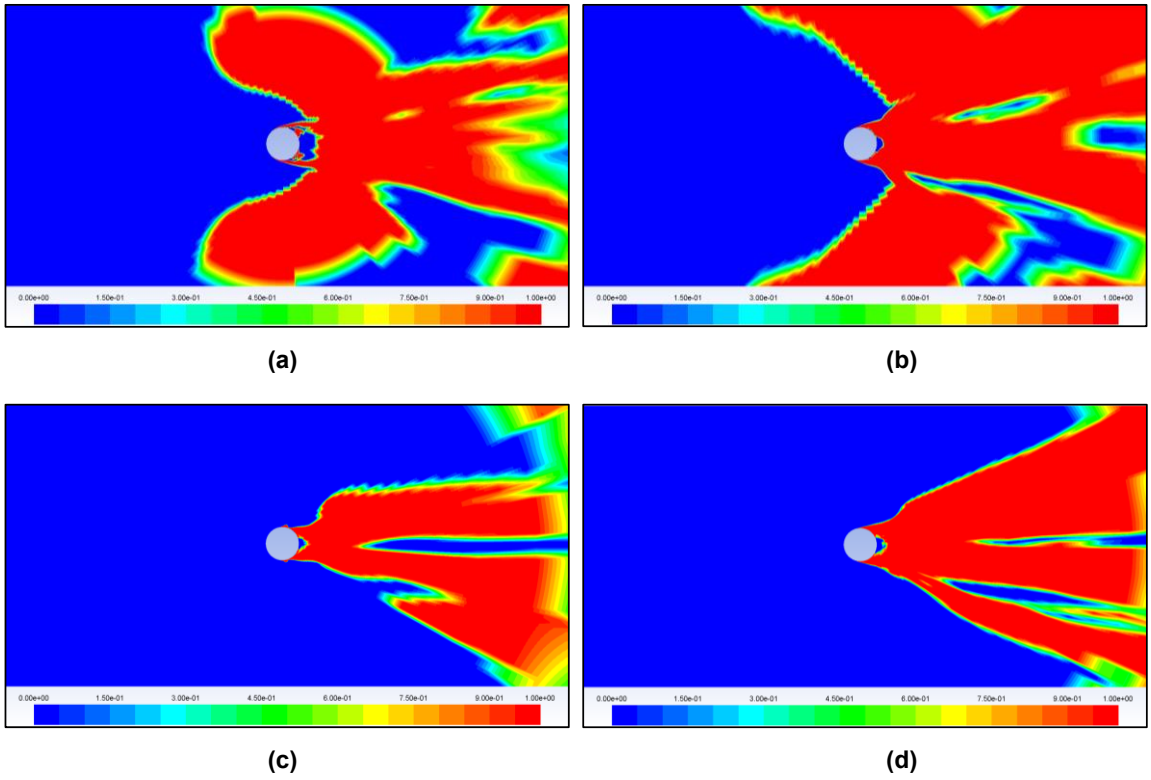

Figure 7.25 Contours of LES weighting parameter (α) in the computational domain for Re_D: (a) 1×10^4, (b) 1×10^5, (c) 1×10^6, and (d) 1×10^7. Regions with blue color ($\alpha = 0$) indicate RANS solution and red color ($\alpha = 1$) indicate LES solution

Figure 7.26 shows the instantaneous velocity contours obtained from all the models for the case of 10^5. The 3D character of the solutions that can only be obtained from hybrid and LES models and the behavior of each model in the boundary layer is illustrated in the figure. The DDES model employs the SST k-ω for its RANS component and hence, predicts a fully turbulent boundary layer over the entire cylinder surface. However, the DDES model has the added ability to resolve the large-scale structures observed in the wake region. The difference in both the models predictions (DDES and SST k-ω) can be observed in the same figure.

Lastly, time averaged streamwise velocity is plotted along a constant (x = 1) in the near wake region in Fig. 7.27 and along the symmetry axis of the cylinder (y = 0) in Fig. 7.28. Results obtained from both the hybrid models are compared with experimental data of Cantwell and Coles [123]. Minor deviations from experiments are observed in the streamwise velocity profiles from the DHRL model. On the whole, the correlation between DHRL and experiments is satisfactory.

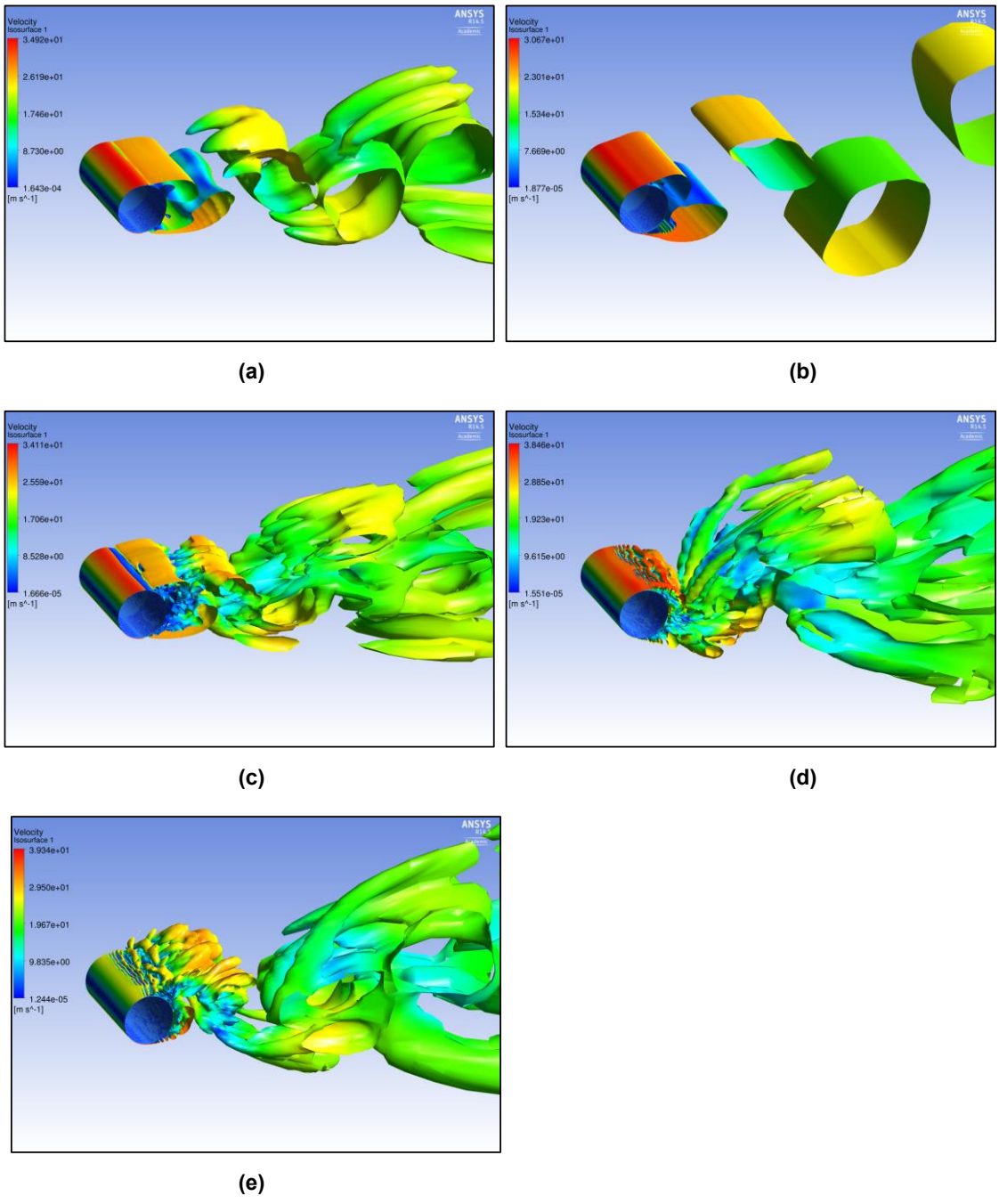

Figure 7.26 Isosurfaces of Q = 1 contoured by instantaneous velocity at $Re_D = 1 \times 10^5$ for: (a) SST k-ω, (b) k-k_L-ω-v^2, (c) DDES, (d) DHRL, and (e) MILES. Here Q-criterion is defined as $Q = 0.5\ (\Omega^2 - S^2)$

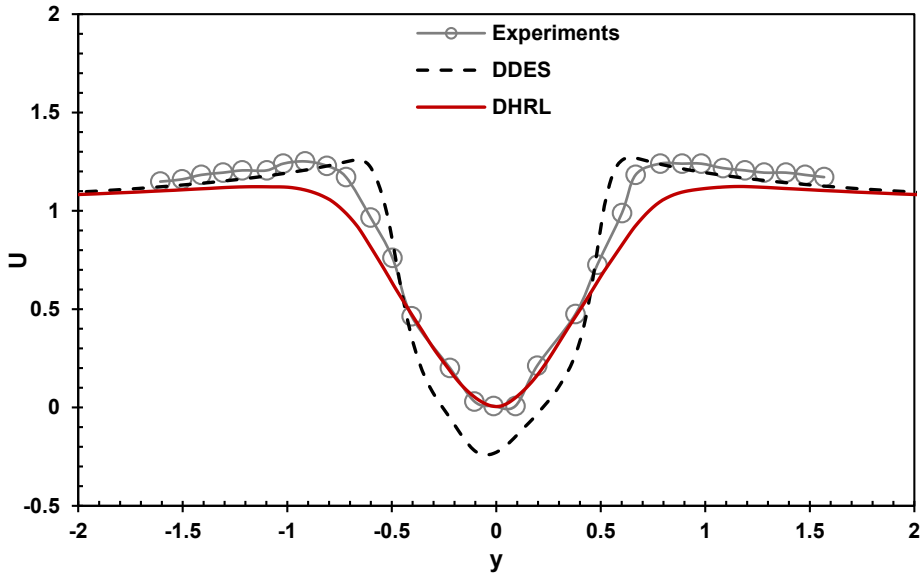

Figure 7.27 Time-averaged streamwise velocity along a constant $x = 1$ at $Re_D = 1 \times 10^5$ in comparison with experiments by Cantwell and Coles [123] at $Re_D = 1.4 \times 10^5$

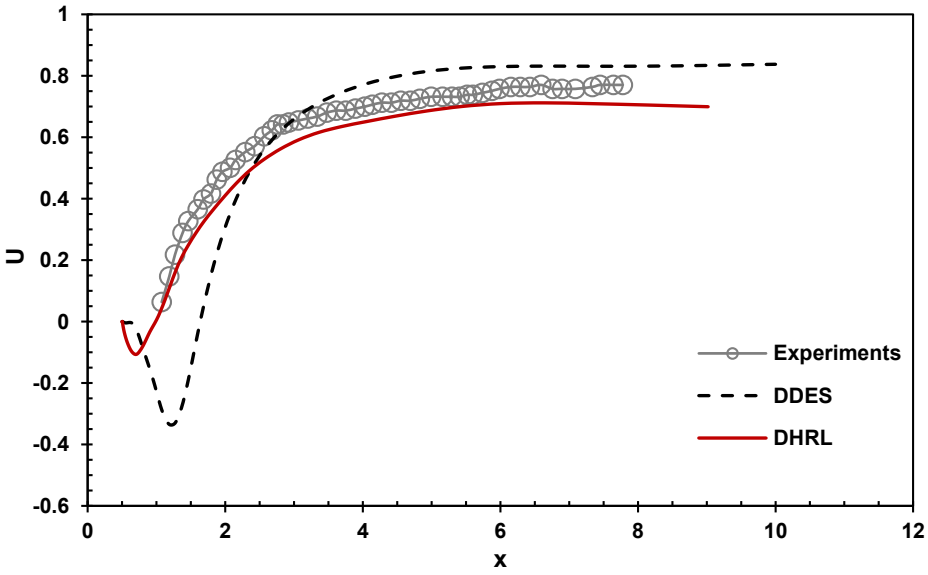

Figure 7.28 Time-averaged streamwise velocity along a constant $y = 0$ at $Re_D = 1 \times 10^5$ in comparison with experiments by Cantwell and Coles [123] at $Re_D = 1.4 \times 10^5$

To summarize, a series of 3D simulations were performed on the circular cylinder case for the flow Re_D ranging from 10^4 to 10^7. For breadth, simulations were performed using other class of models, including hybrid model (DDES), and EVMs (SST k-ω and k-k_L-ω-v^2). Results obtained from the DHRL model were compared with these models and with available data from experiments.

This particular case of flow over a 3D cylinder is challenging as the true predictive ability of the DHRL model is questioned in the presence of fully laminar, fully turbulent, and transitional boundary layers, along with the surface curvature effects prevalent in the low Re regime. The DHRL model successfully predicts these complex flow phenomena and produces results in close proximity to experiments. The model certainly improves predictions when compared to those of the widely popular DDES model. The hybrid model DDES employs the SST k-ω model for its RANS component and hence, predicts a fully turbulent boundary layer over the entire cylinder surface for all the flow regimes. The DDES model certainly improves predictions when compared to the SST k-ω model results due to the model's added ability to resolve the large-scale structures observed in the wake region. However, for higher Re flows (10^6 and 10^7), the difference in both the models predictions diminishes and the SST k-ω results are very close to those of DDES. Ignoring the RC effects and the flow transition phenomena in the low Re regime are some of the tangible reasons for discrepancy in the results. Also interesting to see are results from the k-k_L-ω-v^2 model which clearly are superior to both the DDES and SST k-ω models. A comparison between the proposed models k-k_L-ω-v^2 and DHRL indicates that further improvement in results can be obtained using the latter,

specifically at higher Re flows, due to the model's added ability to mimic a LES type simulation in the separated shear layers.

On the whole, the DHRL model with T-RC effects successfully resolves the flow characteristics observed in all the three regimes – subcritical, critical, and supercritical flow over the circular cylinder and its predictions are in good agreement with experiments. Results from this test case also highlight the fact that the DHRL is certainly an attractive alternative to full LES models especially for low/high Re flows over blunt/bluff bodies and for cases involving large-scale vortex motions.

CHAPTER VIII

CONCLUSIONS AND OUTLOOK

In the continuous search for an 'optimal' modeling technique, an effort has been made to further improve the predictive capability of currently available turbulence models for complex industrial flows without compromising in the aspect of computational efficiency. Since a universally valid turbulence model, by far and in the near future, is out of question, modeling techniques that are valid for wider range of flows with special attention towards flows with combined effects of transition and curvature and/or rotation are considered. The ultimate goal of this research effort is to present two advanced turbulence modeling techniques, one in the RANS category and the other in the hybrid RANS-LES category, with potential as practical tools, and may be desirable for solving low/high Re flows over blunt/curved bodies for the prediction of transition and RC effects. The option of two different turbulence models enables the end user to select either of the techniques according to the application of interest and availability of computational resources.

In the first part of this effort, a new RANS-based model, dubbed k-k_L-ω-v^2, has been proposed, which incorporates the capability to resolve streamline curvature and flow rotation effects into a modified version of the commercially available transition sensitive k-k_L-ω model [34]. A new transport equation for a structural variable related to the transverse velocity fluctuations (v^2) was defined and blended with the transition-sensitive

k-k_L-ω model. The added transport equation introduces the physical effects of RC into the model. The new model has been defined in such a way that RC effects are reproduced in turbulent flows and in the absence of any significant streamline curvature effects, the results predicted by the model are similar to the predictions of the transition sensitive k-k_L-ω model.

In the second part of this effort, a new hybrid model (DHRL) that seeks to combine the strengths of RANS and LES methods has been proposed. The model is based on a recently proposed version of a hybrid RANS-LES framework that can be easily integrated with any desired LES and RANS models. In this study, the proposed four-equation EVM is used for the RANS component and the MILES scheme is used for the LES component. The major advantage of this hybrid model lies in its ability to dynamically determine the RANS and LES regions in the computational domain and adjust the interface between the two regions based on the continuity of total turbulence production. Furthermore, the hybrid model is capable of resolving both flow transition from laminar-to-turbulent and rotation and/or streamline curvature effects. These complex effects enter the hybrid model via the RANS component which utilizes the proposed four-equation model.

To assess the performance of both the proposed models in terms of: (i) capturing the combined effects of flow transition and surface curvature prevalent in low Re flows; (ii) resolving significant large-scale unsteady flow structures observed in the separated shear layers (for the case of DHRL model); and (iii) predicting computational results in close proximity to experiments, a series of model validation tests have been performed on a number of cases ranging from simple to complex flow configurations. The test cases

selected for validation purposes include certain complex flow phenomena, accurate prediction of which often presents a demanding task for currently available turbulence models, thereby highlighting the need for advanced modeling techniques proposed in this work. In general, results from the k-k_L-ω-v^2 model validation cases indicate satisfactory performance and highlight the potential ability of the model to successfully resolve the T-RC effects with reasonable engineering accuracy, for a relatively small increase in computational cost. In the 2D elliptic airfoil case, it was shown that accurate RANS prediction of aerodynamic characteristics including pre-stall, stall, and post-stall requires comprehensive turbulence models, such as the k-k_L-ω-v^2, that respond correctly to transitional as well as curvature effects. In the 3D axisymmetric hill case, wherein the flowfield is generally dominated by highly unsteady phenomena, including large vortical structures shed intermittently or periodically, and multiple patches of spatially varying boundary layer separations and reattachments, it was shown that the k-k_L-ω-v^2 model produced significant improvement in flow predictions when compared to other commercially available fully turbulent models. Moreover, some of the results predicted by the model were either better or in par with those obtained from hybrid and LES models. The DHRL model, which specifically accounts for T-RC effects in the RANS region, has been validated against canonical and complex (in terms of flow prediction) test cases. Results obtained indicate overall improvement in model predictions when compared to the proposed 4-equation RANS model and other popular hybrid models, and are obtained at a significant reduction of computational cost compared to full LES models. Also interesting to note is the fact that the model produces sufficient levels of turbulent fluctuations in the flowfield, even for low Re flows, provided the mesh is

sufficiently resolved. For the 3D circular cylinder case, the DHRL model produced excellent results for all the tested flow regimes that range from low to high Re flows. Also, the hybrid model was shown to perform well in full RANS mode, transitional mode, and full LES mode, and can be successfully applied to low/high Re flows to resolve both T-RC effects.

The development of two advanced physics-based turbulence modeling techniques that are robust, simple to implement, and computationally inexpensive (when compared to their counterparts) can be considered as the critical findings of this research effort. Results from all the validation cases presented in this work provide confidence in the fact that the models perform as designed for solving low/high Re flows over blunt bodies for the prediction of T-RC effects. However, one should note that the proposed models are far from perfect and the results published in this research effort only indicate further improvement in predictions compared to currently available models. There is certainly room for advancement in the proposed modeling techniques and some recommendations for future research efforts include: (i) testing the proposed models performance on practical three-dimensional applications; (ii) extending the proposed T-RC concept to more advanced closure methods, specifically nonlinear EVMs or ASMs; (iii) further improvement in stability issues associated with the RC modeling framework; (iv) resolving the stability issues observed with the models on coarse or low quality grids; and (v) testing the proposed RANS model with different LES schemes using the DHRL framework in order to find an 'optimal' combination for the RANS model. With continuous improvements in numerical methods and computing power, the author

anticipates that the search for the ‘optimal’ turbulence model continues within higher order RANS and hybrid RANS-LES models applicable for a wider class of flows.

REFERENCES

[1] Sandoval, D. L., Harlow, F. H., and Genin, K. E., 1988, "Human Collective Dynamics: Two Groups in Adversarial Encounter," Los Alamos National Laboratory Report LA-11247-MS.

[2] Davidson, D. L., 2003, "The Role of Computational Fluid Dynamics in Process Industries," In *Frontiers of Engineering: Reports on Leading-Edge Engineering from the 2002 NAE Symposium on Frontiers of Engineering*, National Academic Press, p. 21.

[3] Piomelli, U., 1999, "Large-Eddy Simulation: Achievements and Challenges," Prog. Aerospace Sci., **35**(4), pp. 335-362.

[4] Spalart, P. R., 2000, "Strategies for Turbulence Modelling and Simulations," Int. J. Heat Fluid Flow, **21**(3), pp. 252-263.

[5] Chapman, D. R., 1979, "Computational Aerodynamics Development and Outlook," AIAA J., **17**(12), pp. 1293-1313.

[6] Derksen, J., 2002, "Lattice-Boltzmann Based Large-Eddy Simulations Applied to Industrial Flows," Computational Science – ICCS 2002, Springer Berlin Heidelberg, pp. 713-722.

[7] Hanjalic, K., 2005, "Will RANS Survive LES? A View of Perspectives," J. Fluids Eng., **127**(5), pp. 831-839.

[8] Spalart, P. R., Jou, W-H., Strelets, M., and Allmaras, S. R., 1997, "Comments on the Feasibility of LES for Wings, and on a Hybrid RANS/LES Approach," In: Advances in DNS/LES, Proceedings of the First AFOSR International Conference on DNS/LES.

[9] Orszag, S. A., Borue, V., Flannery, W. S., and Tomboulides, A. G., 1997, "Recent Successes, Current Problems, and Future Prospects of CFD," AIAA Paper No. 97-0431.

[10] Speziale, C. G., 1998, "Turbulence Modeling for Time-Dependent RANS and VLES: A Review," AIAA J., **36**(2), pp. 173-184.

[11] Batten, P., Goldberg, U., and Chakravarthy, S., 2002, "LNS – An Approach towards Embedded LES," AIAA Paper No. 2002-0427.

[12] Shih, T-H., and Liu, N-S., 2004, "Partially Resolved Numerical Simulation from RANS towards LES for Engine Turbulent Flows," AIAA Paper No. 2004-160.

[13] Chaouat, B., and Schiestel, R., 2005, "A New Partially Integrated Transport Model for Subgrid-Scale Stresses and Dissipation Rate for Turbulent Developing Flows," Phys. Fluids, **17**(6), p. 065106.

[14] Girimaji, S. S., 2006, "Partially-Averaged Navier-Stokes Model for Turbulence: A Reynolds-Averaged Navier-Stokes to Direct Numerical Simulation Bridging Method," ASME J. Appl. Mech., **73**(3), pp. 413-421.

[15] Girimaji, S. S., and Suman, S., 2012, "Partially Averaged Navier Stokes (PANS) Method for Turbulence Simulations: Theory and Practice," Progress in Hybrid-RANS LES Modelling, Springer Berlin Heidelberg, pp. 29-43.

[16] Spalart, P. R., 2009, "Detached-Eddy Simulation," Annu. Rev. Fluid Mech., **41**, pp. 181-202.

[17] Chitta, V., Dhakal, T. P., and Walters, D. K., 2012, "Prediction of Aerodynamic Characteristics for Elliptic Airfoils in Unmanned Aerial Vehicle Applications," Low Reynolds Number Aerodynamics and Transition, M. S. Genc, eds., Intech, Rijeka, Croatia, pp. 59-78.

[18] Jones, B. M., 1938, "Stalling," J. Royal Aero. Soc., **38**, pp. 747-770.

[19] Diwan, S. S., and Ramesh, O. N., 2007, "Laminar Separation Bubbles: Dynamics and Control," Sadhana, **32**(1-2), pp. 103-109.

[20] Jahanmiri, M., 2011, "Laminar Separation Bubble: Its Structure, Dynamics and Control," Technical Report, ISSN 1652-8549.

[21] Tani, I., 1964, "Low-Speed Flows Involving Bubble Separations," Prog. Aerosp. Sci., **5**, pp. 70-103.

[22] Chitta, V., Jamal, T., and Walters, D. K., 2014, "Numerical Investigation of Low-Reynolds Number Airfoil Flows Using Transition-Sensitive and Fully Turbulent RANS Models," ASME Paper No. FEDSM2014-21700.

[23] Savill, A. M., 1993, "Some Recent Progress in the Turbulence Modeling of By-Pass Transition," Near-Wall Turbulent Flows, R. M. C. So, C. G. Speziale, and B. E. Launder, eds., Elsevier, Amsterdam, The Netherlands, pp. 829-848.

[24] Westin, K. J. A., and Henkes, R. A. W. M., 1997, "Application of Turbulence Models to Bypass Transition," ASME J. Fluids Eng., **119**(4), pp. 859-866.

[25] Spalart, P. R., and Allmaras, S. R., 1994, "A One-Equation Turbulence Model for Aerodynamic Flows," La Recherche Aérospatiale, **1**, pp. 5-21.

[26] Menter, F. R., 1994, "Two-Equation Eddy-Viscosity Turbulence Models for Engineering Applications," AIAA J., **32**(8), pp. 1598-1605.

[27] Rumsey, C. L., Pettersson-Reif, B. A., and Gatski, T. B., 2006, "Arbitrary Steady-State Solutions with the k-Epsilon Model," AIAA J., **44**(7), pp. 1586-1592.

[28] Rumsey, C. L., 2007, "Apparent Transition Behavior of Widely-Used Turbulence Models," Int. J. Heat Fluid Flow, **28**(6), pp. 1460-1471.

[29] Suzen, Y. B., and Huang, P. G., 2000, "Modeling of Flow Transition Using an Intermittency Transport Equation," ASME J. Fluids Eng., **122**(2), pp. 273-284.

[30] Steelant, J., and Dick, E., 2000, "Modeling of Laminar-Turbulent Transition for High Freestream Turbulence," ASME J. Fluids Eng., **123**(1), pp. 22-30.

[31] Dhawan, S., and Narasimha, R., 1958, "Some Properties of Boundary Layer during the Transition from Laminar to Turbulent Flow Motion," J. Fluid Mech., **3**, pp. 418-436.

[32] Wang, C., and Perot, B., 2002, "Prediction of Turbulent Transition in Boundary Layers Using the Turbulent Potential Model," J. Turbul., **3**(1), pp. 1-15.

[33] Menter, F. R., Langtry, R. B., Likki, S. R., Suzen, Y. B., Huang, P. G., and Völker, S., 2006, "A Correlation-Based Transition Model Using Local Variables – Part I: Model Formulation," ASME J. Turbomach., **128**(3), pp. 413-422.

[34] Walters, D. K., and Cokljat, D., 2008, "A Three-Equation Eddy-Viscosity Model for Reynolds-Averaged Navier-Stokes Simulations of Transitional Flow," ASME J. Fluids Eng., **130**(12), p. 121401.

[35] Perot, J. B., 1999, "Turbulence Modeling Using Body Force Potentials," Phys. Fluids, **11**(9), pp. 2645-2656.

[36] Smith, A. M. O., and Gamberoni, N., 1956, "Transition, Pressure Gradient, and Stability Theory," Douglas Aircraft, Rept. ES-26388.

[37] Stock, H. W., and Haase, W., 1999, "A Feasibility Study of e^N Transition Prediction in Navier-Stokes Methods for Airfoils," AIAA J., **37**(10), pp. 1187-1196.

[38] Lian, Y., and Shyy, W., 2007, "Laminar-Turbulent Transition of a Low Reynolds Number Rigid or Flexible Airfoil," AIAA J., **45**(7), pp. 1501-1513.

[39] Schlichting, H., and Klaus, G., 2000, Boundary Layer Theory, Springer, New York.

[40] Wu, X., Jacobs, R., Hunt, J., and Durbin, P., 1999, "Simulation of Boundary Layer Transition Induced by Periodically Passing Wakes," J. Fluid Mech., **398**, pp. 109-153.

[41] Michelassi, V., Wissink, J. G., and Rodi, W., 2002, "Analysis of DNS and LES of Flow in a Low Pressure Turbine Cascade with Incoming Wakes and Comparison with Experiments," Flow Turbul. Combust., **69**(3-4), pp. 295-329.

[42] Durbin, P., 2011, "Review: Adapting Scalar Turbulence Closure Models for Rotation and Curvature," ASME J. Fluids Eng., **133**(6), p. 061205.

[43] Muck, K. C., Hoffman, P. H., and Bradshaw, P., 1985, "The Effect of Convex Surface Curvature on Turbulent Boundary Layers," J. Fluid Mech., **161**, pp. 347-369.

[44] Launder, B. E., Priddin, C. H., and Sharma, B. I., 1977, "The Calculation of Turbulent Boundary Layers on Spinning and Curved Surfaces," ASME J. Fluids Eng., **99**(1), pp. 231-239.

[45] Howard, J. H. G., Patankar, S. V., and Bordynuik, R. M., 1980, "Flow Prediction in Rotating Ducts Using Coriolis-Modified Turbulence Models," **102**(4), pp. 456-461.

[46] Park, S. W., and Chung, M. K., 1989, "Curvature-Dependent Two-Equation Model for Prediction of Turbulent Recirculating Flows," **27**(3), pp. 340-344.

[47] Pettersson-Reif, B. A., Durbin, P. A., and Ooi, A., 1999, "Modeling Rotational Effects in Eddy-Viscosity Closures," Int. J. Heat Fluid Flow, **20**(6), pp. 563-573.

[48] York, W. D., Walters, D. K., and Leylek, J. H., 2009, "A Simple and Robust Linear Eddy-Viscosity Formulation for Curved and Rotating Flows," Int. J. Numer. Methods Heat Fluid Flow, **19**(6), pp. 745-776.

[49] Spalart, P. R., and Shur, M. L., 1997, "On the Sensitization of Turbulence Models to Rotation and Curvature," Aerosp. Sci. Technol., **1**(5), pp. 297-302.

[50] Smirnov, P. E., and Menter, F. R., 2009, "Sensitization of the SST Turbulence Model to Rotation and Curvature by Applying the Spalart-Shur Correction Term," ASME J. Turbomach., **131**(4), p. 041010.

[51] Dhakal, T. P., and Walters, D. K., 2011, "A Three-Equation Variant of the SST k-ω Model Sensitized to Rotation and Curvature Effects," ASME J. Fluids Eng., **133**(11), p. 111201.

[52] Gatski, T. B., and Speziale, C. G., 1993, "On Explicit Algebraic Stress Models for Complex Turbulent Flows," J. Fluid Mech., **254**, pp. 59–78.

[53] Girimaji, S. S., 1997, "A Galilean Invariant Explicit Algebraic Reynolds Stress Model for Turbulent Curved Flows," Phys. Fluids, **9**(4), pp. 1067-1077.

[54] Wallin, S., and Johansson, A. V., 2002, "Modelling Streamline Curvature Effects in Explicit Algebraic Reynolds Stress Turbulence Models," Int. J. Heat Fluid Flow, **23**(5), pp. 721-730.

[55] Davidson, L., and Peng, S. H., 2003, "Hybrid LES-RANS Modelling: A One-Equation SGS Model Combined with a k-ω Model for Predicting Recirculating Flows," Int. J. Numer. Meth. Fluids, **43**(9), pp. 1003-1018.

[56] Balaras, E., Benocci, C., and Piomelli, U., 1996, "Two-Layer Approximate Boundary Conditions for Large-Eddy Simulations," AIAA J., **34**(6), pp. 1111-1119.

[57] Cabot, W. H., and Moin, P., 1999, "Approximate Wall Boundary Conditions in the Large-Eddy Simulation of High Reynolds Number Flow," Flow Turbul. Combust., **63**(1-4), pp. 269-291.

[58] Temmerman, L., Hadžiabdić, M., Leschziner, M. A., and Hanjalić, K., 2005, "A Hybrid Two-Layer URANS-LES Approach for Large Eddy Simulation at High Reynolds Numbers," Int. J. Heat Fluid Flow, **26**(2), pp. 173-190.

[59] Piomelli, U., Balaras E., Pasinato, H., Squires, K. D., and Spalart, P. R., 2003, "The Inner-Outer Layer Interface in Large-Eddy Simulations with Wall-Layer Models," Int. J. Heat Fluid Flow, **24**(4), pp. 538-550.

[60] Schlüter, J. U., Pitsch, H., and Moin, P., 2004, "Large Eddy Simulation Inflow Conditions for Coupling with Reynolds-Averaged Flow Solvers," AIAA J., **42**(3), pp. 478-484.

[61] Keating, A., De Prisco, G., and Piomelli, U., 2006, "Interface Conditions for Hybrid RANS/LES Calculations," Int. J. Heat Fluid Flow, **27**(5), pp. 777-788.

[62] Slimon, S., 2003, "Computation of Internal Separated Flows Using a Zonal Detached Eddy Simulation Approach," ASME Paper No. IMECE 2003-43881.

[63] Menter, F. R., and Kuntz, M., 2004, "Adaption of Eddy-Viscosity Turbulence Models to Unsteady Separated Flow Behind Vehicles," The Aerodynamics of Heavy Vehicles: Trucks, Buses, and Trains, Springer Berlin Heidelberg, pp. 339-352.

[64] Spalart, P. R., Deck, S., Shur, M. L., Squires, K. D., Strelets, M. Kh., and Travin, A., 2006, "A New Version of Detached-Eddy Simulation, Resistant to Ambiguous Grid Densities," Theor. Comput. Fluid Dyn., **20**(3), pp. 181-195.

[65] Shur, M. L., Spalart, P. R., Strelets, M. Kh., and Travin, A. K., 2008, "A Hybrid RANS-LES Approach with Delayed-DES and Wall-Modelled LES Capabilities," Int. J. Heat Fluid Flow, **29**(6), pp. 1638-1649.

[66] Launder, B. E., and Shima, N., 1989, "Second-Moment Closure for the Near-Wall Sublayer: Development and Application," AIAA J., **27**(10), pp. 1319-1325.

[67] Smagorinsky, J., 1963, "General Circulation Experiments with the Primitive Equations. I. The Basic Experiment," Mon. Weather Rev., **91**(3), pp. 99-164.

[68] Germano, M., Piomelli, U., Moin, P., and Cabot, W. H., 1991 "A Dynamic Subgrid-Scale Eddy Viscosity Model," Phys. Fluids, **3**(7), pp. 1760-1765.

[69] Moin, P., Squires, K., Cabot, W., and Lee, S., 1991, "A Dynamic Subgrid-Scale Model for Compressible Turbulence and Scalar Transport," Phys. Fluids A, **3**(11), pp. 2746-2757.

[70] Yang, Z., Cui, G., Xu, C., and Zhang, Z., 2012, "Large Eddy Simulation of Rotating Turbulent Channel Flow with a New Dynamic Global-Coefficient Nonlinear Subgrid Stress Model," J. Turbul., **13**(48), pp. 1-20.

[71] Fureby, C., and Grinstein, F. F., 1999, "Monotonically Integrated Large Eddy Simulation of Free Shear Flows," AIAA J., **37**(5), pp. 544-556.

[72] Gathmann, R. J., Si-Ameur, M., and Mathey, F., 1993, "Numerical Simulations of Three-Dimensional Natural Transition in the Compressible Confined Shear Layer," Phys. Fluids, **5**(11), pp. 2946-2968.

[73] Porter, D. H., Pouquet, A., and Woodward, P. R., 1994, "Kolmogorov-Like Spectra in Decaying Three-Dimensional Supersonic Flows," Phys. Fluids, **6**(6), pp. 2133-2142.

[74] Fureby, C., 1996, "On Subgrid Scale Modeling in Large Eddy Simulations of Compressible Fluid Flow," Phys. Fluids, **8**(5), pp. 1301-1311.

[75] Grinstein, F. F., Gutmark, E. J., Parr, T. P., Hanson-Parr, D. M., and Obeysekare, U., 1996, "Streamwise and Spanwise Vortex Interaction in an Axisymmetric Jet. A Computational and Experimental Study," Phys. Fluids, **8**(6), pp. 1515-1524.

[76] Chitta, V., Dhakal, T. P., and Walters, D. K., 2015, "Sensitization of a Transition-Sensitive Linear Eddy-Viscosity Model to Rotation and Curvature Effects," J. Fluids Eng., **137**(3), p. 031207.

[77] Chitta, V., Dhakal, T. P., and Walters, D. K., 2013, "Development and Application of a New Four-Equation Eddy-Viscosity Model for Flows with Transition, Curvature and Rotation Effects," ASME Paper No. FEDSM2013-16372.

[78] Chitta, V., and Walters, D. K., 2012, "Prediction of Aerodynamic Characteristics of an Elliptic Airfoil at Low Reynolds Number," ASME Paper No. FEDSM2012-72389.

[79] Chitta, V., Jamal, T., and Walters, D. K., 2015, "Numerical Study of Vortical Separation from a Three-Dimensional Hill Using Eddy-Viscosity Models," ASME-JSME-KSME Paper No. AJK2015-03223.

[80] Chitta, V., and Walters, D. K., 2015, "A Hybrid RANS-LES Modeling Methodology Sensitized to Transitional and Curvature/Rotation Effects," ASME Paper No. IMECE2015-53155.

[81] Walters, D. K., 2009, "Physical Interpretation of Transition-Sensitive RANS Models Employing the Laminar Kinetic Energy Concept," ERCOFTAC, Bulletin 80, pp. 1-6.

[82] Matsubara, M., and Alfredsson, P. H., 2001, "Disturbance Growth in Boundary Layers Subjected to Free-Stream Turbulence," J. Fluid Mech., **430**, pp. 149-168.

[83] Jacobs, R. G., and Durbin, P. A., 2001, "Simulations of Bypass Transition," J. Fluid Mech., **428**, pp. 185-212.

[84] Mayle, R. E., and Schulz, A., 1997, "The Path to Predicting Bypass Transition," ASME J. Turbomach., **119**(3), pp. 405-411.

[85] Klebanoff, P. S., 1971, "Effects of Free-Stream Turbulence on a Laminar Boundary Layer," Bull. Am. Phys. Soc., **16**(11), p. 1323.

[86] Walters, D. K., and Leylek, J. H., 2004, "A New Model for Boundary Layer Transition Using a Single-Point RANS Approach," ASME J. Turbomach., **126**(1), pp. 193-202.

[87] Volino, R. J., 1998, "A New Model for Free-Stream Turbulence Effects on Boundary Layers," ASME J. Turbomach., **120**(3), pp. 613-620.

[88] Jacobs, R. G., and Durbin, P. A., 1998, "Shear Sheltering and the Continuous Spectrum of the Orr-Sommerfeld Equation," Phys. Fluids, **10**(8), pp. 2006-2011.

[89] Lilly, D. K., 1992, "A Proposed Modification of the Germano Subgrid-Scale Closure Method," Phys. Fluids, **4**(3), pp. 633-635.

[90] Walters, D. K., Bhushan, S., Alam, M. F., and Thompson, D. S., 2013, "Investigation of a Dynamic Hybrid RANS/LES Modelling Methodology for Finite-Volume CFD Simulations," Flow Turbul. Combust., **91**(3), pp. 643-667.

[91] Patankar, S. V., and Spalding, D. B., 1972, "A Calculation Procedure for Heat, Mass, and Momentum Transfer in Three-Dimensional Parabolic Flows," Int. J. Heat Mass Transfer, **15**(10), pp. 1787-1806.

[92] ANSYS, ANSYS Fluent Theory Guide 14.0, ANSYS, Inc., Canonsburg, PA.

[93] Nair, M. T., and Sengupta, T. K., 1997, "Unsteady Flow past Elliptic Cylinders," J. Fluids Structures, **11**(6), pp. 555-595.

[94] Matsubara, M., and Alfredsson, P. H., 1996, "Experimental Study of Heat and Momentum Transfer in Rotating Channel Flow," Phys. Fluids, **8**(11), pp. 2964-2973.

[95] Kristoffersen, R., and Andersson, H. I., 1993, "Direct Simulations of Low-Reynolds-Number Turbulent Flow in a Rotating Channel," J. Fluid Mech., **256**, pp. 163-197.

[96] Coupland, J., 1990, "ERCOFTAC Special Interest Group on Laminar to Turbulent Transition and Retransition: T3A and T3B Test Cases," Technical Report No. A309514.

[97] Holloway, D. S., Walters, D. K., and Leylek, J. H., 2004, "Prediction of Unsteady, Separated Boundary Layer over a Blunt Body for Laminar, Turbulent, and Transitional Flow," Int. J. Numer. Methods Fluids, **45**(12), pp. 1291-1315.

[98] Roshko, A., 1961, "Experiments on the Flow Past a Circular Cylinder at Very High Reynolds Number," J. Fluid Mech., **10**(3), pp. 345-356.

[99] Zdravkovich, M. M., 1990, "Conceptual Overview of Laminar and Turbulent Flows Past Smooth and Rough Circular Cylinders," J. Wind Eng. Ind. Aerodyn., **33**(1-2), pp. 53-62.

[100] Achenbach, E., 1968, "Distribution of Local Pressure and Skin Friction around a Circular Cylinder in Cross-Flow up to Re = 5×10^6," J. Fluid Mech., **34**(4), pp. 625-639.

[101] Schubauer, G. B., 1939, "Air Flow in the Boundary Layer of an Elliptic Cylinder," National Advisory Committee for Aeronautics, Report No. 652.

[102] Lin, J. C. M., and Pauley, L. L., 1996, "Low-Reynolds-Number Separation on an Airfoil," AIAA J., **34**(8), pp. 1570-1577.

[103] Kwon, K., and Park, S. O., 2005, "Aerodynamic Characteristics of an Elliptic Airfoil at Low Reynolds Number," J. Aircraft, **42**(6), pp. 1642-1644.

[104] Jackson, P. S., and Hunt, J. C. R., 1975, "Turbulent Wind Flow over a Low Hill," Quart. J. R. Met. Soc., **101**(430), pp. 929-955.

[105] Ishihara, T., Hibi, K., and Oikawa, S., 1999, "A Wind Tunnel Study of Turbulent Flow over a Three-Dimensional Steep Hill," J. Wind Eng. Indus. Aerodyn., **83**(1-3), pp. 95-107.

[106] Simpson, R. L., Long, C. H., and Byun, G., 2002, "Study of Vortical Separation from an Axisymmetric Hill," Int. J. Heat Fluid Flow, **23**(5), pp. 582-591.

[107] Byun, G., Simpson, R. L., and Long, C. H., 2004, "Study of Vortical Separation from Three-Dimensional Symmetric Bumps," AIAA J., **42**(4), pp. 754-765.

[108] Patel, N., Stone, C., and Menon, S., 2003, "Large-Eddy Simulation of Turbulent Flow over an Axisymmetric Hill," AIAA Paper No. 2003-967.

[109] Patel, N., and Menon, S., 2007, "Structure of Flow Separation and Reattachment Behind an Axisymmetric Hill," J. Turbul., **8**(36), pp. 1-24.

[110] Persson, T., Liefvendahl, M., Bensow, R. E., and Fureby, C., 2006, "Numerical Investigation of the Flow over an Axisymmetric Hill Using LES, DES, and RANS," J. Turbul., **7**(4), pp. 1-17.

[111] Wang, C., Jang, Y. J., and Leschziner, M. A., 2004, "Modelling Two- and Three-Dimensional Separation From Curved Surfaces with Anisotropy-Resolving Turbulence Closures," Int. J. Heat Fluid Flow, **25**(3), pp. 499-512.

[112] Castagna, J., Yao, Y., and Yao, J., 2014, "Direct Numerical Simulation of a Turbulent Flow Over an Axisymmetric Hill," Comput. Fluids, **95**, pp. 116-126.

[113] Garcia-Villalba, M., Li, N., Rodi, W., and Leschziner, M. A., 2009, "Large-Eddy Simulation of Separated Flow over a Three-Dimensional Axisymmetric Hill," J. Fluid Mech., **627**, pp. 55-96.

[114] Tessicini, F., Li, N., Leschziner, M. A., 2007, "Large-Eddy Simulation of Three-Dimensional Flow around a Hill-Shaped Obstruction with a Zonal Near-Wall Approximation," Int. J. Heat Fluid Flow, **28**(5), pp. 894-908.

[115] Rhie, C. M., and Chow, W. L., 1983, "Numerical Study of the Turbulent Flow Past an Airfoil with Trailing Edge Separation," AIAA J., **21**(11), pp. 1525-1532.

[116] Jasak, H., Weller, H. G., and Gosman, A. D., 1999, "High Resolution NVD Differencing Scheme for Arbitrarily Unstructured Meshes," Int. J. Numer. Methods Fluids, **31**(2), pp. 431-449.

[117] Margolin, L. G., and Rider, W. J., 2005, "The Design and Construction of Implicit LES Models," Int. J. Numer. Methods Fluid, **47**(10-11), pp. 1173-1179.

[118] Adedoyin, A. A., Walters, D. K., and Bhushan, S., 2006, "Assessment of Modeling and Discretization Error in Finite-Volume Large Eddy Simulations," ASME Paper No. IMECE2006-14918.

[119] Leonard, B. P., 1979, "A Stable and Accurate Convective Modelling Procedure Based on Quadratic Upstream Interpolation," Comput. Methods Appl. Mech. Eng., **19**(1), pp. 59-98.

[120] Jordan, S. A., and Ragab, S. A., 1998, "A Large-Eddy Simulation of the Near Wake of a Circular Cylinder," ASME J. Fluids Eng., **120**(2), pp. 243-252.

[121] Breuer, M., 2000, "A Challenging Test Case for Large Eddy Simulation: High Reynolds Number Circular Cylinder Flow," Int. J. Heat Fluid Flow, **21**(5), pp. 648-654.

[122] Travin, A., Shur, M. L., Strelets, M. Kh., and Spalart, P. R., 2000, "Detached-Eddy Simulations Past a Circular Cylinder," Flow Turbul. Combust., **63**(1-4), pp. 293-313.

[123] Cantwell, B., and Coles, D., 1983, "An Experimental Study of Entrainment and Transport in the Turbulent Near Wake of a Circular Cylinder," J. Fluid Mech., **136**, pp. 321-374.

[124] Warschauer, K. A., and Leene, J. A., 1971, "Experiments on Mean and Fluctuating Pressures of Circular Cylinders at Cross Flow at Very High Reynolds Numbers," In Proceedings of International Conference on Wind Effects on Buildings and Structures, Tokyo, pp. 305-31.